UNIVERSITY OF CALIFORNIA,
IRVINE

Infrared Optical and Thermal Properties of Microstructures – from Nature to Bio-inspired Materials

DISSERTATION

submitted in partial satisfaction of the requirements
for the degree of

DOCTOR OF PHILOSOPHY

in Mechanical and Aerospace Engineering

by

Anirudh Krishna

Dissertation Committee:
Professor Jaeho Lee, Chair
Professor Adriana Briscoe
Professor Jack Brouwer

2020

TABLE OF CONTENTS

LIST OF FIGURES

LIST OF TABLES

ACKNOWLEDGEMENTS

I would like to express my sincere gratitude to my advisor, Dr. Jaeho Lee, for his invaluable mentorship, guidance and support, which helped my advance my knowledge and research aptitude in a motivated and scholarly manner. His eagerness to counsel and mentor were integral to my academic progress at the University of California, Irvine. My interactions with him, through individual meetings, lab meetings and otherwise, lay at the foundation of who I aim to be as a researcher and scholar.

I am also extremely grateful to, and indebted to, Dr. Adriana Briscoe, who was an excellent mentor to me in my last few years of graduate studies. Her vast knowledge, empathy, and know-how are qualities I will strive to emulate in my academic life.

I would also like to thank Dr. Jack Brouwer, whose support and counsel through the course of this study in his capacity as a dissertation committee member aided greatly in shaping the study to what it presently is. I am thankful for his practical suggestions and comments, which stem from his fondness for knowledge. Attending his classes will always be part of the moments I cherish in graduate life.

I am very thankful to the dogs and people in my life, without whom none of this would have been possible, foremost to my dog, Liliana, and my parents, whose unwavering support and unconditional love is the basis of who I am, where I am and what I am. My academic pursuits are made possible due to their intentions of placing prime importance on education, regardless of financial or other hurdles. This dissertation, and all of my academic work, is a dedication to Liliana.

VITA

Anirudh Krishna

Education

University of California, Irvine December 2020

Doctor of Philosophy in Mechanical and Aerospace Engineering

University of California, Irvine December 2016

Master of Science in Mechanical and Aerospace Engineering

National Institute of Technology, Trichy August 2014

Bachelor of Technology in Mechanical Engineering

Journal Publications

1. X. Nie, Y. Yoo, H. Hewakuruppu, J. Sullivan, **A. Krishna**, and J. Lee, "Cool White Polymer Coatings based on Glass Bubbles for Buildings," *Scientific Reports* 10*,* 6661, 2020.
2. **A. Krishna**, X. Nie, A. D. Warren, J. E. Llorente-Bousquets, A. D. Briscoe, J. Lee, "Infrared optical and thermal properties of microstructures in butterfly wings," *Proceedings of the National Academy of Sciences*, 117(3), 1566–1572, 2020.
3. **A. Krishna**, J. M. Kim, J. Leem, M. C. Wang, S. Nam, and J. Lee, "Ultraviolet to Mid-Infrared Emissivity Control by Mechanically Reconfigurable Graphene," *Nano Letters*, 19(8), 5086–5092, 2019.
4. M. Sala-Casanovas†, **A. Krishna**†, Z. Yu, and J. Lee, "Bio-inspired Stretchable Selective Emitters based on Corrugated Nickel for Personal Thermal Management," *Nanoscale and Microscale Thermophysical Engineering*, 23(3), 173–187, 2019.
5. **A. Krishna**, and J. Lee, "Morphology-Driven Emissivity of Microscale Tree-like Structures for Radiative Thermal Management," *Nanoscale and Microscale Thermophysical Engineering*, 22(2), 124–136, 2018.

Conference Proceedings, Peer-Reviewed

1. **A. Krishna**, J. M. Kim, J. Leem, M. C. Wang, S. Nam, and J. Lee, "Dynamic Radiative Thermal Management by Crumpled Graphene," IEEE Intersociety Conference on Thermal and Thermomechanical Phenomena in Electronic Systems (ITherm 2019).
2. X. Nie, **A. Krishna**, M. Jeong, P. Wu, C. Yu, and J. Lee, "Stretchable Selective Emitters based on Carbon Nanotube Films for Adaptive Thermal Control," IEEE Intersociety Conference on Thermal and Thermomechanical Phenomena in Electronic Systems (ITherm 2019).
3. G. Liang, A. Sadeghifard, **A. Krishna**, J. Lee, and E. P. Hernandez, "Modeling and Analysis of a Shape Memory Alloy-based Adaptive Regulator for Thermal Management," ASME International Technical Conference on Packaging and Integration of Electronic and Photonic Microsystems (InterPACK 2019).
4. **A. Krishna**, and J. Lee, "Morpho Butterfly-Inspired Spectral Emissivity of Metallic Microstructures for Radiative Cooling," IEEE Intersociety Conference on Thermal and Thermomechanical Phenomena in Electronic Systems (ITherm 2018).
5. J. Sullivan, **A. Krishna**, and J. Lee, "Porous Nickel as a Selective Emitter for Surface Cooling in Various Environments," IEEE Intersociety Conference on Thermal and Thermomechanical Phenomena in Electronic Systems (ITherm 2018).

Selected Honors and Awards

1. Graduate Dean's Dissertation Fellowship, 2020 – 2021
2. Outstanding Paper Award, IEEE ITherm, 2019
3. Samueli School of Engineering Graduate Student Research and Travel Grant, 2019
4. Best Oral Presentation Award, MRS Spring Meeting, 2018
5. Samueli School of Engineering Ph.D. Bridge Fellowship, 2017

Appointments

University of California, Irvine 2019 – 2020

Instructor

- MAE 120 (Heat Transfer)

University of California, Irvine 2016 – 2020

Teaching Assistant

- MAE 120 (Heat Transfer)
- MAE 107 (Thermal Laboratory)

University of California, Irvine 2016 – 2018

Grader

- MAE 220 (Conduction Heat Transfer)

ABSTRACT OF THE DISSERTATION

Infrared Optical and Thermal Properties of Microstructures – from Nature to Bio-inspired Materials

by

Anirudh Krishna

Doctor of Philosophy in Mechanical and Aerospace Engineering

University of California, Irvine, 2020

Professor Jaeho Lee, Chair

Control over mid-infrared optical properties is critical for applications such as thermoregulation, infrared sensing, thermal imaging, and thermal camouflage. The distinct wavelength ranges for heating and cooling by radiative heat transfer call for selective emitters to fulfill the need for spectral optical control. The present doctoral research focuses on the role played by microstructures in controlling the infrared optical properties of materials and understanding the relationship to temperature and impact on thermal properties. There is a plethora of examples of microstructure-dependent optical properties in nature. The present work focuses on the mid-infrared optical and thermal properties of microstructures and aims to learn from nature in developing bio-inspired microstructures geared towards varying human needs and applications.

Butterfly wings have garnered much attention towards studies on their visible optical properties, but not much is known about their infrared optical and thermal properties. The mid-infrared wavelengths of 7.5-14 μm coincide with the atmospheric transmission window and are particularly important for radiative heat transfer in the

ambient environment. A high mid-infrared emissivity can allow for cooling by aiding in heat loss to the outer space, whereas a low mid-infrared emissivity can minimize this heat loss. This work uses Fourier-transform infrared (FTIR) spectroscopy and infrared thermography to show that the mid-infrared emissivity of butterfly wings from warmer climates is up to 2 times higher than that of butterfly wings from cooler climates. I also use rigorous coupled-wave analysis (RCWA) and finite-difference time-domain (FDTD) computations to reproduce the spectroscopy data. The spectral emissivity values govern the thermal properties of butterfly wings, and the thermal computations show that butterfly wings in their respective habitats can maintain a moderate and viable temperature range through a balance of solar absorption and infrared emission. Using the computed optical properties, a potential correlation between the mid-infrared emissivity of their wings and climatic conditions such as air temperature has been investigated.

In a similar vein, Saharan silver ants make use of their hair-like microstructures to enhance their mid-infrared emissivity and remain cool in the desert climates. This work replicates the relatively simple hair-like structures in the form of corrugated, periodic microstructures to control the infrared optical properties of various materials. Furthermore, I add tunability to the optical properties by utilizing elastomeric substrates and show mid-infrared emissivity control by mechanically reconfigurable graphene. Here, mechanical stretching and releasing induces controlled morphology changes. By integrating graphene with stretchable, elastomeric substrates, I fabricate 10 μm pitch crumpled graphene optimized for mid-infrared emissivity control. The interference between adjacent crumpled features and diffraction at the graphene/air interface lead to wavelength-specific variations in transmissivity, and consequently emissivity for the

crumpled graphene at 9.9 μm and 13 μm wavelengths. The measurements also show reversible changes of emissivity over 30 cycles of stretching and releasing at the wavelength of 9.9 μm.

To present a more practical system, I have developed a selective emitter using a simple metallic coating. By evaporating nickel on a pre-strained elastomer, I create 700 nm periodic corrugations that increase the nickel absorptivity from 0.3 to 0.7 in 0.2-2.5 μm wavelengths due to multiple scattering, as supported by spectroscopy and computations. The optical change is reversible and is used to demonstrate a stretchable wearable system. The corrugated nickel on a human body at 309 K allows a heat flux of 62 Wm^{-2} out of the skin when stretched and 79 Wm^{-2} into the skin when released.

The present doctoral research thus studies the role of microstructures in the optical and thermal properties of natural beings and applies the findings towards bio-inspired materials that aim to satisfy ever-growing human needs.

INTRODUCTION

Many animals living in extreme environments rely substantially on maximizing or minimizing the heat losses from their bodies to ensure survivability in their habitats (1–8). Several animals have effectively adapted to their habitat environments by making use of their unique surface microstructure-dependent mid-IR optical properties to control the heat losses (2–6). The interaction of microstructures with incident radiation plays an important role in the thermoregulation of animals in nature (5, 9–14). Specifically, the animals make use of the mid-IR wavelength range of 7.5-14 μm, which plays a vital role in heat losses in the ambient environment. The mid-IR wavelengths correspond to the wavelength range where thermal emission takes place as governed by Planck's law (15–17). Moreover, this wavelength region also hosts the window of atmospheric transmission (18), which can lead to substantial radiative cooling in the ambient environment to outer space at 3 K (–270˚C) (19, 20).

Among several examples, polar bears make extensive use of their microscale, hollow fur to trap heat and remain warm even when ambient air temperatures are around -50˚C (1–3). Minks and arctic foxes thrive in arctic environments similarly making use of their fur for warmth (7, 8, 21). In the other extreme, many tropical and equatorial animals remain cool by maximizing heat re-emission in the mid-IR wavelengths. Notably, animals such as the fennec fox (6), the Saharan silver ant (22), and the thistledown velvet ant (23) make use of their surface microstructures to cool down in the otherwise unbearable heat of the deserts they inhabit. The success of nature in optimizing structure-dependent optical and thermal properties has opened the possibilities for developing solutions to human needs to

stay cool or warm (24–27). While human thermoregulation is an important application, the natural microstructures have inspired diverse systems and products for other applications as well, including vapor and IR sensors (28, 29), and for enhanced visible optical control (30).

Figure 1. Animals around the world that make use of microstructure-dependent optical properties to stay warm or cool in extreme environments. From left to right, the figure depicts the thistledown velvet ant (23), *Bistonina biston* butterfly (31, 32), polar bear (1–3, 33, 34), Saharan silver ant (22), fennec fox (6), arctic fox (8, 32, 33), mink (7, 32, 33), bird of paradise (35), and *Troides magellanus* butterfly (4, 32). While the animals come from varying extremes in habitat climate, such as the desert-dwelling thistledown velvet ant, Saharan silver ant, and fennec fox, the tropical *Bistonina biston* and *Troides magellanus* butterflies, and bird of paradise, and the arctic climate polar bear, arctic fox, and mink, they all successfully thrive in their respective habitats due to thermoregulation.

In the midst of all animals that have been studied, butterflies remain attractive due to their near-global geographic spread necessitating some form of adaptation to keep warm or cool in varying habitats (4, 5). However, when it comes to butterflies, the focus of the majority of studies has been on visible to near-IR wavelengths (0.2–2.5 μm wavelengths) where coloration and solar absorption take place. Butterflies heat up their wings by absorbing the heat from the sun, in the ultraviolet (UV) to near-IR wavelengths of 0.2 to 2.5 μm. This heating is essential for facilitating thermoregulation in cold-blooded animals that

rely on habitat, climate, behavioral changes, and evolutionary adaptations. Butterflies regulate their body temperature by controlling their activity level (5, 10, 36–38). Most butterflies are required to attain a body temperature of 20-50˚C, regardless of habitat, in order to be able to fly (39–41).

However, the relevance of surface microstructures in butterfly wings to thermoregulation is incompletely studied because of a dearth of understanding about their optical properties in mid-IR wavelengths that govern thermal emission in the ambient environment. This part of the spectrum (mid-IR) has not yet been systematically examined for butterflies while the effect of mid-IR radiative cooling has attracted much attention for engineering systems (19, 42, 43) as well as for other biological species (22, 25, 44) in the recent literature.

An increasing number of radiative thermal management systems rely on spectral emissivity control for optimal functionality. For instance, the ultraviolet (UV) to near-infrared (near-IR) absorptivity is critical to the functioning of thermophotovoltaics and solar absorbers/collectors, while mid-IR emissivity (in the atmospheric transmission window of 7.5-14 μm) determines the performance of radiative cooling and thermal imaging. However, conventional surface materials have emissivity values that are either high or low throughout the spectrum (20). For example, ceramic materials are typically emissive and metallic materials are typically reflective and not emissive. Consequently, there exists a strong need to develop selective emitters that optimize the optical properties of surfaces in distinct wavelength regions, for distinct applications as necessary. Previous studies have successfully developed a wide variety of systems ranging from vapor sensors to angle-independent reflectors (28, 29, 45). In similar vein as the existing studies, this

present work aims to derive inspiration from nature in optimizing spectral-selective emitters for cooling and heating applications.

While studies of passive selective emitters provide interesting solutions to spectral emissivity control (19, 20, 29, 46, 47), the investigation of dynamic modulation of the spectral emissivity poses new opportunities. This is because passive selective emitters have fixed spectral emissivity profiles (19, 20, 46) and variations in the ambient thermal environment (such as diurnal or seasonal changes) would need to be accounted for by dynamic adjustment of the emissivity. With inspiration from the studies on microstructure-dependent optical and thermal properties in nature (22, 31, 48), one may develop microstructures that offer dynamic optical and thermal control and provide elegant solutions for a multitude of human needs.

CHAPTER 1

1.1 Infrared Optical and Thermal Properties of Butterfly Wings

While visible coloration and solar absorption characteristics have been extensively studied in butterflies (49–53), their mid-IR optical properties and thermoregulation have not (4, 5). Butterfly wings also scatter mid-IR radiation apart from UV, visible, and near-IR radiation (31). This could be due to the presence of unique microstructures that specifically interact with the mid-IR wavelengths. To effectively regulate their wing temperatures, butterflies may have evolved microstructures that affect their solar absorptivity and mid-IR emissivity (5, 12, 54, 55). Analyzing the role of microstructures in thermoregulation could enhance our understanding of the survival mechanisms of butterflies.

I analyze four species (*Archaeoprepona demophoon mexicana*, *Celastrina echo sidara*, *Heliconius sara sprucei*, *Limenitis arthemis astyanax*) from distinct geographical regions ranging from the Ecuadorian rainforests to the Front Range of Colorado's Rocky Mountains, U.S.A. The varying geography is also accompanied by climatic variation ranging from hot and humid in the rainforests to the mountainous cold climates. *A. demophoon* is found in Oaxaca, Mexico through the year, where the air temperature remains around 20-35˚C (warm/dry) (56). *C. echo* is found in abundance in the Rocky Mountains in Colorado, U.S.A. between the months of April and June, with air temperatures between 10-25˚C (cool/dry) (56). *H. sara* is found in Ecuador throughout the year, where the air temperatures are between 25-35˚C (warm/humid) (57). *L. arthemis* is found in Florida, U.S.A. in abundance from March to October, where the air temperatures are around 15-30˚C (moderate/humid) (57). The four species could thus serve as arbiters for species from differing climatic and geographical conditions. These four species also lack optical data in the mid-IR spectrum,

and have not been evaluated for their thermoregulation. With measured and computed optical data, I performed analytical computations and measurements of the thermal performance of these samples to analyze their behavior both in the temperatures of their respective habitats and when placed in a uniform control environment.

1.2 Wing Microstructure and Optical Characterization

The periodic microstructures present in the butterfly wings were analyzed using SEM imaging with a Philips XL-30 microscope of the right dorsal hindwing of each sample. The images shown in **Figure 2** depict the mesh-like microstructures present on the wing scales of the butterfly samples. These microscale-meshes contain periodic ridges linked together by cross-links in the transverse direction.

Periodic microstructures have been hypothesized to correspond to structural coloration of butterfly wing scales (5, 14, 49, 51, 52, 58, 59). Hence, I compared the SEM images from various locations on the butterfly wing samples. From optical imaging, *A. demophoon* and *L. arthemis* wings have distinct structurally colored regions, while *H. sara* appears mostly blue except for the edge of the wing. *C. echo* displays uniform visible coloration. Under SEM imaging, however, the varying regions of the wing all display periodic mesh-like microstructures across the varying colored regions.

The dimensions for the ridge periodicity (a), cross-link periodicity (b), ridge thickness (c), and cross-link thickness (d) were measured from the SEM images and are reported with their respective standard deviation values from measurements at 100 locations across multiple scales for each sample (**Figure 2**). The dimensional parameters vary across the different species, with a ranging between 1-2 μm, b ranging between 0.5-1 μm, c between 0.25-0.5 μm, and d at 0.2 μm. The parameter e was taken from measurements of angled SEM images of the samples, with $e = 1.2 \pm 0.1$ μm, and is comparable to the existing literature (60–62). The biological nature of the samples presents an inherent natural variation in the structural parameters ranging between 0.01-0.2 μm, and could lead to broadband optical and thermal control (45, 63, 64).

Using the microstructures obtained from the SEM imaging of the butterfly wing samples (**Figure 2**), I evaluated the spectral absorptivity/emissivity for the samples by rigorous coupled-wave analysis (RCWA) (20, 65, 66), with custom-modified open-source code (20, 65, 66). The geometric dimensions for computation were gathered from the SEM images as shown in **Figure 2**, and the refractive index and extinction coefficient of chitin were taken from the literature (4, 67, 68). The natural variations and disorder in the structural parameters do not permit perfect periodicity and hence I used the measured average of each of the geometric dimensions of the microstructures in order to impose periodicity.

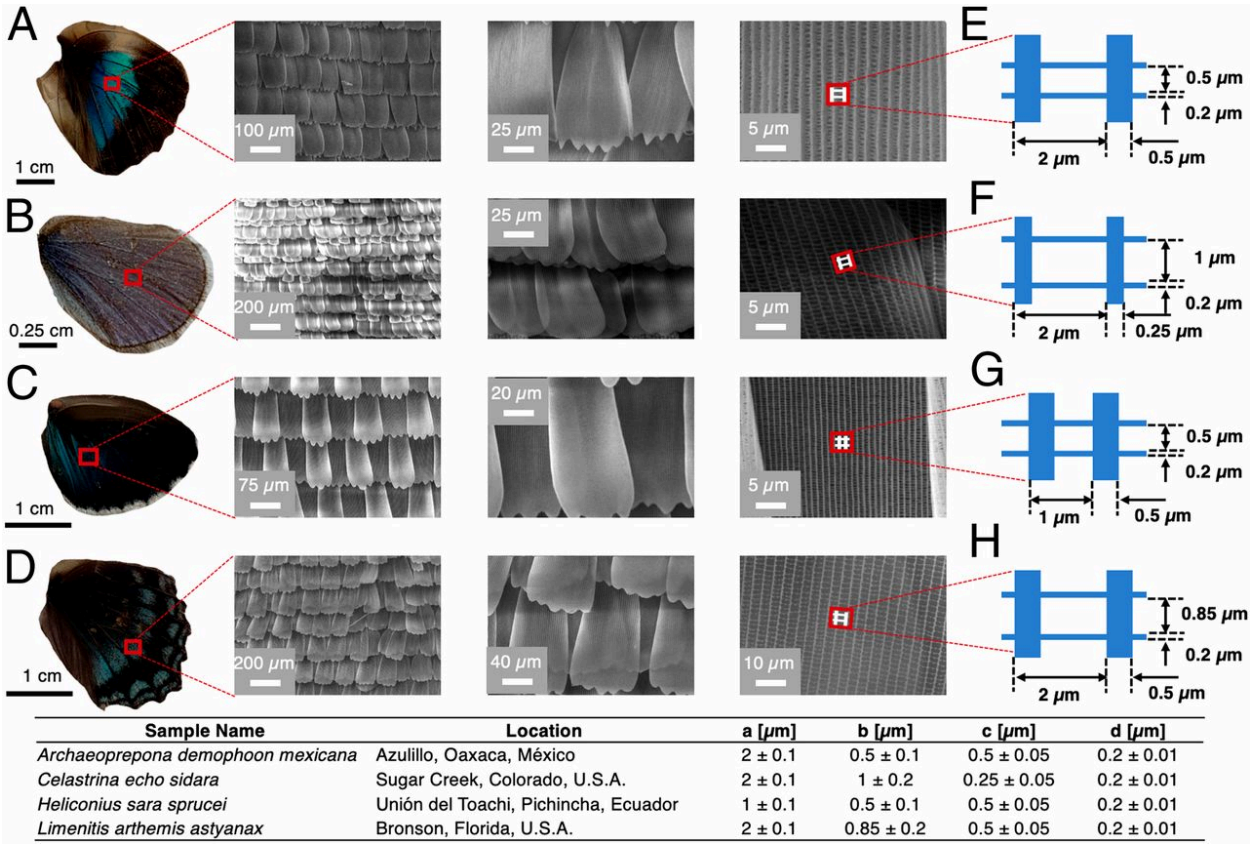

Sample Name	Location	a [μm]	b [μm]	c [μm]	d [μm]
Archaeoprepona demophoon mexicana	Azulillo, Oaxaca, México	2 ± 0.1	0.5 ± 0.1	0.5 ± 0.05	0.2 ± 0.01
Celastrina echo sidara	Sugar Creek, Colorado, U.S.A.	2 ± 0.1	1 ± 0.2	0.25 ± 0.05	0.2 ± 0.01
Heliconius sara sprucei	Unión del Toachi, Pichincha, Ecuador	1 ± 0.1	0.5 ± 0.1	0.5 ± 0.05	0.2 ± 0.01
Limenitis arthemis astyanax	Bronson, Florida, U.S.A.	2 ± 0.1	0.85 ± 0.2	0.5 ± 0.05	0.2 ± 0.01

Figure 2. Optical images and SEM images for the right dorsal hindwings from (*A*) *A. demophoon*, (*B*) *C. echo*, (*C*) *H. sara*, and (*D*) *L. arthemis*. The images depict the presence of periodic microstructures on the wing scales of the butterflies. The periodic microstructures are present as mesh-like features with prominent ridges and cross-links that traverse the ridges (depicted as *Inset* schematics). (*E*–*H*) The microstructures are modeled as a unit cell based on dimensions from the SEM images. Figure reproduced from (69).

The RCWA results (**Figure 3**) for each of these samples depict mid-IR emissivity values ranging between 0.2-0.6, show similar optical behavior across the computation and spectroscopic measurements, and demonstrate the suitability of using a unit cell approximation to model the butterfly wing microstructures.

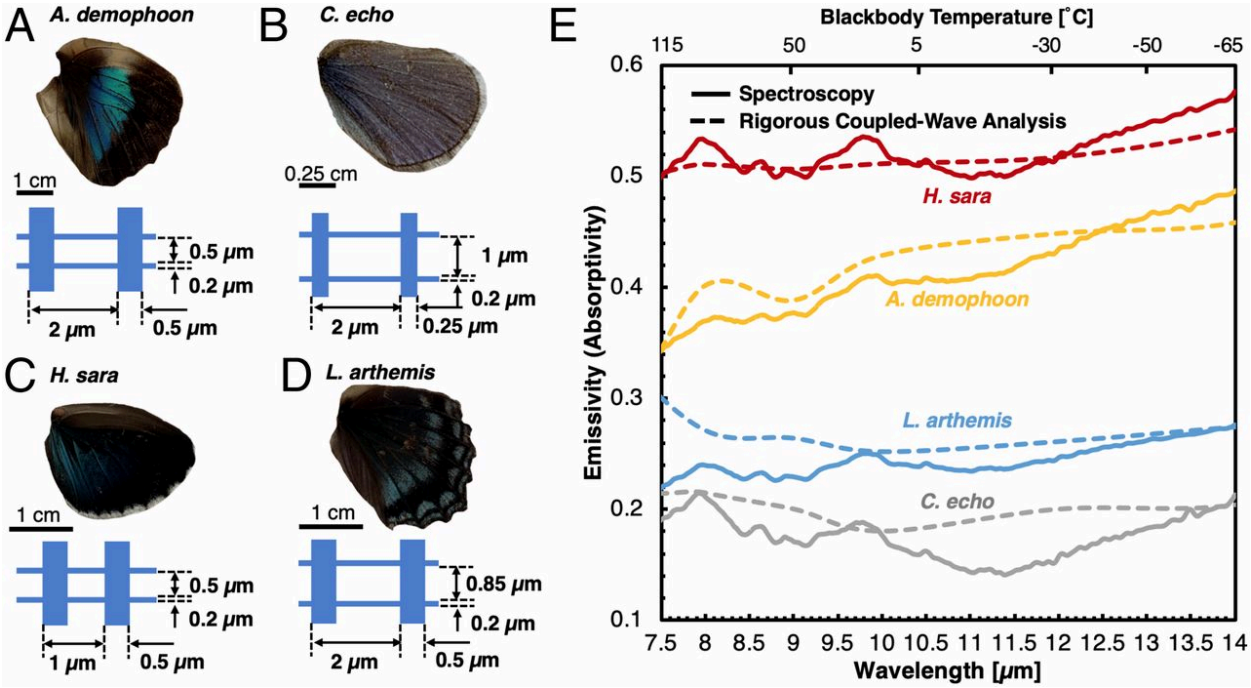

Figure 3. Experimental and computational emissivity data between 7.5 and 14 μm wavelengths (within the atmospheric transmission spectrum) for the sample butterfly species (with schematics for the specimens) for (*A*) *A. demophoon*, (*B*) *H. sara*, (*C*) *C. echo*, and (*D*) *L. arthemis*. (*E*) The emissivity values are computed using RCWA based on structural dimensions (*A*–*D*) from SEM imaging. The emissivity values are plotted with respect to the wavelength and corresponding blackbody temperature [calculated using Wien's law]. The agreement of the computed emissivity with the measured emissivity signifies the accuracy in the assumption of a unit cell approximation for the microstructures present on the butterfly wings. Figure reproduced from (69).

Spectroscopy on the butterflies was carried out on the right dorsal hind-wing of individual specimens of *A. demophoon* (n=5), *C. echo* (n=4), *H. sara* (n=4), and *L. arthemis* (n=9). The measurements provide the emissivity (and consequently the absorptivity, assumed equal to the emissivity by Kirchhoff's Law (17)) as unity minus the sum of the reflectivity and transmissivity (17, 70) (**Figure 4**).

The UV/Vis spectroscopy yields absorptivity/emissivity dips (and hence, reflectivity peaks) for *A. demophoon* (with a reflectivity peak of 0.26 centered at 0.4 μm), *H. sara* (reflectivity peak of 0.11 around 0.37-0.41 μm), and *L. arthemis* (reflectivity peak of 0.32 between 0.38-0.42 μm), with a near-uniform reflectivity of 0.33 for *C. echo*. The solar absorptivity allows for absorption of incident solar irradiation to aid in heating of the butterflies by absorption of incident solar irradiation (9). I observed moderately high solar absorptivity values for all four species (>0.5) within the visible spectrum (0.3-0.7 μm), slowly tapering down to 0.2-0.6 as the near-IR wavelength regions are approached (**Figure 4a**). The average solar absorptivity of the samples contains an uncertainty of ±0.03 for *A. demophoon* and *C. echo*, ±0.05 for *H. sara*, and ±0.04 for *L. arthemis*.

The mid-IR emissivity values were then recorded by Fourier-transform infrared (FTIR) measurements. While the mid-IR emissivity in the wavelengths of 7.5-14 μm remained at 0.2-0.3 for *C. echo* and *L. arthemis*, *A. demophoon* and *H. sara* showed a mid-IR average emissivity of 0.4-0.6 (**Figure 4b**). The average mid-IR emissivity of the samples contains an uncertainty of ±0.03 for *A. demophoon*, ±0.02 for *C. echo*, and ±0.05 for *H. sara* and *L. arthemis*. There are prominent emissivity peaks in the wavelengths of 3 μm and 6 μm due to the presence of chitin (4), seen across all butterfly samples. The mid-IR wavelengths of 7.5-14 μm are critical for thermoregulation by means of mid-IR heat loss (19, 20, 71, 72). Changes in thermal performance of butterfly wings by varying mid-IR emissivity as observed here might aid in thermoregulation of the butterflies.

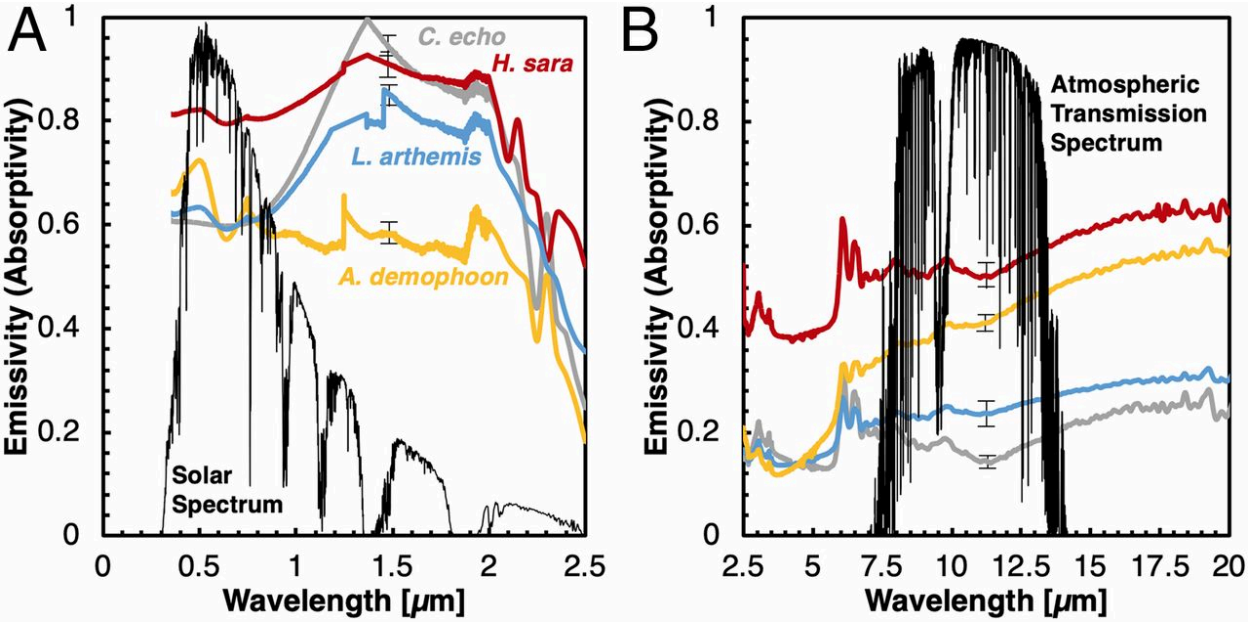

Figure 4. Spectral emissivity (absorptivity) values for the butterfly wing specimens (right dorsal hindwing). (*A*) UV/Vis spectroscopy for *A. demophoon* (yellow), *H. sara* (red), *C. echo* (gray), and *L. arthemis* (blue) measures the spectral emissivity in the wavelength range of 0.3 to 2.5 μm. The results depict moderately high emissivity (absorptivity) values throughout the UV/Vis spectrum, with the average values being around 0.82 for *H. sara*, 0.69 for *C. echo*, 0.67 for *L. arthemis*, and 0.55 for *A. demophoon*. (*B*) FTIR spectroscopy performed in the wavelength range of 2.5 to 20 μm to evaluate the mid-IR emissivity (absorptivity) profiles for the butterfly wing specimens. The results depict mid-IR (7.5 to 14 μm) emissivity (absorptivity) values ranging from around 0.54 for *H. sara* (red), 0.42 for *A. demophoon* (yellow), 0.3 for *L. arthemis* (blue), and 0.18 for *C. echo* (gray), in decreasing order. The spectra are depicted with an overlay of the atmospheric transmission spectrum (7.5 to 14 μm) which aids in re-emission of heat to outer space and, consequently, heat loss. Figure reproduced from (69).

Next I sought to validate the FTIR measurements of mid-IR emissivity by using IR thermography to measure the average mid-IR emissivity of the butterfly wing samples between the wavelengths of 7.5-14 μm. The spectral average mid-IR emissivity values from IR thermography range from a low of 0.24 ± 0.04 for *C. echo*, to a high of 0.52 ± 0.05 for *H. sara*, with intermediate values of 0.33 ± 0.04 for *L. arthemis*, and 0.42 ± 0.05 for *A. demophoon*. The IR thermography results were then compared with the average emissivity (in the 7.5-14 μm wavelength range) taken from FTIR spectroscopy and showed similar values (**Figure 5**).

The IR imaging in **Figure 5** depicts nearly uniform mid-IR emissivity across the right dorsal hind-wing samples, measured as a function of the perceived temperature on the IR map. On the *A. demophoon* wing, I noticed regions of lower emissivity closer to the proximal region, with a nearly uniform higher emissivity present towards the edge of the wing. For the *C. echo* wing, I observed a near-uniform low emissivity across the sample, with a near-uniform high emissivity on the *H. sara* wing barring high emissivity black regions closer to the wing hinge. The *L. arthemis* wing depicts minimal variation in emissivity across the wing moving from the hinge to the edge. The IR imaging thus depicts no clear mid-IR distinction across the visibly distinct colored regions of the samples, and indicates the possibility that different microstructures are responsible for thermoregulation and coloration. The measurement of mid-IR emissivity by IR imaging at a temperature of 69-70 $^{\circ}$C yields comparable results to the FTIR spectroscopy done at 20-22 $^{\circ}$C, depicting negligible variation of optical properties with changes in sample temperature.

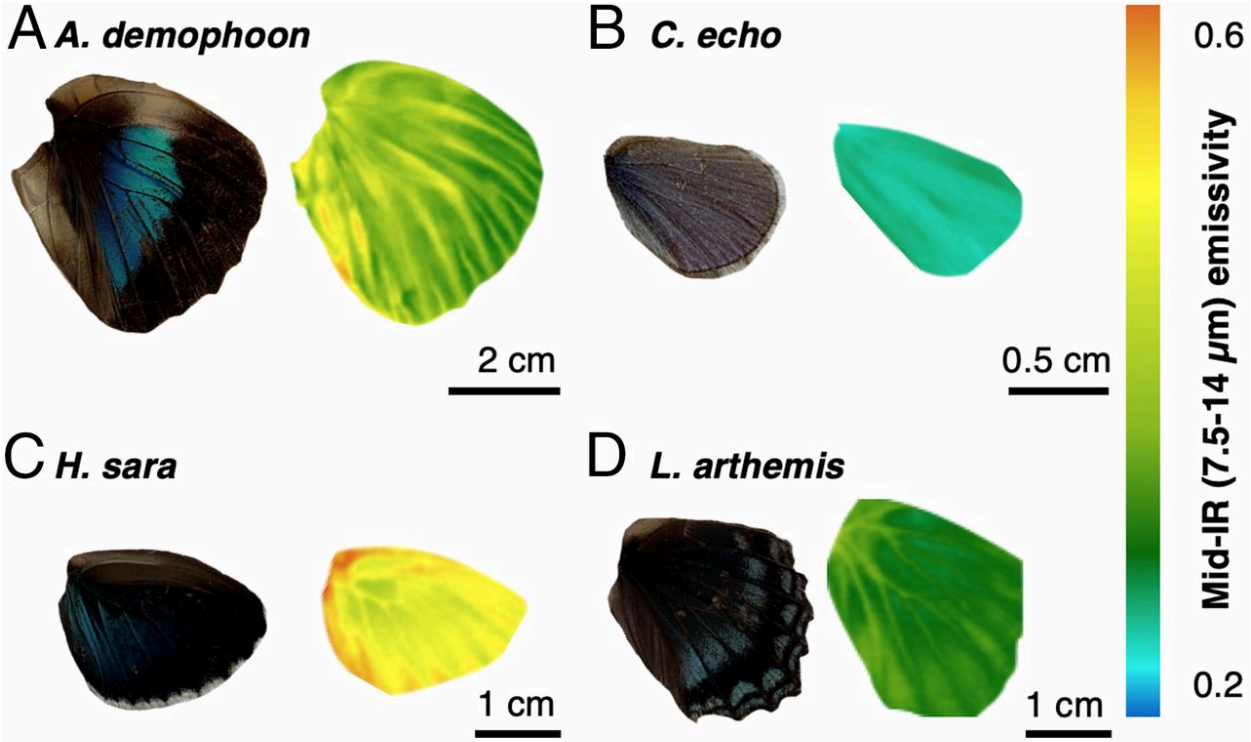

Sample	FTIR (7.5-14 μm)	IR Thermography
A. demophoon	0.42 ± 0.03	0.37 ± 0.05
C. echo	0.18 ± 0.02	0.24 ± 0.04
H. sara	0.54 ± 0.05	0.52 ± 0.05
L. arthemis	0.3 ± 0.05	0.33 ± 0.04

Figure 5. Comparison of average mid-IR emissivity for various right dorsal hindwing specimens between the wavelengths of 7.5 and 14 μm using IR thermography and FTIR measurements for (*A*) *L. arthemis*, (*B*) *C. echo*, (*C*) *H. sara*, and (*D*) *A. demophoon*. The IR mapping presented here depicts variations in emissivity values across the wing specimens, with lower emissivity regions moving toward the blue colors on the map, and higher emissivity regions moving toward the red. While *C. echo* depicts an average mid-IR emissivity of 0.24, the values remain at 0.33 for *L. arthemis* and at 0.42 for *A. demophoon* and reach a value of 0.54 for the *H. sara*. The uncertainty of the measured emissivity values includes the uncertainty in the measurement temperature and the inherent uncertainty of the instrument itself. The results for the 4 species depict close similarity in values for the different methods and validate the measurement observations. Figure reproduced from (69).

1.3 Habitat Climate Correlation

The differing ambient environmental and climate conditions in the habitats of different butterfly species imposes varying radiative demands on the butterflies. I evaluated the butterfly species with the tabulated geometric dimensions of the microstructures present on the wing surfaces from prior literature findings (**Table 1**) (49, 62, 69, 73–78). The dimensions are taken as input parameters for the RCWA computation, along with the refractive index and extinction coefficients of the materials involved (for instance, chitin (4, 67, 68)). The results depict that as one observes the mid-IR wavelengths, the butterflies attained emissivity values around 0.24-0.60 (**Figure 6**). The mid-IR wavelengths of 7.5–14 μm are critical for thermoregulation by means of radiative cooling (9, 19, 20, 71, 72). The varying values of emissivity in the mid-IR wavelengths could thus result in varying thermal performance of the butterfly wings under different environmental thermal conditions. The results depict a possibility for radiative thermoregulation in the butterfly wings by means of structural modulation of spectral emissivity.

Table 1. Geometric dimensions of the microstructures present in the butterfly wings under consideration. The microstructures are predominantly in the form of series of parallel ridges that are connected in the perpendicular direction by cross-links. The dimensional input parameters for the emissivity computation include the periodicity/pitch of the ridges (a) and the cross-links (b), and their respective thicknesses (c and d), and the unit cell height (e). The average mid-IR emissivity as a result of the corresponding RCWA computation is listed against each of the samples.

Sample Name	**Abundance**	**Avg. Ann. Air Temperature [K]** (79, 80)	**a [μm]**	**b [μm]**	**c [μm]**	**d [μm]**	**e [μm]**	**Average Mid-IR Emissivity**	
								RCWA	**FDTD**
Heliconius sara (69)	Year-round	300 ± 5	1	0.5	0.5	0.2	1.2	0.60	0.52
Heliconius doris (49)	Year-round	300 ± 5	1.2	0.6	0.5	0.2	1.2	0.58	0.48
Troides helena (73)	Year-round	303 ± 8	1.2	0.5	0.2	0.1	1.2	0.52	0.43
Hypochrysops delicia (74)	Year-round	303 ± 8	1.5	1	0.2	0.1	1.2	0.51	0.44
Graphium agamemnon (75)	May-September	301 ± 4	1.2	0.7	0.2	0.1	1.2	0.52	0.44
Euploea mulciber (76)	April-October	301 ± 4	1.2	0.8	0.1	0.1	1.2	0.49	0.43
Aricia icarioides (74)	Year-round	303 ± 8	1.5	1	0.4	0.1	1.2	0.52	0.43
Archaeoprepona demophoon (69)	Year-round	301 ± 3	2	0.5	0.5	0.2	1.2	0.51	0.44
Danis danis (74)	Year-round	289 ± 3	2	1.2	0.2	0.1	1.2	0.47	0.41
Ogyris amaryllis (74)	Year-round	288 ± 3	2.1	1.6	0.2	0.1	1.2	0.47	0.40
Allancastria cerisyi (77)	March-July	288 ± 3	1.2	0.7	0.5	0.1	1.2	0.48	0.39
Curetis acuta (78)	April-October	289 ± 3	2	1	0.2	0.1	1.2	0.30	0.28
Jalmenus evagoras (74)	Year-round	288 ± 3	2	1	0.2	0.1	1.2	0.30	0.28
Celastrina argiolus (74)	April-July	288 ± 3	2.1	0.9	0.1	0.1	1.2	0.26	0.26
Limenitis arthemis (69)	March-October	287 ± 3	2	0.85	0.5	0.2	1.2	0.33	0.30
Teinopalpus imperialis (77)	April-July	284 ± 4	1.7	0.5	0.2	0.1	1.2	0.36	0.31
Papilio machaon (62)	March-September	281 ± 5	1.9	1	0.5	0.2	1.2	0.31	0.28
Polyommatus icarus (74)	May-September	284 ± 4	1.7	0.8	0.2	0.1	1.2	0.26	0.24
Arhopala japonica (74)	Year-round	279 ± 2	2.5	1	0.2	0.1	1.2	0.31	0.24
Chrysozephyrus brillantinus (74)	Year-round	271 ± 1	2.5	1	0.1	0.1	1.2	0.29	0.24
Celastrina echo (69)	April-July	274 ± 2	2	1	0.25	0.2	1.2	0.21	0.19

In order to effectively analyze the correlation of optical properties of the butterfly wings with climatic conditions, it would be meaningful to analyze the spectral average emissivity values in the wavelength range of significance. For example, the mid-IR

spectrum (from 7.5 μm to 14 μm wavelengths, the atmospheric transmission window) is expected to offer radiative cooling of the samples by re-emission of heat to outer space (19, 20). The distinct wavelength range for re-emission of heat does not permit a comparison of the overall spectral average emissivity with the environmental climate. I thus compare the average mid-IR emissivity to the annual average air temperature at the corresponding locations.

A distinction among the various habitat climatic conditions of the butterflies was made using the Köppen-Geiger climate classifications (79, 80). The climate classifications consider the monthly average, maximum, and minimum values of air temperature and precipitation across all locations of the world and are used to map the climatic zones of the various locations. The use of monthly average, maximum, and minimum values reduces uncertainties that arise by simple consideration of annual average temperature (due the fluctuation in the values recorded temporally and spatially). The Köppen-Geiger classification acts as a uniform arbiter for the climatic zones of various locations globally and was thus used in the analysis of climatic data in the present study (**Figure 6a**).

A more detailed analysis was then performed by considering the range of air temperature values for each habitat, with the data verified by the Köppen-Geiger classification for the habitats of the butterflies. In order to further avoid spatial variations in the air temperature data, the reported values were taken as the average of the reported data across at least 3 different weather stations within the habitat of each of the butterflies (56, 57). The temporal variations in data were avoided by considering the annual average ambient air temperature for the analysis. A generalized trend for the annual average ambient air temperature values indicate correlations to the latitude of measurement and

the altitude of the location as well (79). For instance, the northern plains in India experience a different air temperature (corresponding to a different climate classification) compared to the elevated regions of the Tibetan plateau, although both locations are along the same latitudes.

I then compared the mid-IR emissivity of the butterfly wings with the corresponding annual average air temperature values in their respective habitats (**Figure 6b**). The mid-IR emissivity values are averaged for each butterfly within the wavelength range of 7.5–14 μm. The results depict a correlation between mid-IR emissivity and annual average air temperature, in which a linear regression fit yields a coefficient of correlation (R) of +0.86. The corresponding coefficient of determination (R^2) is +0.74, indicating that 74% of the changes in the mid-IR emissivity can be explained by changes in the air temperature.

The mean value of the mid-IR emissivity for the entire dataset was 0.40, with a standard deviation of 0.13, with all values ranging between a minimum and maximum of 0.21 and 0.60 respectively (**Figure 6c**). The *Celastrina echo* butterfly displays an average mid-IR emissivity of 0.21, with the average air temperature ranging lesser than 280 K (7˚C) annually (climate classification: Dfc) (56, 57, 79, 80). However, *Heliconius sara* depicts an average mid-IR emissivity of 0.60, with an annual average air temperature of greater than 290 K (17˚C) (climate classification: Af) (56, 57, 79, 80). The variation in mid-IR emissivity with ambient air temperature is hypothesized to correspond to control over the cooling capabilities offered by re-emission of heat from the butterfly wings (31, 69). Higher values of mid-IR emissivity result in greater heat loss from the wings by re-emission of heat to outer space (at a temperature of 3K or –270˚C). The results show a correlation between the annual average ambient air temperature and the mid-IR emissivity that can be

hypothesized to indicate climatic adaptations to heat loss from the butterflies across varying habitats.

I also analyzed the possible correlation between mid-IR emissivity and precipitation, another factor considered in the Köppen-Geiger climate classifications. The analysis showed wide variations in precipitation globally, with no perceived direct link to either latitude or altitude (56, 57). While butterflies exist in diverse habitats with respect to geography and temperature, establishing a morphological connection to adaptations for varying precipitation could provide valuable insight into the survival mechanisms of butterflies. Butterfly wings have been extensively studied for their hydrophobic characteristics (81–83). However, there has been no established evidence of morphological adaptations for precipitation/humidity. I analyzed the annual average precipitation across the various habitats and plotted them on a relative scale from low to high (light blue to deep red) (**Figure 6b**). Based on the analysis, there was no direct link between mid-IR emissivity and precipitation. While butterflies are known to adapt hydrophobic surfaces by variation of surface morphology, the dominant geometric parameters controlling spectral emissivity and hydrophobicity are found to be different (81–83).

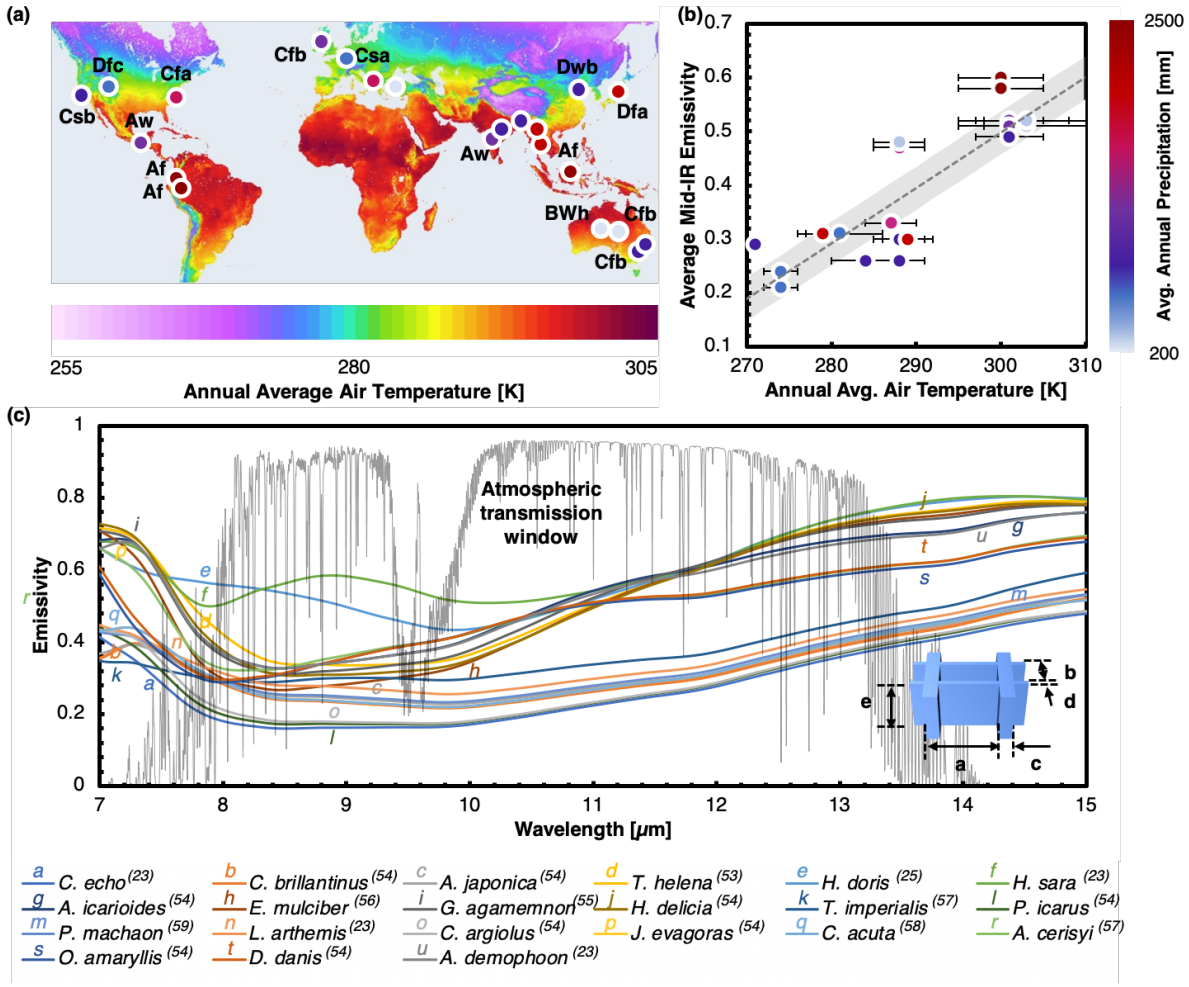

Figure 6. (a) Geographical mapping of the sampled butterfly species around the world. The coloration of the map indicates the annual average ambient air temperature (84). The text adjacent to the data points indicate the habitat-related Köppen-Geiger climate classification (80). The coloration of the data points themselves indicates the annual precipitation received in the habitats of each of the butterflies (56, 57). (b) Correlation of mid-IR emissivity with annual average air temperature. The mid-IR emissivity was averaged over 7.5–14 μm for each butterfly wing computed based on reported microstructure data in the literature (49, 62, 69, 73–78). For a linear fit to the presented data set, there is a correlation of $\varepsilon_{mid\text{-}IR} = 0.01T_{air} - 2.59$ (the dotted line represents the fit, with the gray band representing the 99% confidence interval for the fit). The corresponding coefficient of correlation is +0.86 and the coefficient of determination is +0.74. The correlation between the mid-IR emissivity and the annual average air temperature may be hypothesized to adaptations for thermoregulation by heat loss via re-emission of heat to outer space. (c) Computational emissivity predictions for the wing structures of various butterfly species from around the world. The plot depicts the emissivity in the mid-IR wavelengths, up to 15 μm. The optical property values were computed based on structural dimensions from SEM analyses in existing literature (49, 62, 69, 73–78). The computations were performed using a unit cell approach based on experimental validation in existing literature (69).

While the comparison of the mid-IR emissivity with the annual average air temperature depicted a positive correlation, there remained a need to distinguish between the air temperature values during daytime and during nighttime (56, 57). This was especially important as the butterflies are more active during daylight hours, and comparatively sedentary during night (38). Similar to the earlier analysis, I performed an evaluation of the correlation between the mid-IR emissivity and separated daytime and nighttime annual average temperature values for each of the butterflies (**Figure 7**). The results indicated positive correlations of the mid-IR emissivity to both the daytime (**Figure 7a**) and the nighttime (**Figure 7b**) annual average air temperature data. The coefficient of correlation for the daytime data was +0.82, and that for the nighttime data was +0.87, indicating that 68% and 76% of the variations in the mid-IR emissivity respectively can be explained by variations in the daytime and nighttime annual average air temperature.

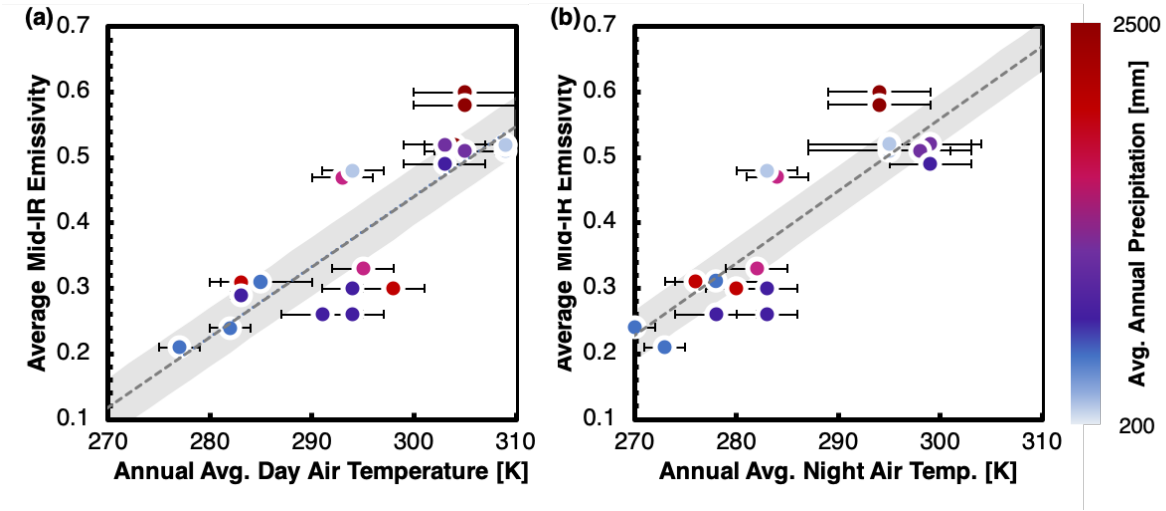

Figure 7. Comparison of mid-IR emissivity with daytime and nighttime annual average air temperature values (56, 57) for the butterflies. (a) Average mid-IR emissivity in the wavelength range of 7.5–14 μm of butterfly wings with respect to the daytime annual average air temperature in their habitats. The linear correlation corresponds to $\varepsilon_{mid\text{-}IR} = 0.01T_{air} - 2.78$, with a coefficient of correlation of +0.82. (b) Average mid-IR emissivity in the wavelength range of 7.5–14 μm of butterfly wings with respect to the nighttime annual average air temperature in their habitats. The linear correlation corresponds to $\varepsilon_{mid\text{-}IR} = 0.01T_{air} - 2.76$, with a coefficient of correlation of +0.87. The gray band in both plots represents

the 99% confidence interval for the fits. The plots use the same method of calculations, the same sources of information, and the same color coding as **Figure 6**.

In similar fashion, it was possible that the comparison of mid-IR emissivity with summer and winter average air temperatures (56, 57). In addition to the seasonal analysis, I also included an analysis of the air temperatures of the months during which each of the butterflies are found in abundance in their habitats. The results (**Figure 8**) indicate observable correlations of the mid-IR emissivity to the summer (**Figure 8a**), the winter (**Figure 8b**), and the abundant months (**Figure 8c**) average air temperature. The coefficient of correlation for the summer data was +0.90, and that for the winter data was +0.82, indicating that 81% and 67% of the variations in the mid-IR emissivity respectively can be explained by variations in the summer and winter average air temperature. It was interesting to observe that the coefficient of correlation was higher for summertime, during which many butterflies are active. The coefficient of correlation for the abundant months was even higher, at +0.95, indicating that 90% of the changes in mid-IR emissivity can be explained by variations in air temperature. These results that suggest that there may exist a strong correlation between the air temperature for the butterflies in their habitats during months they are active at, and their respective mid-IR optical properties.

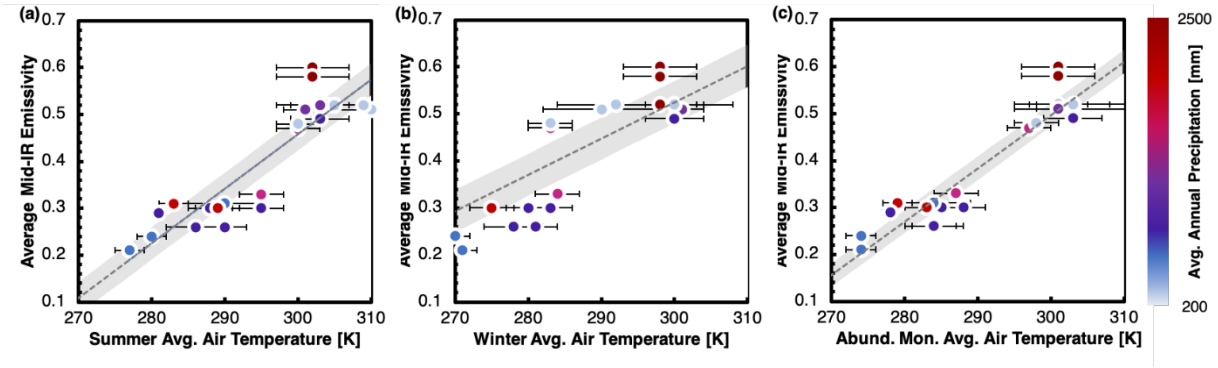

Figure 8. Comparison of mid-IR emissivity with summer, winter, and abundant months average air temperature values (56, 57) for the butterflies. (a) Average mid-IR emissivity of butterfly wings with respect to the summer average air

temperature in their habitats. The linear correlation corresponds to $\varepsilon_{mid\text{-}IR} = 0.01T_{air} - 3.04$, with a coefficient of correlation of +0.90. (b) Average mid-IR emissivity of butterfly wings with respect to the winter average air temperature in their habitats. The linear correlation corresponds to $\varepsilon_{mid\text{-}IR} = 0.01T_{air} - 1.79$, with a coefficient of correlation of +0.82. (c) Average mid-IR emissivity of butterfly wings with respect to the abundant months average air temperature in their habitats. The linear correlation corresponds to $\varepsilon_{mid\text{-}IR} = 0.01T_{air} - 2.91$, with a coefficient of correlation of +0.95. In all the plots, the gray band represents the 99% confidence interval for the fits. The plots use the same method of calculations, the same sources of information, and the same color coding as **Figure 6**.

1.4 Thermal Characterization

I also predicted the steady state temperatures attained by the wings in their respective habitats, with the temperature and solar irradiation data taken for July over the past decade (2007-2017) (56, 57, 85, 86) in Santa María Huatulco, Oaxaca, Mexico for *A. demophoon* (87), and Deckers, Colorado, USA for *C. echo* (56, 57). The temperature data were also compared with other weather stations within their habitats such as Azulillo and San Pedro Pochutla, Oaxaca, Mexico, and Cheesman and Estes Park, Colorado, USA (57, 88). While inherent variation in data exists across multiple sources, the sources I used are considered reliable and should account for locational variation. The data are thus expected to accurately depict the thermal environment of the butterflies, barring other sources of variation in their thermal microhabitat as discussed below. The samples were assumed to be exposed to incident solar irradiation (P_{sun}'') taken to be varying at 580-1000 Wm^{-2} for each location correspondingly. While the butterflies' habitats may offer forest cover or other obstacles to solar irradiation, the butterflies generally bask under direct sunlight (10, 89, 90), and as such, the forest cover can be assumed to have minimal effect on the incident solar radiation. The samples interact with the surroundings by means of convective and conductive losses ($P_{cond+conv}''$), with h_{eff} taken to be 5 $Wm^{-2}K^{-1}$ (for calm air), 10 $Wm^{-2}K^{-1}$ (for a gentle breeze), or 20 $Wm^{-2}K^{-1}$ (for a strong breeze). Increasing convection from the wings to the surrounding air for both butterflies would result in surface temperatures that gradually approach the air temperature. I computed the net radiative power (P_{net}'') using equations from existing literature (20).

The calculations (**Figure 9d, 9e**) show a steady-state wing temperature of 47-51˚C attained by both samples with respect to their corresponding habitats at 12 noon with peak

solar irradiance. The temperatures remained within 20-50˚C and likely aid in survival by thermoregulation (9, 13, 37). The analysis predicts the upper limit for daytime wing temperature as it assumes clear skies, and overpredicts nighttime radiative losses by assuming the entire dorsal wing is exposed to the cold sky. The actual butterflies at nighttime are likely perched under leaves, within rock crevices, in clusters, or with the dorsal side of the wings hidden (38, 91).

The present study analyzes the steady-state wing temperatures of the butterflies at rest. During flight, the energy balance is expected to differ from the rest condition due to changes in the thermal processes associated with the butterflies. While the major changes involve variations in convection, there is also the possibility of metabolic heat generation (89), and other related thermal processes. Flight is expected to increase the convection coefficient (h) for the butterflies due to increase in associated wind velocity over the wings, leading to possible lowering of wing temperatures (**Figure 9d, 9e**). For example, an increase in the h from 10 $Wm^{-2}K^{-1}$ to 20 $Wm^{-2}K^{-1}$ leads to a decrease in the wing temperature for *A. demophoon* and *C. echo* from 50-51˚C to 40-44˚C. Meanwhile, the flight activity itself could lead to increased metabolism and correspondingly a possible increase in the butterflies' temperatures. The temperature prediction for butterfly wings during flight requires further investigations and transient heat transfer analysis with information about convection and metabolic properties (90).

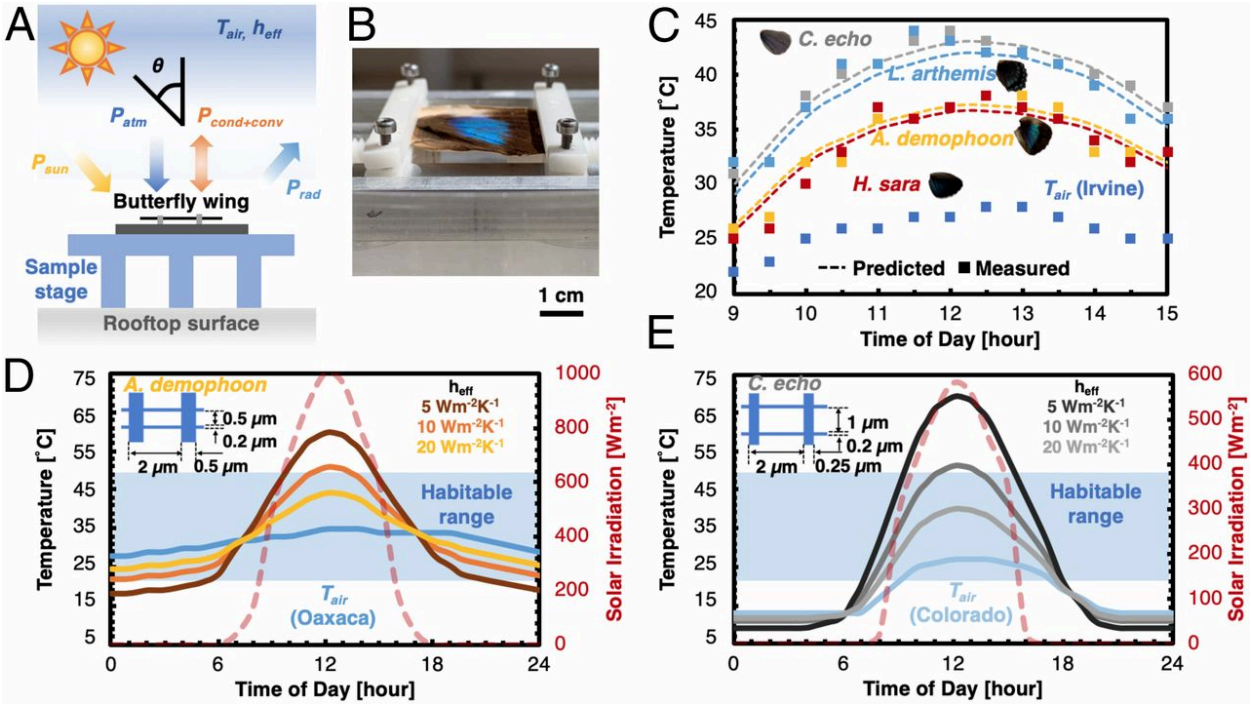

Figure 9. Thermal analysis of butterfly wings. (*A*) Schematic of temperature measurement setup under a control environment with the energy balance considered for the thermal analysis, including incoming heat from the sun and atmosphere, outgoing radiation to outer space, and conductive and convective losses. (*B*) Optical image of temperature measurement on the *A. demophoon* right dorsal hindwing specimen. The specimen is held with clamps placed on a specimen holder mounted on thermal isolation legs. (*C*) Measured temperature comparison of the 4 specimens of butterflies under similar ambient climate conditions in a control environment (Irvine, CA) on July 31, 2018. While *A. demophoon* (yellow) and *H. sara* (red) attained wing temperatures of 37 °C at noon, *C. echo*(gray) and *L. arthemis* (blue) heated up further to 41 to 42 °C, highlighting the role of mid-IR heat losses in warmer climate butterflies. The measurements are validated by computational temperature predictions. (*D* and *E*) Theoretical predictions of the butterfly wing temperatures in their respective habitat conditions for the 2 species, (*D*) *A. demophoon* and (*E*) *C. echo*, depicting a surface temperature of 47 to 51 °C [within the habitable range of 20 to 50 °C] with an effective heat transfer coefficient of 10 $W \cdot m^{-2} \cdot K^{-1}$ (a gentle breeze) at 12 noon. The habitat air temperatures were taken as an average in July for the past decade (2007–2017) and the dashed lines representing the incident solar irradiation. Figure reproduced from (69).

CHAPTER 2

2.1 Butterfly-inspired Micro-tree Designs for Thermal Management

The spectral characteristics of the incident radiation and the spectral properties of the surface materials themselves largely dictate the radiative thermal phenomena affecting surfaces exposed to ambient conditions. Incident solar radiation is governed by Planck's law of radiation based on the solar surface temperature and incident wavelength. The Planck curve for solar radiation at the solar surface temperature of 5778 K results in a peak in incident radiation around the visible and near-infrared wavelengths and explains the heating up of surfaces exposed to wavelengths between 0.2 μm and 2.5 μm (92). Moving to the higher ends of near-infrared and mid- to far-infrared regions, the presence of an atmospheric transmission spectrum (18) aids in the radiative cooling of surfaces by permitting re-emission of heat using outer space as a heat sink at 3 K. The radiative exchange is also dependent om the spectral properties of surface materials. Various surface materials interact in different ways to incident solar radiation, depending on their inherent optical and spectral properties. In general, metallic surfaces have relative permittivity values that vary greatly with wavelength (where relative permittivity is the inherent material property responsible for attenuating electromagnetic waves in a medium). This leads to spectrally varying refractive indices. As a consequence, metallic surfaces have inherently low surface emissivity (with typical values ranging up to 0.3), making them highly reflective over a wide spectral range. Ceramic surfaces are a contrast to metallic surfaces, with largely spectrally stable relative permittivity values. This leads to moderate refractive indices and relatively high spectral emissivity values (with typical values ranging above 0.6). Optically, this leads to metals having a characteristic luster and shine, while

ceramics possess dull surfaces. Thermally, metals often heat up to above-ambient surface temperatures when exposed to solar radiation, with ceramic surfaces cooling down to sub-ambient temperatures. It is thermally interesting and practically useful to have ceramic surfaces that heat up for cheap and localized heating and metallic surfaces that cool down for energy conservation and to avoid mechanical failure and deterioration. This could be done all the while maintaining the desirable malleability and ductility of metals and hardness and brittleness of ceramics. The thermal properties of the surfaces can be controlled by varying the spectral emissivity. A high spectral emissivity/absorptivity between 0.2 μm and 2.5 μm with low infrared emissivity in the atmospheric transmission spectrum between 7.5 μm and 14 μm would lead to the surface absorbing solar radiation, but lacking means to re-emit, leading to the heating up of the surface. A low spectral emissivity for 0.2-2.5 μm with a high emissivity for 7.5-14 μm would lead to radiative cooling of the surface. The spectrally varying nature of heating and cooling demands a level of spectral tuning in surface emissivity that cannot be provided by bare metals or ceramics and suggests modifications to the surface morphology for optimal radiative thermal management. Radiative thermal management could potentially allow for heating or cooling of surfaces without relying on the consumption of electricity or resources for convection or conduction (93–99). This results in cheap alternatives to conventional thermal problems (93–95).

Existing solutions for radiative thermal management typically offer very little spectral control of emissivity (46, 47, 100–103). This can be improved by an increased geometric control over the surface morphology (19, 72, 104). With an increase in the morphological complexity of the structures, there are additional geometrical variables that

offer better tuning and control of the spectral surface emissivity. While there are various factors determining the emissivity, I present a morphology-driven approach to potentially overcome the typical spectral emissivity behavior imposed by the choice of material. I present the use of microscale tree-like structures, or micro-trees in short, as a morphological choice for radiative thermal management, due to the possibility of control over various geometric parameters. This is justified by comparing the micro-trees to pure grating structures, which yield narrower spectral peaks or dips (105). This is also depicted in Figure 10(c), where a pure grating structure (where a duty cycle of b/L nears the lower end of values) offers poorer spectral selectivity compared to a micro-tree structure.

Micro-trees are also widely studied for their biological interest (14, 50, 52), offering spectral-selective emissivity and reflectivity (4, 106–111). The spectral-selective emissivity profiles are a consequence of interference among the periodic surface structures, diffraction at the interfaces, and other optical phenomena (112). Such micro-tree designs have been used for applications ranging from artificial thermal and vapor sensors (28), spectral-selective infrared sensors (113), and flexible, angle-independent reflectors (45), but have not been fully exploited for radiative thermal management applications as yet.

The choice of the micro-tree structures, thus, stems from an aim to achieving increased control over geometric factors affecting spectral emissivity. With multiple periodicities and dimensional factors dictating the design of the structures, they are assumed to present an equally high level of geometrical variables to control and tune the spectral emissivity profile as desired. Because the choice of emissive surfaces is now morphology driven, one is no longer confined by limitations imposed by material choice.

This paves the way for the use of low cost, and low purity materials for radiative thermal management applications.

2.2 Computational Prediction of Optical Properties

Measurement or computation of the surface emissivity can either be done experimentally or via modeling and simulation. Experimental measurements of surface emissivity are typically done with the use of radiometers, spectrometers, such as Fourier transform infrared (FTIR) spectrometers (114, 115), and pyrometric techniques (that measure the emitted radiation from high temperature surfaces) (116) for simultaneous measurement of surface emissivity and temperature. Computational analysis requires the use of calculation of surface emissivity by modeling or simulation.

A simple means of computing the surface emissivity as a function of surface morphology involves the use of surface roughness analysis, using a given root mean squared (RMS) surface roughness. Varying the RMS surface roughness would consequently lead to variations in the spectral emissivity profile. The general trend with an increasing surface roughness is expressed by an increase in overall emissivity values, especially towards the long wavelength regions. While it is possible to compute the emissivity for surfaces of a wide range of surface roughness, it is fairly difficult to differentiate between separate topographies, such as triangular or rectangular structures. This is mitigated by the use of more advanced means for the computation of surface emissivity. Rigorous coupled wave analysis (RCWA) (117) and integral equation method (IEM) (118) are both established methods of surface emissivity computation. Because IEM requires Monte Carlo simulations of Gaussian surfaces and the usage is confined to a few specific surface geometries, I use the RCWA to explore various geometries of micro-trees in this work. RCWA computes the surface emissivity by a rigorous solution of the Maxwell's equations. It

accounts for complex surface geometries and morphologies by considering them as a combination of a finite number of layers stacked on top of each other. This is then followed by an analytical solution along a preferred direction or plane, and a numerical solution along the other two directions or planes. The RCWA considers the geometry of the sample and the optical properties of the materials, such as the relative permittivity (dielectric function) and the magnetic permeability (consequently also being related to the refractive indices of the materials, given by the square root of the product of the relative permittivity and permeability) (65, 66, 119, 120). The RCWA solves for the forward and reverse scattering matrices for incident wave vectors, and gives the reflectivity, transmissivity and emissivity as output values. The reflectivity (ρ) is computed from the reverse scattering, the transmissivity (τ) is computed from the forward scattering, and the emissivity (ε) is given as $\varepsilon = 1-\rho-\tau$ (65, 66, 119, 120). The dimensional details of the tree-like structure, namely the lamellae (branch) spacing, the lamellae thickness, the lamellae width, the ridge (stem) thickness, the ridge height, the number of lamellae, are input to create the geometry for the RCWA. This is followed by the definition of the unit cell parameters, which essentially define the pitch/periodicity of the tree-like structures themselves. The structure is thus defined geometrically as a two-dimensional (2D) structure. The RCWA computation utilized in this work assumes the periodic unit cells to extend infinitely in the third dimension, and also to be replicated infinitely as a periodic feature as well. The computation is thus done for the unit cell, with appropriate Floquet/Bloch boundary conditions to facilitate the periodic nature (65, 66, 119, 120).

The optimization of the structures for use in various applications is done by controlling the geometric parameters (surface morphology). An illustration of the

optimization method used in the work to obtain the desired spectral emissivity is provided by **Figure 11** and **Figure 12**, where the parameters are each varied in turn, while other structural parameters are held constant, to determine the optimized value of each structural parameter.

The focus is now shifted to spectrally controlling the emissivity of the micro-trees for radiative heating and cooling, offering metallic surfaces that cool down and ceramic surfaces that heat up under ambient conditions. While many possible combinations of materials and geometric dimensions exist, I present here the choices of common engineering materials, with optimized geometries for radiative heating or cooling. The choice of the material used for the structures depends on the intended application. I choose a typical ceramic material to optimize and lower its emissivity for radiative heating. Ceramics typically have an overall high spectral emissivity, and I aim to lower the emissivity in the infrared and raise it in the solar region to heat the generally cool ceramic surfaces up. The use of silica (SiO_2) in solar cells has been demonstrated (19, 94) primarily due to the transparent nature of silica and its high transmissivity in the visible region of the solar spectrum. Another possible material is alumina (Al_2O_3), due to its ease of use as a manufacturing material. Alumina also has the advantage of being easily produced by atomic layer deposition (ALD) (121, 122). The microscale structures could potentially be manufactured for practical use by utilizing a base structure provided by patterned silicon, onto which alumina is then deposited by ALD (121, 123, 124). Possible manufacturing methods are reviewed and detailed in previous works (98). The lithography techniques (such as e-beam, dual beam laser interference, or photolithography) have proven particularly successful in this aspect for the manufacturing of patterned silicon base (28,

112). The alumina layer can then be deposited on via ALD. The use of alumina in the aircraft and aerospace industry has also been widely demonstrated (125). The choice of alumina is also bolstered by the closeness of the refractive indices of alumina and silica for the range of wavelengths that are being evaluated (123, 124, 126), with the wavelength-dependence of the refractive indices being evaluated with the help of data from Sellmeier's relation and other spectral correlations (127). Alumina also displays a high level of transmissivity (>80%) for a majority of the spectrum (128, 129) solidifying its application for thermal management and for related solar applications. The added capability of being suitable for mass production and large-scale manufacturing as well (28, 130) makes it a suitable choice of material for designing the optimized radiative heating microstructures. Considering a design of microscale branched grating structures for alumina on a silicon substrate, the requirement for a high emissivity for the wavelengths up to 2.5 μm yields the ridge periodicity as 1 μm, and the lamella periodicity as 3 μm, with 3 lamellae per ridge. The widths of the lamellae are uniformly 0.4 μm, and their thicknesses 1 μm, with the lamellae extending infinitely along each ridge, of width 0.1 μm. The emissivity spectrum for this structure is given in **Figure 10**, with optical data based on bare alumina (131). The purpose of the micro-trees is validated when compared to bare alumina, as bare alumina yields a relatively flat, high emissivity over the entire spectrum. This would not serve the purpose of a surface with a tunable emissivity. The ceramic micro-trees could thus potentially offer radiative heating for a typically cool ceramic surface.

The second combination of materials presented in the analysis considers aluminum micro-trees on a silicon substrate. The aluminum microscale structures could also potentially be manufactured for practical applications by utilizing a patterned silicon base

structure, onto which the aluminum layer is then deposited by vapor deposition methods, or other comparable means (28, 112, 130). The patterning of the silicon base is done potentially by lithography (dual beam interference or e-beam lithography) or other methods (28, 112). Deposition, by evaporation or chemical vapor deposition (CVD) could then be used to manufacture the aluminum layer on the silicon base. Aluminum is a typical metal, and its low spectral emissivity leads to heating up of its surface. I investigate the possibility of using aluminum micro-trees to achieve radiative cooling of a typically hot aluminum surface. The optimized geometry for radiative cooling purposes with the requirement for a high emissivity between the wavelengths of 7.5 and 14 μm yields a ridge periodicity of 10 μm, and a lamella periodicity of 8 μm, with 3 lamellae per ridge. The spacing between two adjacent lamellae is 4 μm, yielding a lamella thickness of 4 μm. The lamellae are 2 μm wide from end to end, with the ridges being 1 μm wide. The emissivity profile of the aluminum micro-tree structure, in **Figure 10**, is based on optical data for bare aluminum (132). Bare aluminum displays a flat, low emissivity profile, rendering it relatively futile as a surface with tunable emissivity, and resulting in a hot bare aluminum surface. The metallic micro-trees, however, offer radiative cooling, unlike the bare metallic surfaces.

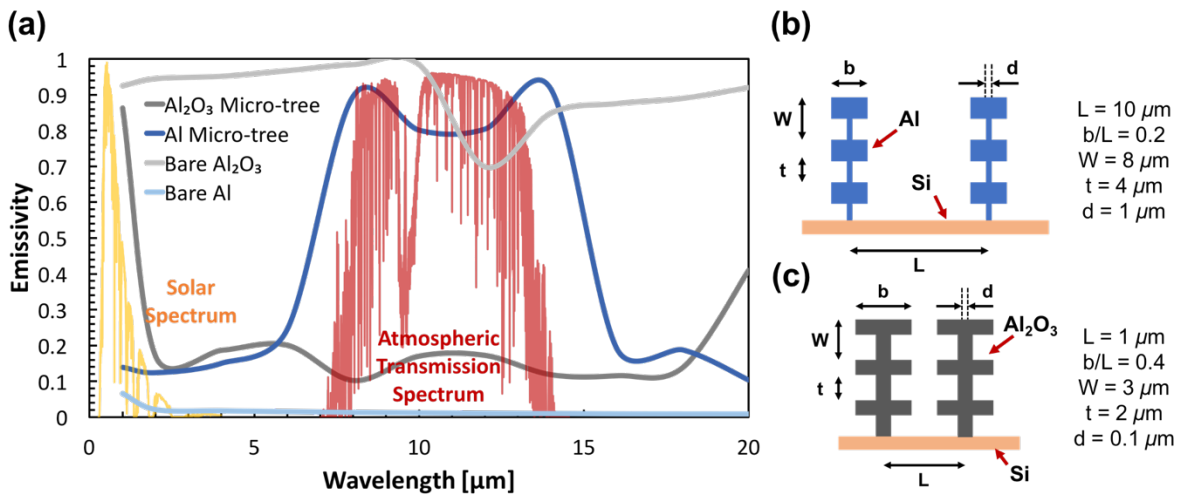

Figure 10. Various designs of micro-trees for radiative thermal management applications. (a) Emissivity spectrum for the alumina micro-tree, with a ridge periodicity (L) of 1 μm and a lamella periodicity (W) of 3 μm. Bare alumina absorbs in all wavelengths, which is mitigated by micro-trees, that achieve the optimal scenario acting as a reflector in most wavelengths, and an emitter in the infrared spectrum, making it suitable for thermal management applications. Bare alumina is rarely used as a surface coating and its surface properties might not remain constant due to non-ideal real-life conditions. Emissivity spectrum for the aluminum micro-tree, with a ridge periodicity (L) of 10 μm and a lamella periodicity (W) of 8 μm. Bare aluminum behaves much as bare alumina does, though by reflecting in all wavelengths, negates its suitability for thermal management applications. The spectra are superposed on the solar spectrum in the visible region (92), which is responsible for radiative heating, and the atmospheric transmission spectrum (18), which is responsible for radiative cooling in the ambient environment. (b) The optimized dimensions of the aluminum micro-trees for radiative cooling, with a ridge periodicity (L) of 10 μm, a lamella periodicity (W) of 8 μm, lamella width (b) of 2 μm, and a lamella spacing (t) of 4 μm. (c) The optimized dimensions of the alumina micro-trees for radiative heating, with a ridge periodicity (L) of 1 μm, a lamella periodicity (W) of 3 μm, lamella width (b) of 0.4 μm, and a lamella spacing (t) of 2 μm. Figure reproduced from (20).

The emissivity spectrum of these micro-tree structures remains high in the visible wavelengths for heating or follows the peak in the atmospheric transmission spectrum for radiative cooling. The radiative heating structures offer a high emissivity up to wavelengths around 2.5 μm, with relatively low emissivity values for all other spectral regions. The radiative cooling structures have an emissivity rising roughly at 7.5 μm and dropping off at around 14 μm. The emissivity through the rest of the spectrum is low, maintaining a value of around 0.2 for most of the visible region. This leads to a high reflectivity for the surface

over all wavelengths, except for those between 7.5 and 14 μm, effectively aiding the reemission of radiation over the infrared spectrum, while avoiding heat generation by reflecting incident radiation over other wavelengths. The emissivity spectrum of the micro-tree structures also roughly follows the trend of existing radiative thermal management solutions (19), at times offering better results with respect to the far-infrared regions as well.

The adaptability of the micro-tree structures used for thermal management to various emissivity requirements is aided by flexibility in varying the dimensions of the structures. With an example of the aluminum micro-tree structures, it is aided by the variation of the ridge spacing and the lamella spacing. The rise and fall in the high emissivity region are controlled by the ridge spacing, because of the interference of photons over multiple adjacent ridges. Increasing the ridge spacing for the aluminum micro-trees leads to a delayed rise and fall in the high emissivity region, and a decrease in the ridge spacing of the aluminum micro-trees yields an earlier rise and fall in the high emissivity region, as shown in **Figure 11(b)**. Similarly, the overall emissivity profile is controlled by the lamella width, shown in **Figure 11(c)**. Varying the width of the lamellae varies the wavelength response due the interference of photons between adjacent lamellae. Increasing the lamella width leads to a loss in spectral-selective emissivity characteristics, leading to the emissivity profile approaching that of bare aluminum. The lamella spacing controls the height of the emissivity peak in the high emissivity region. The optimal lamella spacing for the aluminum micro-trees is found to be at 4 μm, as demonstrated in **Figure 11(d)**. Similarly, variations in the number of lamella lead to variations in the height of the emissivity peak in the case of the aluminum. The optimal number of lamellae for radiative

cooling is found to be at 3 lamellae per ridge, with lesser and more lamellae leading to a lowering of the emissivity peak. The tunable nature of the photonic structures is similarly reported in literature (124), with variations in the periodicity of the structures yielding varying reflectance peaks.

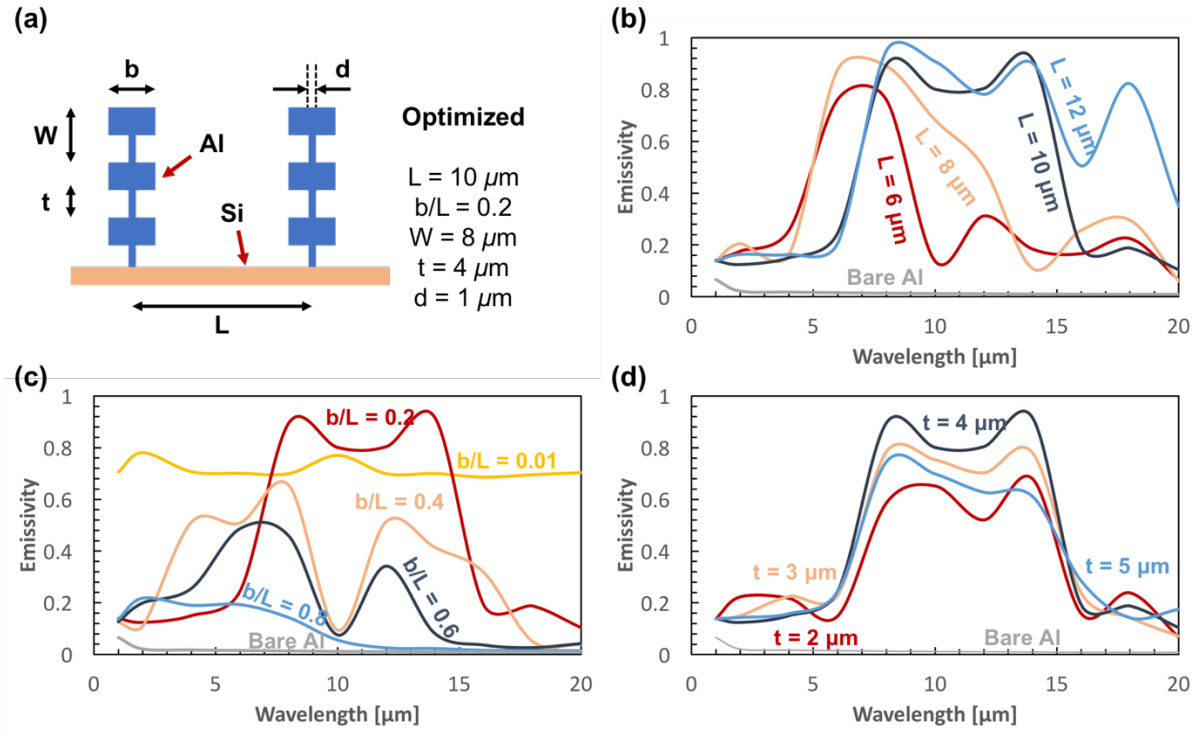

Figure 11. Tunable nature of the metallic micro-tree structures aided by the variation of the ridge and lamella spacing. (a) Optimized dimensions for aluminum micro-trees for radiative cooling applications, with a ridge periodicity (L) of 10 μm, a lamella periodicity (W) of 8 μm, lamella spacing (t) of 4 μm, and lamella width (b) of 2 μm. (b) Variation in ridge periodicity of aluminum micro-tree yielding a delayed rise/drop in high emissivity (caused by increased spacing), or an early rise/drop (caused by decreased spacing). (c) Variation in width of lamellae of aluminum micro-tree leading to changes in the overall spectral emissivity profile, with an increased width leading to the emissivity profile approaching that of bare aluminum. (d) Variation in lamella spacing leading to changes in the height of the emissivity peak. The optimal value for lamella spacing for the aluminum micro-trees is found to be at 4 μm. The colors of the various plot lines signify different geometric dimensions as denoted in the plots next to each line. Figure reproduced from (20).

Similar to the morphological adaptability of the metallic micro-trees, the emissivity profile of the ceramic micro-tree structures is also geometrically tunable in nature. Increasing the ridge spacing for the alumina micro-trees leads to a delayed rise and fall in

the high emissivity region, and a decrease in the ridge spacing of the alumina micro-trees yields an earlier rise and fall in the high emissivity region, as shown in **Figure 12(b)**. Similarly, the overall emissivity profile is controlled by the lamella width, shown in **Figure 12(c)**. Increasing the lamella width leads to a loss in spectral-selective emissivity characteristics, leading to the emissivity profile approaching that of bare alumina. The lamella spacing controls the height of the emissivity peak in the high emissivity region. The optimal lamella spacing for the alumina micro-trees is found to be at 2 μm, as demonstrated in **Figure 12(d)**. Similarly, variations in the number of lamella lead to variations in the height of the emissivity peak in the case of the alumina/silicon. The optimal number of lamellae for radiative cooling is found to be at 3 lamellae per ridge, with lesser and more lamellae leading to a lowering of the emissivity peak.

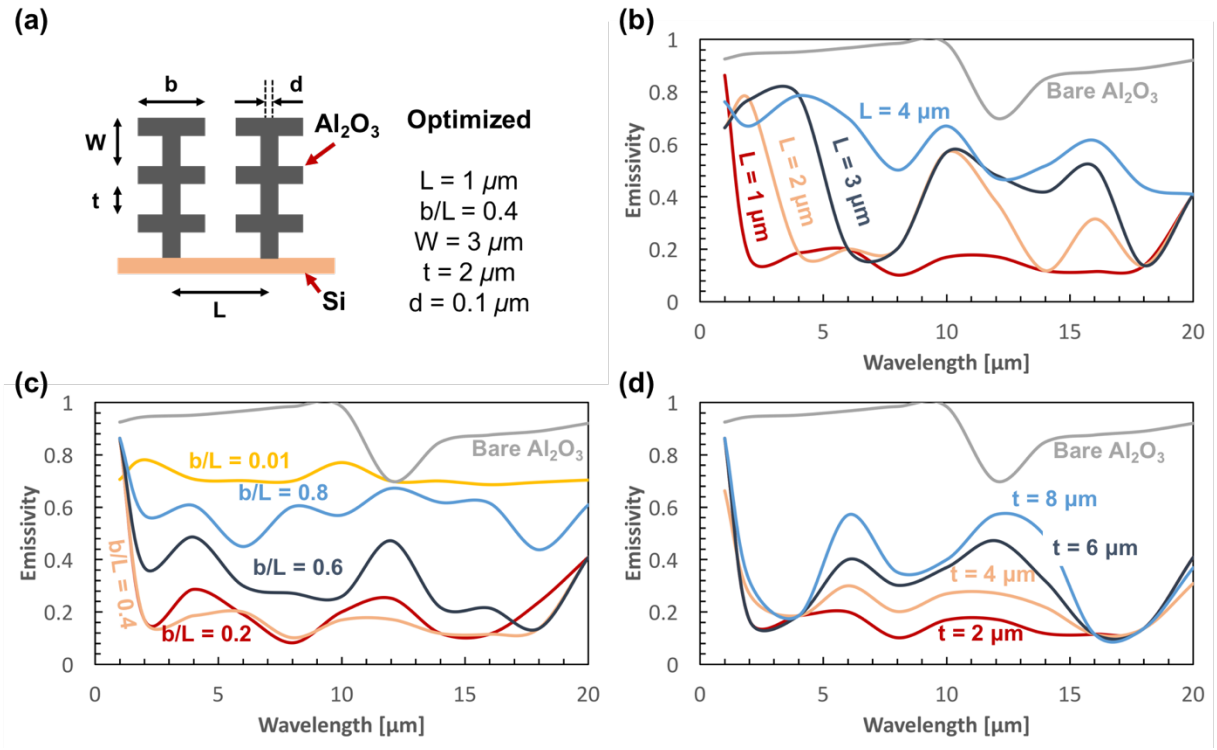

Figure 12. Tunable nature of the ceramic micro-tree structures aided by the variation of the ridge and lamella spacing. (a) Optimized dimensions for alumina micro-trees for radiative heating applications, with a ridge periodicity (L) of 1 μm, a lamella periodicity (W) of 3 μm, lamella spacing (t) of 2 μm, and lamella width (b) of 0.4 μm. (b) Variation in ridge periodicity of alumina micro-tree yielding a delayed drop in high emissivity (caused by increased spacing), or an early drop (caused by decreased spacing). (c) Variation in width of lamellae of alumina micro-tree leading to changes in the overall spectral emissivity profile, with an increased width leading to the emissivity profile approaching that of bare alumina. (d) Variation in lamella spacing leading to changes in the height of the emissivity peak. The optimal value for lamella spacing for the alumina micro-trees is found to be at 2 μm. The colors of the various plot lines signify different geometric dimensions as denoted in the plots next to each line. Figure reproduced from (20).

Variations in the angle of incidence affecting the emissivity profile must be considered in order to minimize adverse effects due to angular changes. **Figure 13** demonstrates the angular variations of spectral emissivity for the metallic and ceramic micro-trees, showing minimal variations in the emissivity peak with wavelength over a wide range of angles, with an abrupt drop as the angle of incidence approaches near-parallel.

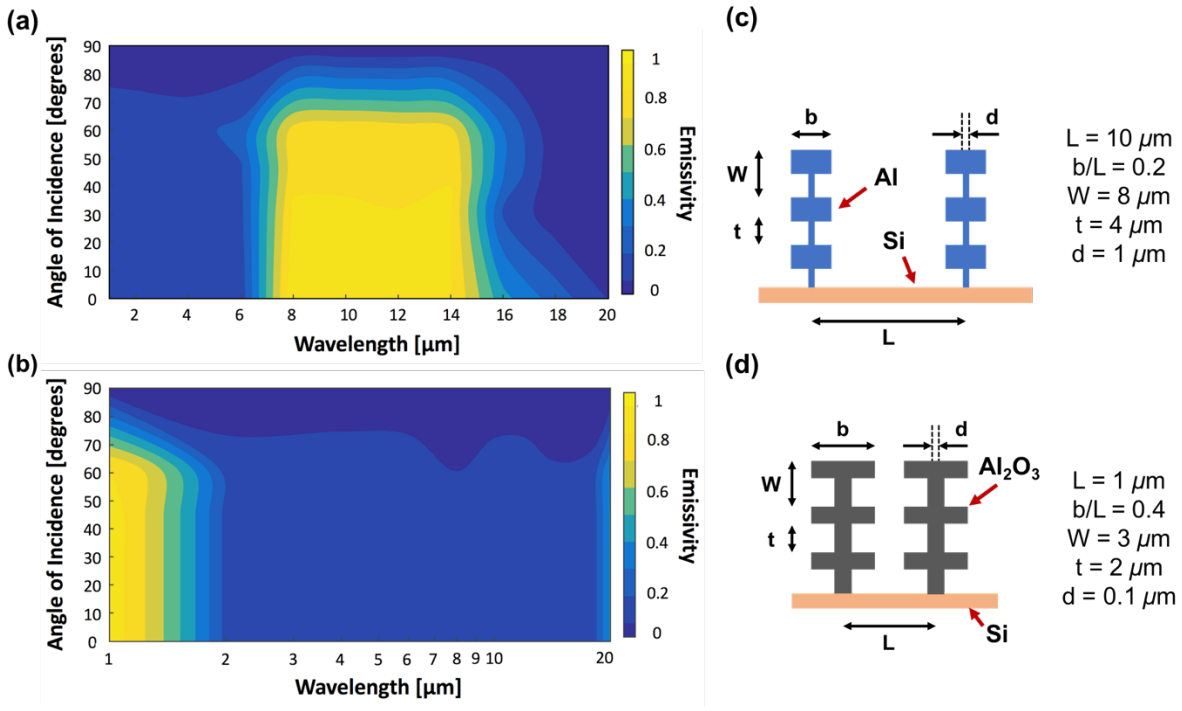

Figure 13. Angle dependent emissivity spectra for the metallic and ceramic micro-trees. (a) Angle dependent data for the aluminum micro-trees for angles of incidence varying from 0 to 89.9 degrees, demonstrating the sustenance of the

emissivity peak between 7.5 μm and 14 μm for a wide range of angles. (b) Angle dependent data for the alumina micro-trees for angles of incidence varying from 0 to 89.9 degrees, showing a sustained emissivity peak for the visible wavelengths, with a low emissivity elsewhere. The emissivity profile remains fairly invariant for a majority of the angular range, displaying a sudden decay as the angles approach 90°, indicating effective use of the micro-tree structures for most applications with varying angles of incidence, with none to minimal loss in spectral emissivity characteristics. (c) The dimensions and schematic of the optimized radiative cooling aluminum micro-trees. (d) The dimensions and schematic of the optimized radiative heating alumina micro-trees. Figure reproduced from (20).

The results show a tunable periodic microstructure that effectively reemits incident radiation from the surface through the atmospheric transmission spectrum or absorbs selectively purely within the visible wavelength region. While the high emissivity region for radiative heating corresponds to incoming solar radiation, with a low infrared emissivity to maximize surface heating, the high emissivity regions correspond to the thermal regions of the wavelength for radiative cooling, thus avoiding the detrimental effects of undesirable heat generation on the surface. The surface also exhibits a high reflectivity for all other regions of the spectrum, thus effectively avoiding the heating of the surface by any incident radiation on it. The adaptability of the structures to various requirements posed on them is aided by the flexibility in their design and dimensions, with varying periodicities in different aspects of the structure resulting in the tuning of emissivity in different regions of the spectrum. The tunable nature and spectral control present the possibility of having selective high emissive metallic micro-trees compared to very low emissivity bare metallic surfaces, or of selective low emissivity ceramic micro-trees compared to typically high emissivity bare ceramic surfaces.

2.3 Prediction of Thermal Properties in the Ambient Environment

Assuming that the surface is exposed to incident radiation with a clear sky at all times, the power balance on the surface is a combination of the incident solar radiation (P_{sun}), the incident atmospheric thermal radiation (P_{atm}), the radiation emitted by the surface (P_{rad}), and the conductive and convective losses from the surface ($P_{cond+conv}$), as given by Eq. (1) (47). The surface temperature is denoted as T, with the ambient temperature at T_{amb}.

$$P_{rad}(T) - P_{atm}(T_{amb}) - P_{sun} + P_{cond+conv} = 0 \quad (1)$$

The radiation emitted out from the surface is computed by multiplying the spectral radiance of a black body with the emissivity of the surface, integrated over the hemisphere, as in Eq. (2).

$$P_{rad}(T) = \int \cos\theta \, d\Omega \int_0^{\infty} I_{BB}(T, \lambda)\varepsilon(\lambda, \Omega)d\lambda \quad (2)$$

$$\int d\Omega = \int_0^{\pi/2} \sin\theta \, d\theta \int_0^{2\pi} d\phi \quad (3)$$

$$I_{BB}(T, \lambda) = \frac{2hc^2}{\lambda^5(e^{hc/\lambda k_B T} - 1)} \quad (4)$$

Eq. (3) gives the angular integral over the hemisphere, while Eq. (4) computes the radiance of a blackbody at a temperature T, with λ being the wavelength, h representing the Planck constant, c the velocity of light in vacuum, and k_B the Boltzmann constant.

The incident atmospheric thermal radiation is computed similar to Eq. (2), factoring in the emissivity of the atmosphere (ε_{atm}), with t being the atmospheric transmittance along the zenith.

$$P_{atm}(T_{amb}) = \int \cos\theta \, d\Omega \int_0^{\infty} I_{BB}(T,\lambda)\varepsilon(\lambda,\Omega)\varepsilon_{atm}(\lambda,\Omega)d\lambda \quad (5)$$

$$\varepsilon_{atm}(\lambda,\Omega) = 1 - t(\lambda)^{1/\cos\theta} \quad (6)$$

The incident solar power absorbed by the surface is computed in Eq. (7), where θ_{sun} is the incident angle. The solar irradiance is taken for an air mass of 1.5 (AM1.5) (133).

$$P_{sun} = \int_0^{\infty} I_{AM1.5}(\lambda)\varepsilon(\lambda,\theta_{sun})\cos\theta_{sun}\, d\lambda \quad (7)$$

Conductive and convective heat losses from the surface are computed in Eq. (8), where h_c is the net heat transfer coefficient for conduction and convection from the surface to its surroundings.

$$P_{cond+conv} = h_c(T - T_{amb}) \quad (8)$$

The solar angle is assumed to be 30°, with the h_c at 10 W/m^{2}K. The model also assumes that the sky is clear throughout the day, and that the effects of changes due to wind are neglected, to maintain a uniform value for the heat transfer coefficient.

The hourly temperature profile is modeled for daylight hours with standard conduction and convection assumptions for atmospheric conditions, as illustrated in Figure 5. The performance of the metallic micro-tree structures shows a surface that is cooler by nearly 9 K as compared to the ambient, while being ~10 K cooler than bare metallic surfaces. While bare aluminum reaches a peak temperature of around 301 K, the aluminum micro-trees reach a temperature of around 291 K. The alumina micro-tree reaches a temperature roughly 2-3 K higher than ambient at around 302 K, compared to bare alumina, which reaches a surface temperature of around 6 K below ambient around 294 K.

Overall, the aluminum micro-tree structures maintain a surface temperature that has a cooling power of around 136 W/m^2, while the alumina micro-trees have a heating power of around 12 W/m^2. The low emissivity of aluminum over the entire incident spectrum causes it to heat up, and the high emissivity of alumina causes it to cool down. However, the tailored and optimized aluminum micro-trees cool down, and the alumina micro-trees heat up.

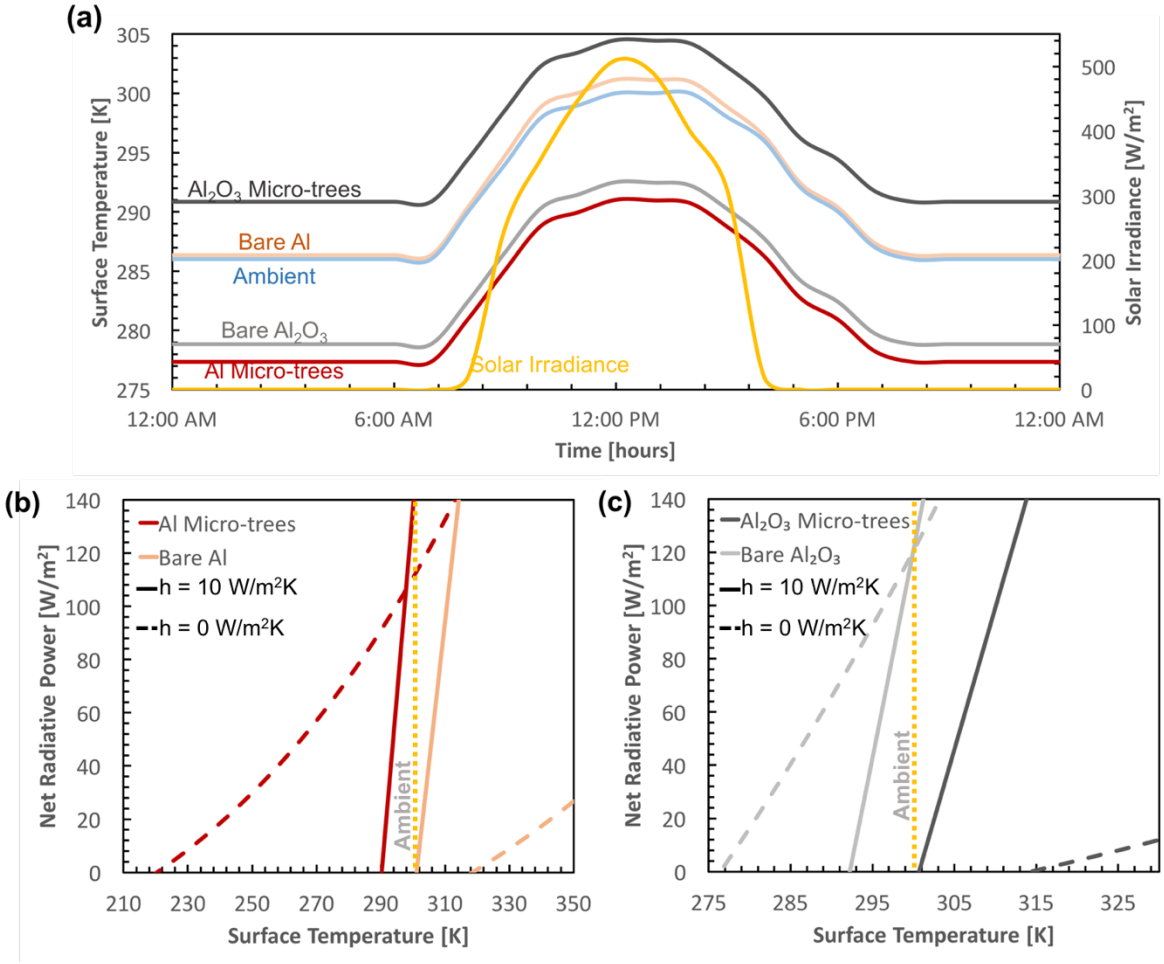

Figure 14. (a) Modeling of the performance of the micro-tree structures for a clear sky with no wind, superposed on the solar irradiance (133). Data compared with polished bare alumina and bare aluminum. Metallic surfaces, such as bare aluminum, have very low spectral emissivity (and are highly reflective), and typically heat up around 1-2 K above ambient, while the emissivity control offered by the morphological tuning of aluminum micro-trees leads to radiative cooling of the surface to around 9 K below ambient at peak solar irradiance. Ceramic surfaces, such as bare alumina, have

generally high spectral emissivity values, and typically have sub-ambient surface temperatures (around 6 K below ambient), while the morphologically controlled emissivity of alumina micro-trees offers radiative heating and a surface temperature of around 2-3 K higher than ambient. (b),(c) Comparison of net radiative power of microstructures for radiative thermal management with bare alumina and bare aluminum, indicating a net power of roughly 136 W/m^2 for the radiative cooling micro-trees for h = 10 W/m^2K, a value around 112% higher as compared to bare metallic surfaces, leading to the radiative cooling of metallic micro-tree surfaces as compared to bare metallic surfaces. The metallic micro-trees consequently behave much as bare ceramic surfaces do, thermally. The radiative heating micro-trees have a substantially lower net power than bare ceramic surfaces, with the net power being around 12 W/m^2 below zero (36-40% lower than bare alumina) for h = 10 W/m^2K. This leads to a heating up of ceramic micro-tree surfaces, as opposed to the cooling down of bare ceramic surfaces, with a higher net power, making them behave thermally much as bare metallic surfaces do. Figure reproduced from (20).

While the assumptions for conduction and convection offer practical results for thermal analyses, a comparison is done varying the coefficient of heat transfer for conduction and convection (h_c) for values at 0 $Wm^{-2}K^{-1}$ and 10 $Wm^{-2}K^{-1}$. The results for the analysis illustrate a more ideal scenario as the h_c value decreases, with the surface temperature substantially changing with respect to the ambient. For radiative cooling, an h_c value of 10 $Wm^{-2}K^{-1}$ yields a nearly 9 K drop from the ambient, while an h_c value of 0 $Wm^{-2}K^{-1}$ leads to a nearly 85 K drop from the ambient conditions. For radiative heating, an h_c value of 10 $Wm^{-2}K^{-1}$ yields a nearly 2-3 K rise from the ambient, while an h_c value of 0 $Wm^{-2}K^{-1}$ leads to a nearly 15 K rise from the ambient conditions. The scenario of zero conduction and convection remains ideal, however, and the extremely high sub-ambient cooling/heating consequently remains an ideal condition as well.

CHAPTER 3

3.1 Ant-inspired Crumpled Materials for Dynamic Optical and Thermal Control

The use of complex systems and material surfaces in aerospace applications imposes a need for careful consideration of thermal management. This is especially true considering the need for maintaining human comfort while attaining optimal system performance in adverse environmental ambient conditions. While several examples exist for active thermoregulation (134, 135), the inherent use of resources to allow for the thermoregulation can be burdensome. To mitigate this, possible solutions include passive regulation by means of radiative exchange using selective emitters.

For all surfaces exposed to the ambient environment, the solar spectrum between the wavelengths of 0.2 μm and 2.5 μm can affect the functioning of radiative heating relying on solar absorption (136). Meanwhile, the mid-IR wavelength range between 7.5 μm and 14 μm (the atmospheric transmission window) (18) can be utilized for radiative cooling relying on IR emission (19, 42, 71, 72, 104, 137). Distinct spectral ranges for heating and cooling impose the need for spectral-selective modulation and control of emissivity by engineered surfaces. Selective emitters can control the emissivity across distinct regions of the electromagnetic spectrum and allow optimal solutions to systems where a unique wavelength response is desired, and has been successfully used in applications for photonics/optoelectronics (138, 139), infrared (IR) imaging, and thermoregulators (140).

There are various emissivity optimization techniques for selective emission/absorption, from heterostructure (metallic and semiconductors/oxides) multilayers to photonic structures, gratings, and other architected surface features (19, 42,

72, 104, 137). The techniques offered by existing solutions aim to optimize the emissivity spectra within the atmospheric transmission window from 7.5-14 μm wavelengths. However, a vast majority of the selective emitters rely on rigid materials and surfaces and have a limited scope of use. The use of flexible materials can offer morphology-controlled (20) dynamic emissivity changes and thus widen the spectral range of use.

Transient variations in the ambient environments necessitate dynamic emissivity control. Existing dynamic control solutions are based on phase change materials (141–143) and consequently require large temperature variations for emissivity modulation, and curtail the operation to specific temperature ranges. Reconfigurable surfaces address such limitations on temperature. Several solutions exist for dynamic control of IR properties, such as the use of wave-patterned bimetallic layers that offer strain-induced IR emission control (144). However, the use of the Bragg stacks and bimetallic layers only offers control over narrow spectral bands and their reconfigurability is limited due to the use of multilayer structures. There is a distinct lack of fully reconfigurable solutions for emissivity control, which I aim to achieve with the use of a two-dimensional material integrated with a flexible material platform.

Here I present a solution for surface topography-driven emissivity control by crumpled graphene (145), where periodic crumpled features on the surface of the graphene to control the radiative properties such as emissivity. The crumpled graphene derives its surface morphology from the triangular hair structures of the Saharan silver ant (**Figure 15**). The Saharan silver ant utilizes the high mid-IR emissivity and solar-spectrum reflectivity offered by these hairs to remain cool even in the extreme heat of the Sahara Desert (22).

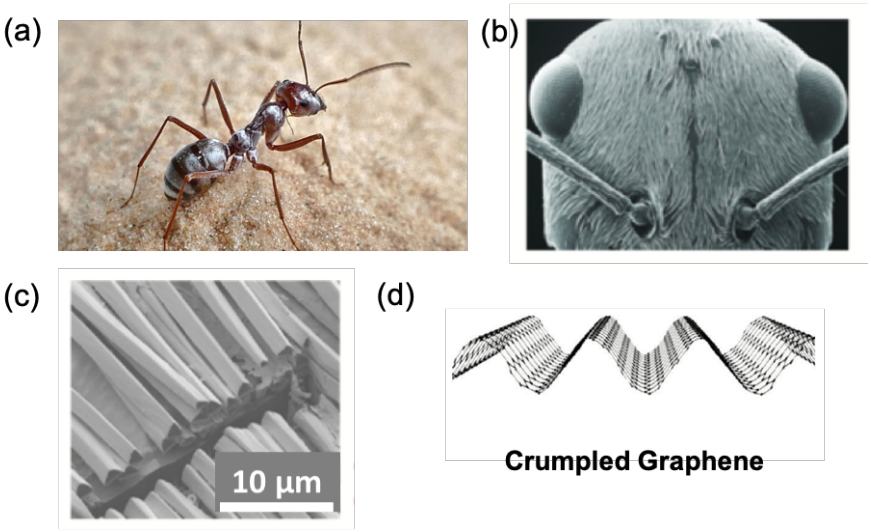

Figure 15. Deriving inspiration from the Saharan silver ant (22) for the development of crumpled graphene. (a) The Saharan silver ant in its natural habitat in the Sahara Desert. (b) The ant manages to remain cool in the extreme heat of the desert by making use of its mid-IR emissive and solar-spectrum reflective hair structures (22). (c) The hair structures are of a triangular cross-section and form the inspiration for the crumpled nature of the graphene surfaces under consideration here. (d) The structural schematic of the crumpled graphene surfaces.

The choice of graphene is motivated by its demonstrated use for spectral emissivity modulation (146–148), extremely high in-plane strength leading to large failure strain (149), and high fatigue resistance that allows extended lifetime of the proposed crumpled graphene structures.

Flat graphene offers a uniformly low emissivity of 0.025 throughout the electromagnetic spectrum (0.1-20 μm) (150). This emissivity profile has been modulated thus far by electrical control (146, 147) or nanotexturing (148). Crumpled graphene is used in this work to control the spectral emissivity leading to a reconfigurable radiative surface structure. This crumpled morphology can be coupled with stretchable platforms to attain dynamic emissivity modulation using simple mechanical straining. With the aid of this, I aim to develop solutions for dynamic thermoregulation with the crumpled graphene selective emitters.

3.2 Prediction of Optical and Thermal Properties

Rigorous coupled wave analysis (RCWA) is used to compute the surface emissivity of the crumpled graphene by a rigorous solution of the Maxwell's equations(65, 151). The input parameters include the optical constants such as the relative permittivity (and consequently the refractive index) for graphene(152, 153). The crumpled graphene structures are set up as periodic triangular features, composed of 30 layers of graphene steps approximating the sloped surfaces for crumpling. The output of the RCWA yields the reflectivity and transmissivity, and the emissivity is then computed as unity minus the sum of the reflectivity and transmissivity (70). The results are also compared with finite-difference time-domain (FDTD) computation results using commercially available Lumerical software. The graphene samples are set up as periodic triangular structures and the graphene layer is set up as an in-built material in the software. The outputs of transmissivity and reflectivity are then used to compute emissivity in similar fashion as above.

The results for RCWA and FDTD evaluation of crumpled graphene structures depict spectral variation in emissivity profiles for different values of crumpling pitch sizes (**Figure 16**). The appearance of distinct spectral peaks and dips in the surface emissivity is controlled primarily by the surface topography. For crumpled graphene samples with a pitch size of 140 nm, the emissivity spectrum shows high emissivity within the UV spectrum. Upon increasing the pitch size to 10 μm the results indicate high emissivity in the mid-IR wavelengths (**Figure 16a, 16b**). The distinct spectral emissivity profiles are a result of the interaction of the incident electromagnetic waves with the crumpled surface in distinct spectral regions (20, 65, 151), (**Figure 16**). The spectrally-distinct emissivity

profiles depend on the interference of incident electromagnetic waves over adjacent crumpled features. The multiple internal reflection incidents that happen at the graphene surface also induce spectral-selective lowering of transmissivity values, dependent on the surface topography and pitch size. The lowering of transmissivity leads to an increase in emissivity over the topography-controlled spectral regions.

The spectral emissivity results also need to be evaluated as a function of the solar zenith angle of incidence in order to optimize the selective emitter design based on the system and environmental conditions. The emissivity profile of the crumpled graphene as a function of solar angle of incidence (**Figure 16b**) indicates a largely angle-independent profile that shows a steep decay in spectral characteristics with large angles of incidence beyond 70˚. This is consequently helpful for the use of crumpled graphene structures for varying device orientations and environmental conditions.

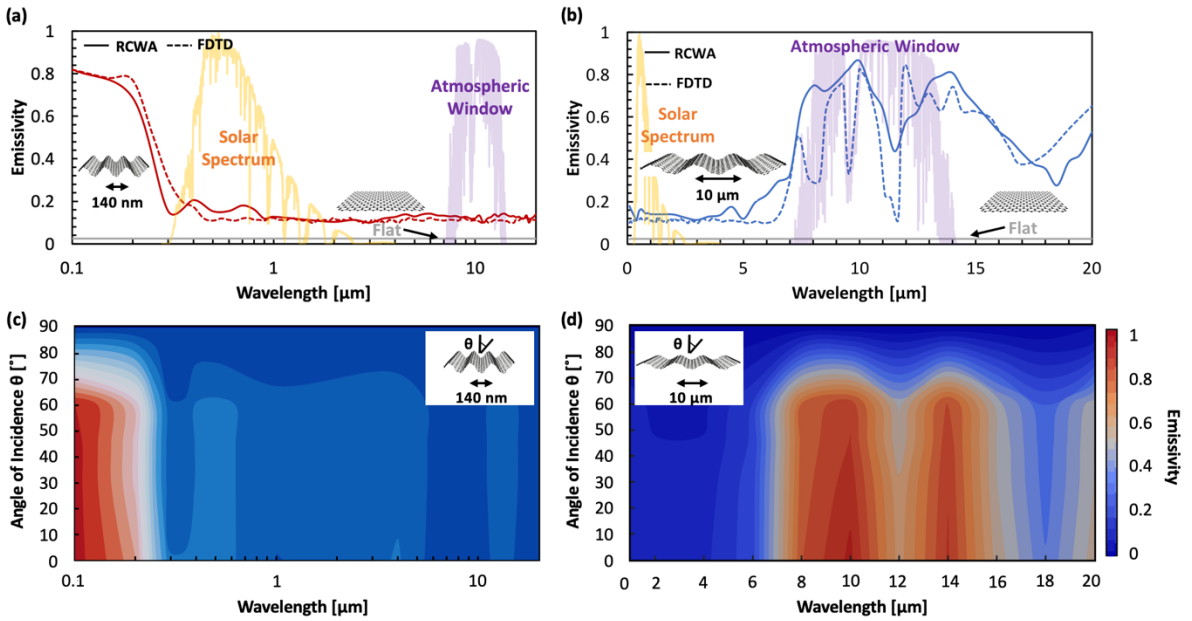

Figure 16. (a, b) Selective emitters based on crumpled graphene. The variations in crumpling pitch affect the radiative cooling (10 μm pitch) and heating (140 nm pitch) opportunities by using the incoming solar radiation and the atmospheric transmission window. Comparison of the computed emissivity values of the 290 nm pitch sample and the 10 μm pitch sample using RCWA and FDTD methods. Flat graphene shows a uniformly flat emissivity of 0.025. The profiles

are depicted with a focus in the solar (a) and IR (b) regions of the electromagnetic spectrum. (c, d) The solar angle of incidence dependent emissivity spectra for the crumpled graphene of pitch = 140 nm, and pitch = 10 μm, demonstrating the spectrally variant emissivity profiles for a wide range of angles. The emissivity profile remains fairly invariant for a majority of the angular range, displaying a sudden decay as the angles approach 70°. The largely angle-invariant emissivity profile potentially allows the use of the crumpled graphene structures for applications with varying angles of incidence in the ambient environment. Figure reproduced from (154).

While the RCWA computations are performed with the assumption of perfectly periodic samples, we analyzed the effects of deviations from the perfectly periodic structures. As observed from the SEM imaging, the samples of 140 nm periodicity show a standard deviation of ±15 nm (**Figure 17**), and samples of 10 μm periodicity show a standard deviation of ±1 μm (**Figure 18**). Taking into account the deviations in the periodicity, we observe minimal changes in the emissivity profiles for both samples (**Figure 17c**, **18c**). We attempt to introduce a non-uniform periodicity by modifying the unit cell for the computation, from periodicity of 140 nm to alternating 125 nm, 140 nm and 155 nm, and from 10 μm to 9 μm, 10 μm and 11 μm. The modified unit cells are constructed with the peak-to-peak distance between the first two crests being 125 nm (or 9 μm), the distance between the second and third crests being 140 nm (or 10 μm), and the third and fourth crests spaced 155 nm (or 11 μm) apart. For the perfectly periodic 140 nm periodicity samples, the computed emissivity peaks drop-off at a wavelength of 200 nm, similar to the modified unit cell (**Figure 19**). Similarly, for the perfectly periodic 10 μm samples and the modified unit cell, the emissivity values remain high between the wavelengths of 8-15 μm, with emissivity peaks at 8-11 μm and 13-15 μm (**Figure 19**). Based on our computational results, we expect little deviations due to non-perfect periodicity from experiments as well.

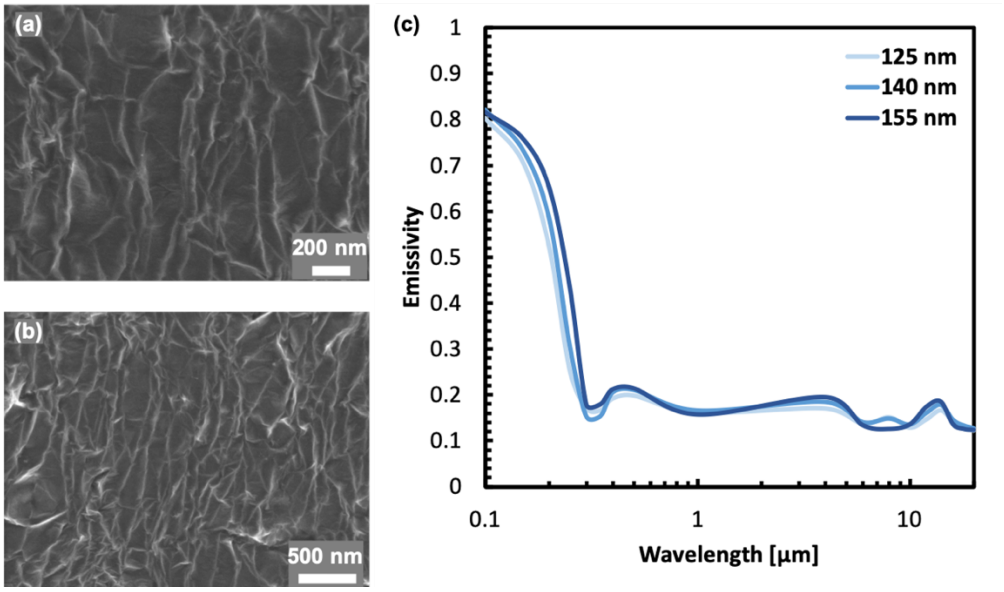

Figure 17. (a, b) SEM images of the crumpled graphene samples of 140 nm periodicity. The images depict periodicity values that have a mean of 140 nm and a standard deviation of ±15 nm. (c) Computational emissivity predictions for perfectly periodic crumpled graphene of 125 nm, 140 nm, and 155 nm periodicity, with peak emissivity drop-off at wavelengths between 200-300 nm wavelengths.

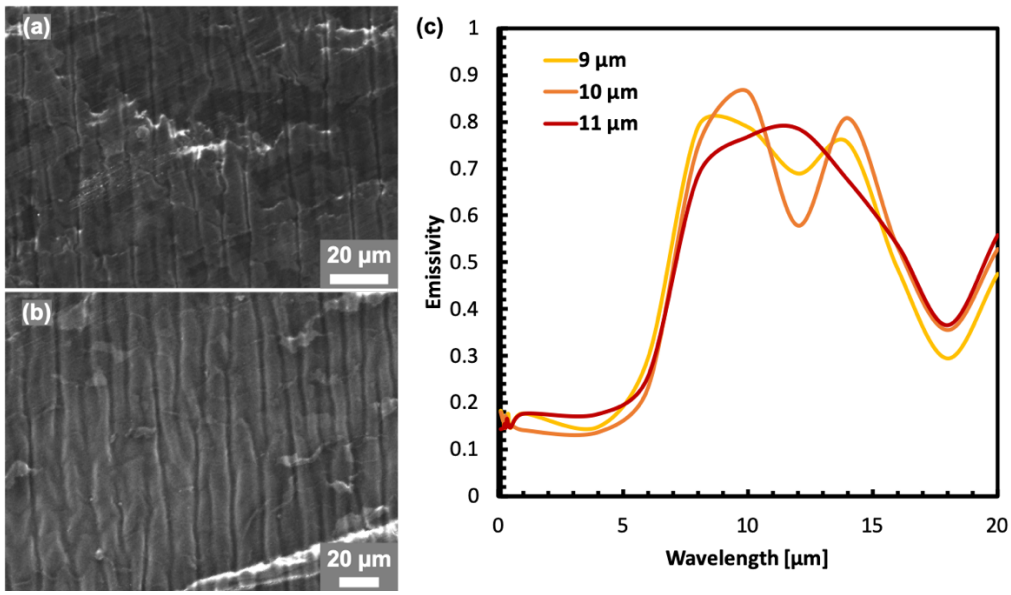

Figure 18. (a, b) SEM images of the crumpled graphene samples of 10 μm periodicity. The images depict periodicity values that have a mean of 10 μm and a standard deviation of ±1 μm. (c) Computational emissivity predictions for perfectly periodic crumpled graphene of 9 μm, 10 μm, and 11 μm periodicity, with emissivity peaks within the wavelength range of 8-15 μm. The 9 μm periodicity crumpled graphene exhibits slightly broader emissivity peaks at wavelengths of 8-15 μm. Similarly, the 10 μm periodicity crumpled graphene exhibits emissivity peaks at the wavelengths of 8-11 μm and 13-15 μm. The 11 μm periodicity crumpled graphene exhibits high emissivity throughout the wavelength range of 8-14 μm, with a broad peak centered at 11-12 μm wavelength.

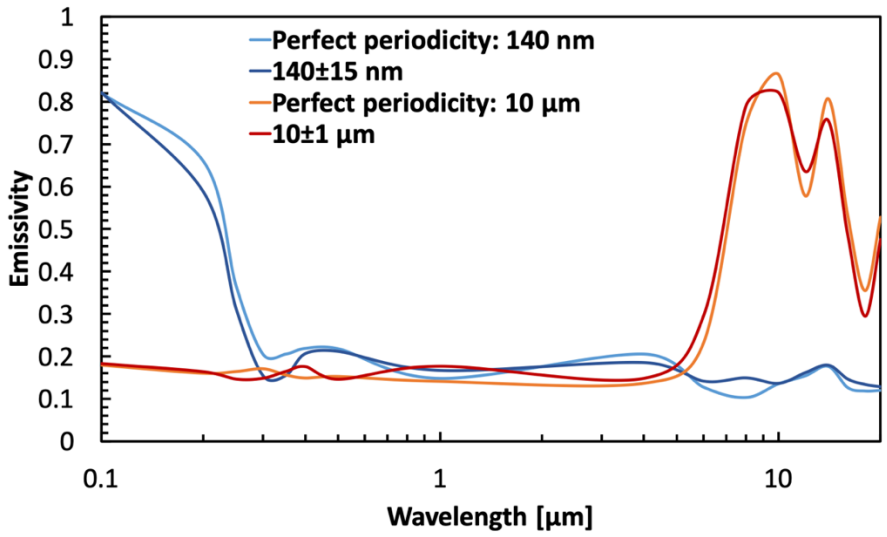

Figure 19. Relationship between spectral emissivity and deviations in crumple periodicity around the mean value for the 140 nm and 10 μm periodicity crumpled graphene, respectively. Computational results for perfect periodicity samples compared with samples of modified unit cell with mean periodicity 140±15 nm and 10±1 μm. The results for the modified unit cell show minimal changes from the perfect periodicity and illustrate the effects of structural deviations from perfect periodicity.

Based on the surface topographies of graphene and the selective surface emission with respect to the solar spectrum and the mid-IR ranges, the surface temperature can be dynamically controlled depending on the need. To evaluate the thermal performance of the proposed surface structure, I consider a thermal energy balance at the surface (**Figure 20a**) where the net power can be expressed by (20):

$$P_{net} = P_{rad} - P_{sun} - P_{atm} - P_{cond+conv} \qquad (1)$$

The term $P_{rad} = \int \cos\theta \, d\Omega \int_0^\infty I_{BB}(T,\lambda)\varepsilon(\lambda,\Omega)d\lambda$ is the power density radiated by the surface with the emissivity ε at the temperature T over the wavelength λ and over the solid angle $d\Omega$, and I_{BB} indicates the spectral radiance of a blackbody. The $P_{sun} = \int_0^\infty I_{AM1.5}(\lambda)\varepsilon(\lambda,\theta_{sun})\cos\theta_{sun}\, d\lambda$ is the power density absorbed by the surface facing the sun at angle θ_{sun}, with the solar illumination intensity $I_{AM1.5}$, which depends on the time of the day. The $I_{AM1.5}$ data are collected from the available literature (92). The expected range

of $I_{sun,\ AM1.5}$ in California is 0-510 Wm^{-2}, with the θ_{sun} being around 30˚ (155) and the I_{BB} being a function of the ambient temperature, which is assumed to range from 286 K to 300 K. The $P_{atm} = \int \cos\theta \, d\Omega \int_0^\infty I_{BB}(T_{amb}, \lambda)\varepsilon(\lambda, \Omega)\varepsilon_{atm}(\lambda, \Omega)d\lambda$ is the power density absorbed by the surface due to the surrounding atmosphere at T_{amb} with the transmission window given by ε_{atm}. The ε_{atm} value for a normal ambient condition in California is on average 0.3. Heat transfer by other environmental and device conditions is considered in the form of $P_{cond+conv} = h_{eff}(T - T_{amb})$ where h_{eff} is the effective heat transfer coefficient for convection and conduction phenomena. To predict the impact of crumpled graphene surfaces in normal ambient conditions, considerable heat transfer by convection and conduction (i.e. h_{eq} = 10 $Wm^{-2}K^{-1}$) are assumed with transient solar irradiance under clear sky (20).

The computation shows that the crumpled graphene of 10 μm pitch size can achieve a net cooling power of 77 Wm^{-2} at an ambient temperature of 300 K, and a surface temperature reduction 7 K below the ambient air (**Figure 20b, 20c**). The predicted tunable temperature range is shown to be 10 K in the normal ambient conditions (and up to 80 K in the theoretical limit of a completely isolated system). The crumpled graphene may lead to tunable sub-ambient radiative cooling (with the 10 μm pitch crumpled graphene) or above ambient heating (with the 140 nm pitch crumpled graphene).

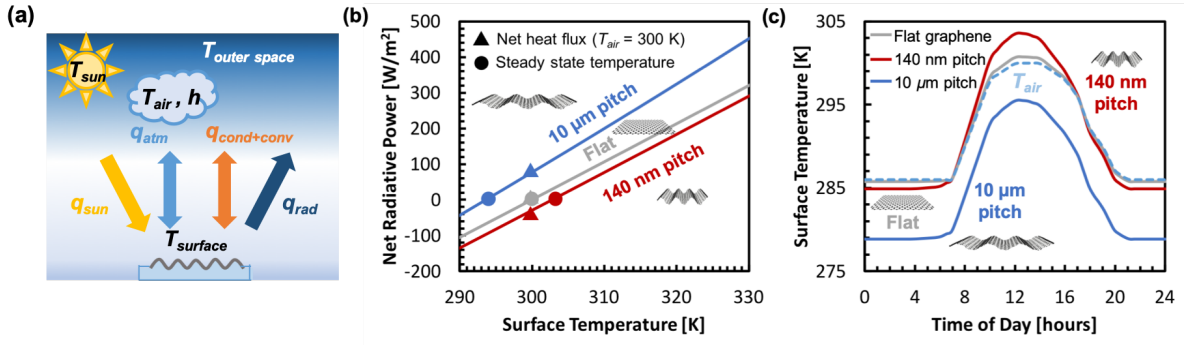

Figure 20. (a) Schematic depiction of the energy balance for the sample surface. The expressions for the heat flux estimations are presented in existing literature (20) and in the Equation 1. The sun heats the sample, with radiative exchange occurring between the sample and the atmosphere. The sample undergoes cooling with the outer space through the atmospheric window, and conductive and convective parasitic losses can be assumed to have an effective h_{eq} = 10 $Wm^{-2}K^{-1}$. (b) The temperatures of graphene surfaces are estimated using the emissivity spectra (Figure 1b) and considering the thermal energy balance in the ambient environment. The ambient temperature considered for this estimation is taken as 300 K. When the net power at the surface is zero, the steady-state temperature can be obtained. (c) The diurnal surface temperature profile shows the crumpled graphene of 10 μm pitch can provide sub-ambient cooling, with the estimated tunability of 10 K between the samples of 140 nm and 10 μm pitch sizes, which can be controlled by mechanical straining and with varying substrate conditions. Figure reproduced from (154).

3.3 Characterization of Optical Properties and Mechanical Tunability

The samples were fabricated and the surface corrugations of graphene were characterized in pitch sizes of 140 nm and 10 μm (156) (**Figure 21**). The crumpled graphene samples were fabricated on 3M VHB elastomer and poly(dimethylsiloxane) (PDMS) substrates respectively. The corrugation pitch sizes of the samples were verified using scanning electron microscopy (SEM) imaging, showing samples of pitch size of 10 μm (**Figure 20**). The samples were then evaluated using UV/Vis and Fourier transform infrared (FTIR) spectroscopy to obtain emissivity results from 200 nm to 15 μm wavelength.

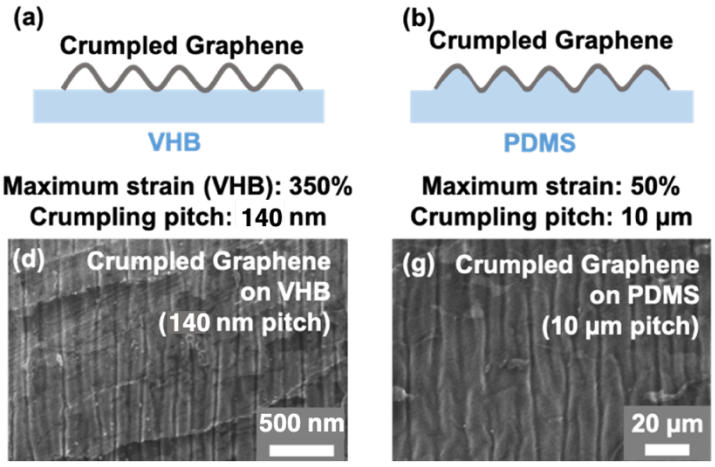

Figure 21. Crumpled graphene has been prepared by allowing a shrinkage of flat graphene on a pre-strained polymer substrate. (a, b) Side-view schematic of samples of increased crumpling pitch on VHB and PDMS substrates. (c, d) The crumpling dimension (140 nm, 10 μm) has been characterized by SEM. Figure reproduced from (154).

The spectroscopic analysis of the crumpled graphene samples in the UV/Vis spectral range were carried out using UV/Vis spectroscopy from 200 nm up to 2.5 μm wavelength (**Figure 22**). The data were measured as a differential with the substrate as the baseline, with the resultant crumpled graphene as the measured data. While the flat graphene

measurement shows a uniformly flat, low emissivity profile of 0.02-0.05, the crumpled graphene samples depict spectral variations in the emissivity profiles. The results depict the 140 nm pitch sample demonstrates an emissivity peak dropping off at 250-300 nm. The peak diminishes in value with increased pitch sizes (**Figure 22b**).

The dynamic tunability of the emissivity is enabled by the stretchable polymer substrates, by the mechanical straining of the samples. I measure the spectra before and after stretching the substrate (**Figures 22c, 22d**). Tensile straining of the samples shifts the drop-off in emissivity to lower wavelengths due to the flattening of the graphene crumples.

The results are also characterized for consistency over multiple cycles of stretching and relaxation. The **Figure 22d** depicts the spectral emissivity value taken at a wavelength of 0.25 μm over 30 cycles for a crumpled graphene sample with an original pitch of 140 nm. The cyclical straining leads to an on-off behavior in the emissivity at the 0.25 μm wavelength. The cyclical testing also displays no changes in emissivity related to fatigue and the samples may withstand further cycles of testing.

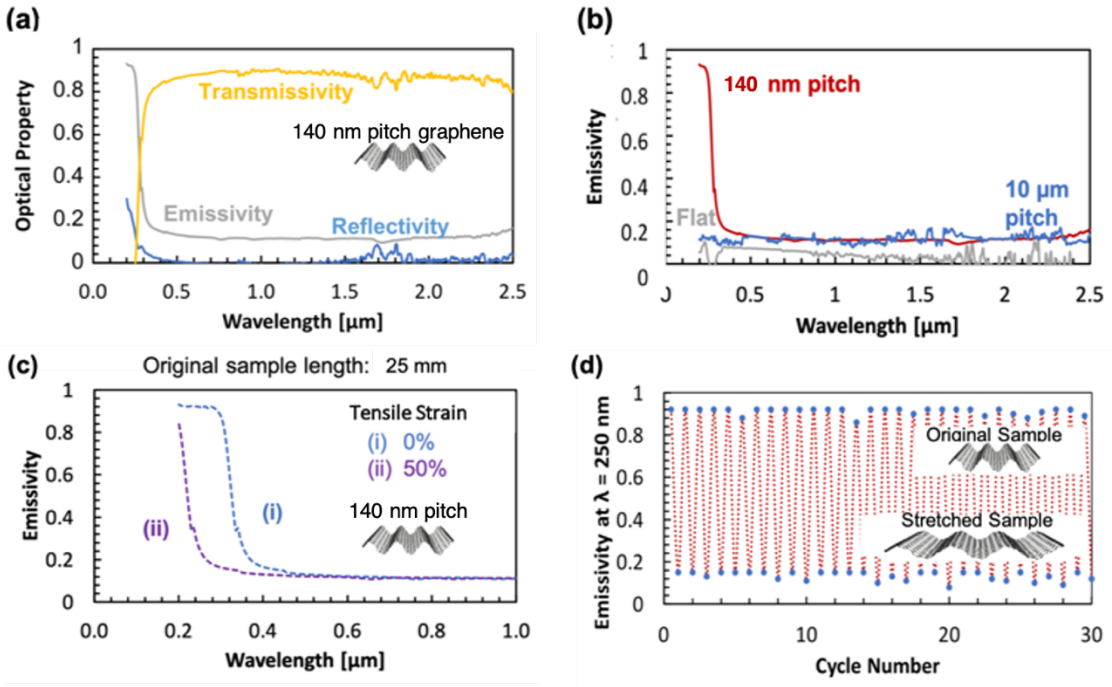

Figure 22. (a) Optical measurements of transmissivity, reflectivity, and emissivity of crumpled graphene of 140 nm pitch being measured by UV/Vis spectroscopy. (b) UV/Vis spectroscopy results for the emissivity of flat graphene, showing an emissivity value of 0.025, which agrees with the literature value, 140 nm pitch crumpled graphene showing an emissivity peak dropping off at 250-300 nm wavelength, and 10 μm pitch crumpled graphene depicting a uniformly flat emissivity profile. (c) By gently straining the 140 nm pitch crumpled graphene, the drop in the emissivity spectrum has blue-shifted, corresponding to a change in the pitch. (d) Emissivity measurements for 140 nm pitch crumpled graphene over 30 cycles of stretching and relaxation, at a wavelength of 0.25 μm. The change in emissivity value over multiple such cycles shows a retention of its characteristics. Figure reproduced from (154).

Similarly, the spectroscopic analysis of the crumpled graphene samples in the mid-IR spectral range were carried out using FTIR spectroscopy beyond 2.5 μm wavelength (**Figure 23**). The spectra were also taken as differential measurements to record purely the data for the crumpled graphene. In the mid-IR wavelengths, I notice prominent emissivity peaks in the 7.5-14 μm spectral region for the 10 μm pitch sample. The emissivity variations are a result of multiple diffraction and interference phenomena among adjacent crumple features and behave as evidenced by the simulation results shown in **Figure 16**. In order to verify the use of crumpled graphene for dynamic IR emissivity modulation, I further analyze the samples over cyclical straining as well. The FTIR results (**Figure 23c,**

23d) also demonstrate consistent emissivity tunability over multiple cycles of stretching and relaxation. The dip in spectral emissivity in the mid-IR regions was likely caused by the increase in pitch sizes due to the mechanical straining of the substrate.

I characterized the emissivity profiles for the samples when subjected to tensile strains beyond the original pre-strain of 20% (**Figure 23c**). The emissivity peak shifts from a wavelength of around 10 μm for a strain of 0%, to a wavelength of around 11 μm for a strain of 10%. When the strain is increased to 20%, the emissivity profile flattens out and has no discernable peak. With a further increase in strain to 25% and beyond, emissivity peaks appear in longer wavelengths, perhaps due to the transverse crumples or the formation of cracks (157). The samples showed negligible deterioration in spectral emissivity characteristics upon return to original state after being subjected to such increased strain, even over multiple cycles, demonstrating the reconfigurability of the crumpled graphene samples.

The cyclical data (**Figure 23d**) were also measured at a wavelength of 9.9 μm and display an on-off behavior in spectral emissivity. The results show the possibility of using the crumpled graphene structures for potential applications in passive dynamic thermoregulation solutions.

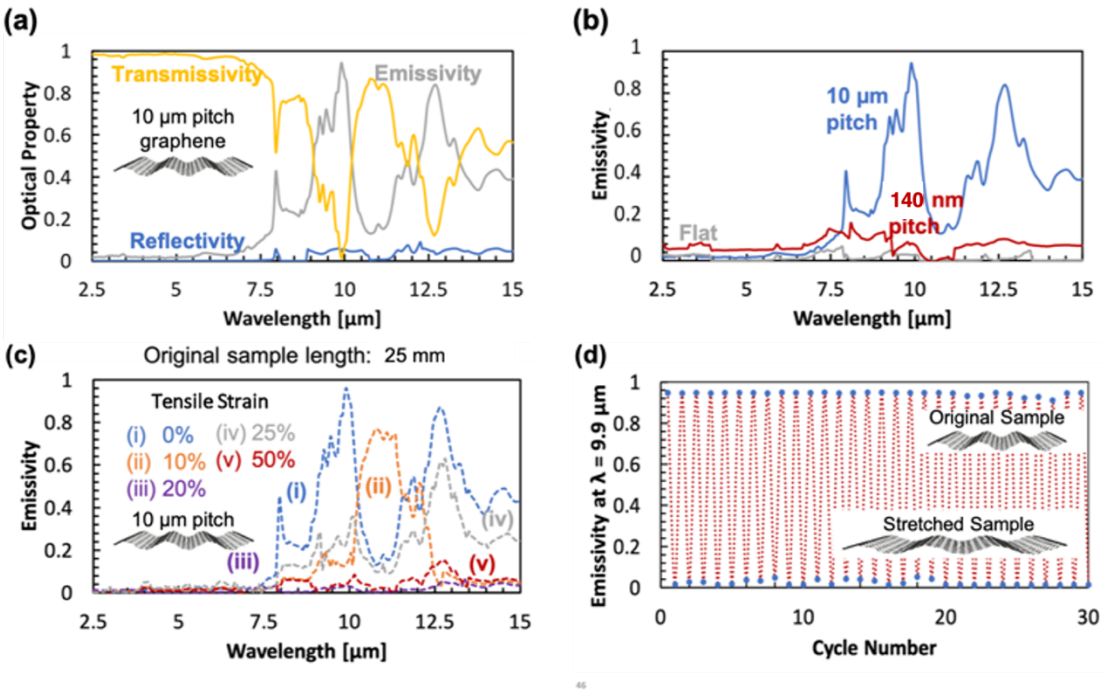

Figure 23. (a) Optical measurements of transmissivity, reflectivity, and emissivity of crumpled graphene of 10 μm pitch being measured in FTIR spectroscopy. (b) FTIR spectroscopy results for the emissivity of flat graphene, showing a uniformly low emissivity value, 290 nm pitch crumpled graphene showing low emissivity profile, although slight above flat graphene values, and 10 μm pitch crumpled graphene depicting emissivity peaks (and transmissivity dips) from 7.5 μm to 14 μm wavelength. (c) By straining the 10 μm pitch crumpled graphene sample, the corresponding change in crumpling pitch has lessened the peaks in emissivity with further peaks appearing with increased tensile strain due to transverse crumpling. (d) Emissivity measurements for 10 μm pitch crumpled graphene over 30 cycles of stretching and relaxation, at a wavelength of 9.9 μm, showing a retention of its characteristics over multiple cycles of stretching. Figure reproduced from (154).

To address the concern of potential damages to the 10 μm pitch crumpled graphene being strained beyond the original pre-strain value of 20%, we compare the emissivity profiles for the samples as they were subjected to 30 cycles of strain from 0% to 50%. For applied strain beyond the original pre-strain, the longitudinal crumples disappear, and the samples start to form transverse crumples due to Poisson's effect (where the application of tensile strain in one direction causes compressive strain in the transverse direction). However, the use of relatively soft fluorocarbon skin layer limits structural defects such as blisters and cracks (157). Here we show the emissivity profiles for the samples as

measured originally (before application of strain), after 1 cycle of straining to 50% and relaxation, and after 30 such cycles (**Figure 24**). The data shows negligible changes after 30 measurements, and the emissivity profiles of the samples return to their original state.

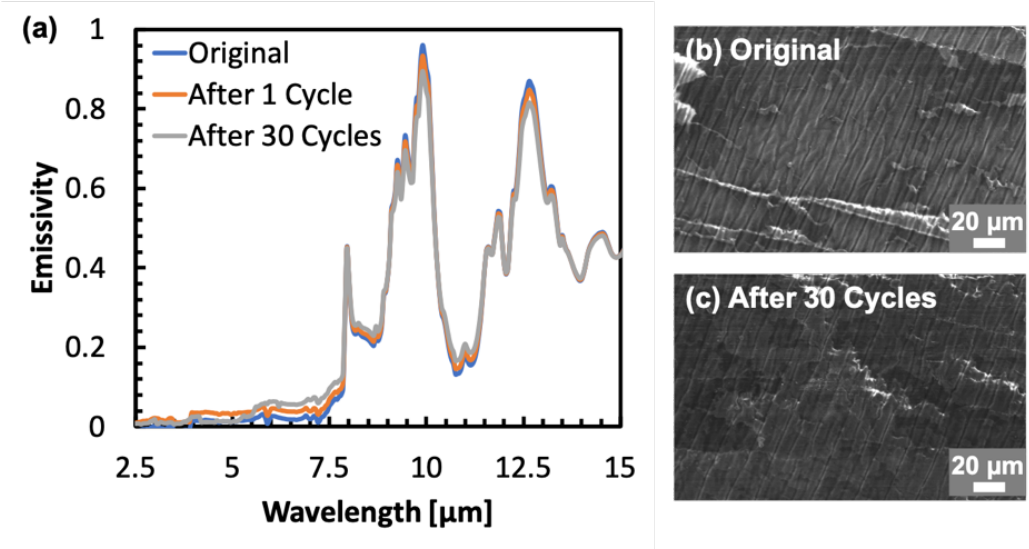

Figure 24. (a) Emissivity measurements for the 10 μm pitch crumpled graphene as measured originally (before application of strain), after one cycle of strain to 50% and relaxation, and after 30 cycles. The negligible changes in the emissivity profiles demonstrate the reconfigurable use of the crumpled graphene even upon experiencing strains exceeding the pre-strain condition. (b, c) SEM images of the 10 μm pitch samples originally (b), and after 30 cycles of straining to 50% and relaxation (c).

CHAPTER 4

4.1 Corrugated Metallic Structures for Wearable Thermal Management

Thermal management in the ambient environment demands spectral control of optical properties. While the incoming solar irradiation(136) heats up surface areas in the wavelength range of 200-2500 nm(158), the atmospheric transmission window(18) allows re-emission of the absorbed heat (i.e., cooling) from ambient surfaces to outer space in the mid-infrared (mid-IR) wavelength range of 7.5-14 μm(19, 20, 71, 72, 159). Because of the distinct spectral ranges allowed for heating and cooling, conventional approaches relying on a high- or low-emissivity material do not offer optimal solutions. One thus relies on engineered surfaces that can be designed to suit a specific application by varying the emissivity along specific regions of the electromagnetic spectrum. By using selective emitters to tailor the emissivity spectrum according to our needs, one can regulate thermal exchanges and optimally control the temperature without using electricity or bulky heat exchangers. The radiative thermal control by selective emitters is attractive for different systems such as solar absorbers(160), thermal imaging devices(161), and bolometers that measure emitted radiative heat from surfaces(162). Rapid developments in selective emitters based on passive nanophotonic structures(19, 20, 100) also show promise for personal- to system-level thermal control(163, 164).

The advancements in personal thermal management have mirrored the emergence and growth of the field of wearables. With the rise of personal health monitors(165), wearable radio-frequency antennas(166), and wearable electrochromic displays(167), there is an increased need for flexible and wearable thermal management solutions(168). This has so far been realized using selective emitters based on flexible substrates, examples

are blended textiles(169), nano-polyethylene fabrics(158, 170, 171) and nanowire-enhanced textiles(100). However, most state-of-the-art selective emitter systems(19, 71, 72, 104) lack dynamic control capabilities. The passive systems are unable to address diurnal or seasonal changes in thermal environments, and this lack of dynamic control affects the scope of their applications. The limitations of dynamic control of radiative and optical properties can be addressed in part by phase-change materials (PCMs)(143, 172). However, the use of PCMs heavily relies on the phase transition temperature, which might not lie in the favorable range of operation for the desired solution.

To overcome the dependence on transition temperature, I look for bio-inspired IR thermal solutions. A prominent example is the radiative cooling abilities of the Saharan silver ant(173). The remarkable cooling capability of the Saharan silver ants is attributed to their structural features, in which a dense array of hairs is characterized by triangular cross-sections. The hair structures on the ant's surface are reflective in the solar spectrum and highly emissive in the mid-IR range, which help them stay cool even in extremely hot temperature conditions of the desert(173). To enable dynamic control, I look for further bio-inspiration from the dynamic photonic materials in chameleons. The ability of chameleons to shift their appearance to communicate with others is a well-documented phenomenon(174). The color-shift is achieved by means of stretch-dependent variations in the distance between photonic nanocrystals and the accompanying spectral shift in reflectivity values. I now aim to integrate the thermal radiation management offered by the ants with the dynamic control offered by optical configuration in chameleons(174) to provide dynamic radiative thermal control.

I emulate the spectral variations in emissivity based on the unique morphology of the ant-hair structures with periodic triangular crests and troughs yielding a corrugated surface morphology. Here I use corrugated nickel to achieve effective modulation in surface emissivity. Nickel is ideal for thermal control on human bodies in the range between 305-314 K because of its relatively high absorptivity values (>0.3) in the solar spectrum (0.2-2.5 μm wavelengths), as compared to conventional metals for fabrication of selective emitters as gold(101), silver(175), or platinum(176) (which display a solar absorption coefficient <0.2)(177). The high solar spectrum emissivity combined with a low mid-IR emissivity (as opposed to highly emissive ceramics) makes nickel a good candidate for tunable emissivity control for solar absorption and personal thermal management solutions. While other metals as molybdenum possess comparably high solar absorptivity values (around 0.4)(178), nickel is chosen for its relative ease of fabrication and lower cost, and its use in existing solar absorber applications(179).

The dynamic modification of optical properties is achieved by emulating the stretch-dependent optical control in chameleons. A simple method analogous to morphology variations in chameleons is with the use of stretchable elastomer substrates, enabling a geometry change by applying a predetermined strain. For example, changes in strain enable the tuning of optical properties in deformation-controlled mechanochromic devices such as multilayer Bragg reflectors that change color with strain(180), switchable transparency windows(181, 182), and adaptive IR-reflecting solutions(25). Thus, I integrate the corrugated nickel with a stretchable elastomeric substrate (3M VHB 4910), in which the triangular corrugations offer easy reconfigurability for dynamic control of optical properties. The bio-inspired corrugated nickel thin film combines unique thermal

and optical properties of desert ants(173) and chameleons(174) (**Error! Reference s ource not found.**). The results presented in this work pave innovative ways of radiative thermal control and enable a reconfigurable thermal system that will utilize stretchable selective emitters.

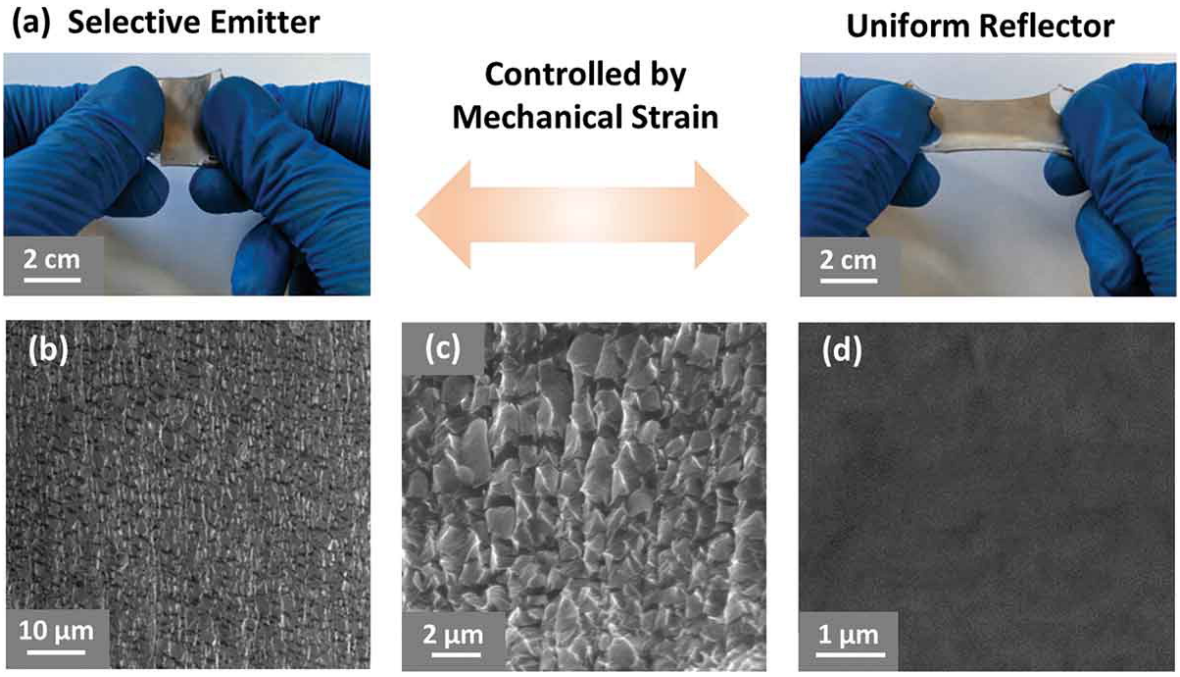

Figure 25. Bio-inspired stretchable selective emitter design. (a) Our work develops selective emitters based on corrugated nickel that resemble the morphology of desert ants and develops a dynamic system based on a stretchable polymer (3M VHB 4910) that resembles the color change mechanism of chameleons. The corrugated nickel films can selectively transform from non-emissive to emissive surfaces. (b) The SEM images show a 10 nm thick nickel layer on a stretchable substrate and sub-micron scale (0.6–0.8 μm) surface corrugation features spanning uniformly over a large area (> 1 cm^2). (c) Angled SEM image shows the corrugated nickel surface has a triangular corrugation profile. (d) The far-right image shows a flat nickel sample. Figure reproduced from (183).

4.2 Computational Prediction of Optical Properties

This work computes the spectral optical properties of corrugated nickel, including reflectivity, transmissivity, and consequently emissivity, using the rigorous couple wave analysis (RCWA)(65, 66) and finite-difference time-domain (FDTD)(184) methods (**Figure 26**). The RCWA method considers topographical variations and handles rigorous solutions of Maxwell's equations(20, 105). Direct results from RCWA yield scattering matrices in the forward and reverse directions, from which reflectivity (ρ) and transmissivity (τ) are computed. The emissivity is assumed identical to the absorptivity by Kirchhoff's law(17) and is computed from the reflectivity and transmissivity ($\alpha = 1-\rho-\tau$)(17). The FDTD method discretizes the samples and solves for space- and time-variant Maxwell's equation for each unit cell. RCWA is semi-analytical and treats the waves and fields as sets of gratings, hence making it very effective for corrugated structures. On the other hand, FDTD is superior in modeling curved surfaces and spherical shapes in full three-dimension. While FDTD is time-consuming, RCWA is more efficient towards optimizing the designs by variation of geometrical parameters.

In the work presented here, the corrugated nickel structures are modelled as a periodic array of triangles that are approximated using a staircase pattern composed of 30 steps, found to be a good approximation after a convergence analysis. This value not only offers sufficient accuracy but also makes the computational load manageable. The optical properties such as spectral permittivity and complex refractive index of the nickel layer(132, 185, 186) and the elastomer substrate(187–189) are considered as input parameters for the spectral computations. The geometrical variables that act as parameters controlling the topography of the corrugated nickel structures include the metallic layer

thickness and the corrugated pitch. The computational parameters, i.e. nickel layer thickness and corrugation pitch, are then optimized to provide maximum solar absorption. The thickness and pitch are inter-dependent parameters due to fabrication constraints. The layer thickness is taken to be 10 nm for the computation, on top of a substrate of 3M VHB 4910 elastomer, while the corrugated pitch is taken to be 700 nm between each successive topographic crest. The results depict substantial variations in the visible to near-IR emissivity values of corrugated and flat nickel (**Figure 26**). While the flat nickel maintains an emissivity of 0.3-0.4 within the wavelengths of 200 nm to 2 μm, the corrugated nickel attains an emissivity of 0.7 within the same spectral range. I attribute this increase in emissivity to interference among adjacent topographic ridges of corrugated nickel. The accompanying phenomena of multiple internal reflections significantly reduce the transmissivity through the sample, thereby increasing the emissivity.

The general emissivity trend is also captured by the Sparrow model(190), which predicts the overall surface emissivity for varying apex angles for surface corrugations or V-grooves. The Sparrow model shows a general increase in emissivity with corrugation of the surface (an average of 0.7 for corrugated, as opposed to an average of 0.36 for simple, flat surfaces). The increase in emissivity in the Sparrow model is due to the increase in internal reflection between adjacent grooves/corrugations(190). The increased internal reflection phenomena lead to an overall drop in transmissivity. With the reflectivity remaining fairly unaffected, the drop in transmissivity leads to an increase in emissivity. While this may provide a general idea of the trend of emissivity variations with increased or decreased corrugation angles, it fails to capture the more intricate topographical variations or spectral results compared to the RCWA or FDTD computations.

The angle-dependence of the emissivity of the sample (**Figure 26b**) is also studied to ensure optimal performance for a wide range of angles of incidence. The results demonstrate no noticeable change in the spectral emissivity of the corrugated nickel samples for angles of incidence up to 75˚, with no variation with respect to azimuth orientation. The negligible variation in emissivity behavior allows for the use of the corrugated nickel samples in varying geographic latitudes or daylight hours with minimal deviation from expected radiative performance.

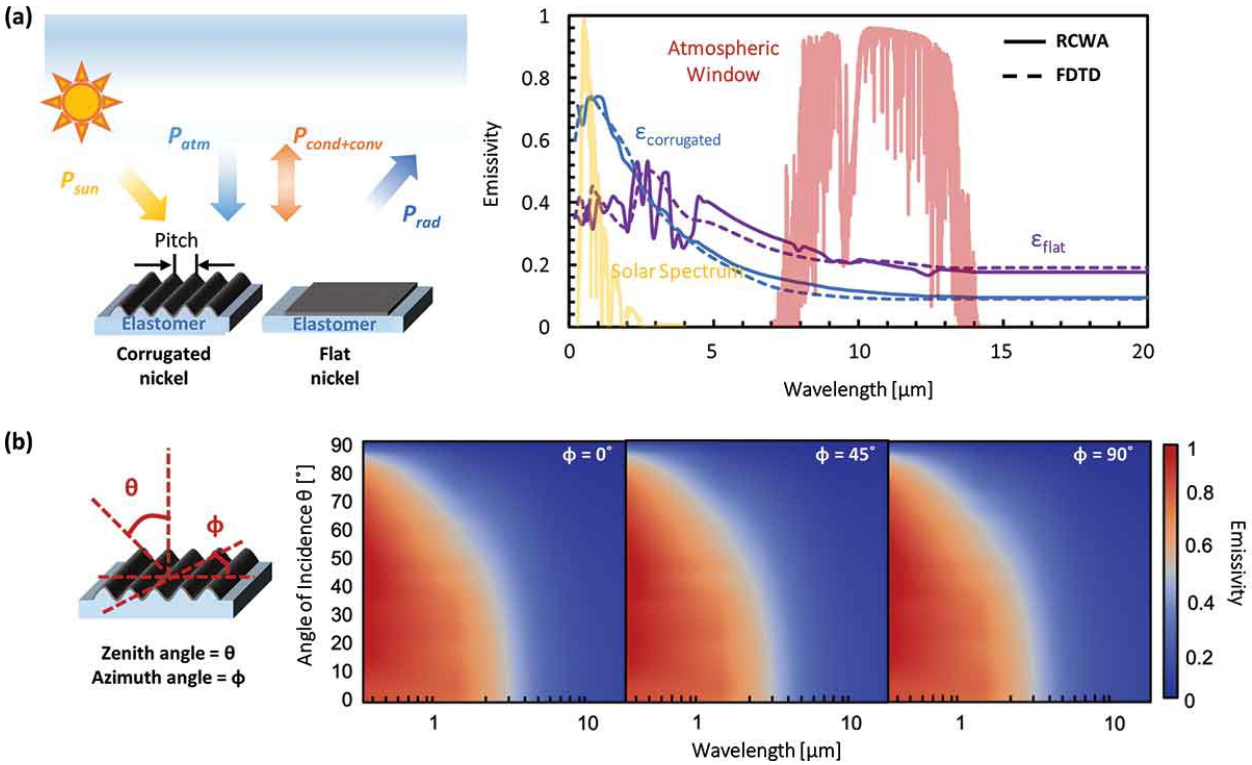

Figure 26. Computations by RCWA and FDTD methods. (a) The computational data for corrugated nickel of 700 nm pitch and flat nickel, both on elastomer substrate, are shown. The unit cell is replicated using periodic boundary conditions. Perfectly matched layer boundary conditions are applied at the bottom and top surfaces to avoid any undesired reflection of the plane wave at the physical boundaries. While the flat nickel shows an emissivity starting off at 0.4, reaching a value of 0.2 in the IR, the corrugated nickel displays a higher emissivity in the visible to near-IR, at 0.7, going down to 0.1 in the mid-IR. This elevated emissivity is attributed to multiple internal reflections of incident radiation, leading to a reduction in transmissivity and a consequent increase in emissivity. The left side schematic depicts the thermal interactions of the samples with the ambient environment. (b) The angle-dependent emissivity profile for the corrugated nickel samples, computed using the RCWA method. Varying the angle of incidence (zenith angle) from normal to 0° incidence, I notice a largely invariant emissivity profile, up to an angle of around 75°. The emissivity profile also remains predominantly

unchanged for various azimuth angles as well. The largely invariant emissivity profile allows for the application of the corrugated nickel samples in wide fields of use. Figure reproduced from (183).

4.3 Measurement of Optical Properties

The corrugated and flat nickel samples are fabricated by electron beam evaporation of 10 nm of nickel on the elastomer substrate. The fabricated corrugated nickel samples show a pitch of 600-800 nm for a pre-strain value centered around 250%, as has been verified by the SEM images. The triangular surface morphology has also been verified by angled SEM imaging (**Figure 25**), validating the use of triangular corrugations for computational modeling. Flat nickel samples were also prepared during the same deposition run on an un-stretched flat substrate, and both samples are characterized by reflectance spectroscopy in the wavelength range of 200 and 2500 nm.

The optical data for flat and corrugated nickel films show a significant difference in the visible spectrum (**Error! Reference source not found.**). As predicted by c omputational results (**Figure 26a**), the corrugated nickel film shows high emissivity values (>0.6) in the visible to near-IR ranges (200-2500 nm wavelengths) compared to the flat nickel film (with an emissivity <0.4). I performed measurements of corrugated nickel by stretching and releasing the elastomer and demonstrated reconfigurable emissivity variations, which can be utilized for dynamic thermal control. The corrugated nickel undergoes a strain of 200%, attaining an emissivity of 0.4. The emissivity profile of the stretched nickel is nearly the same as the emissivity profile offered by flat nickel (**Figure 27b**), thereby facilitating dynamic mechanically induced control of spectral emissivity.

With respect to the emissivity in the mid-IR region, the results deviate from what was ideally expected by computation. This is because of the presence of cracks perpendicular to the corrugated lines direction. Due to the large pre-strain applied before the evaporation pressure, when the sample is released the deformation in the transversal

direction exceeds the maximum plastic strain of nickel. Therefore, the nickel appears to be fragmented in SEM images. This is considered in the temperature computation by modeling, in RCWA, a model where the unit cell is not completely coated with nickel, resembling the actual structure.

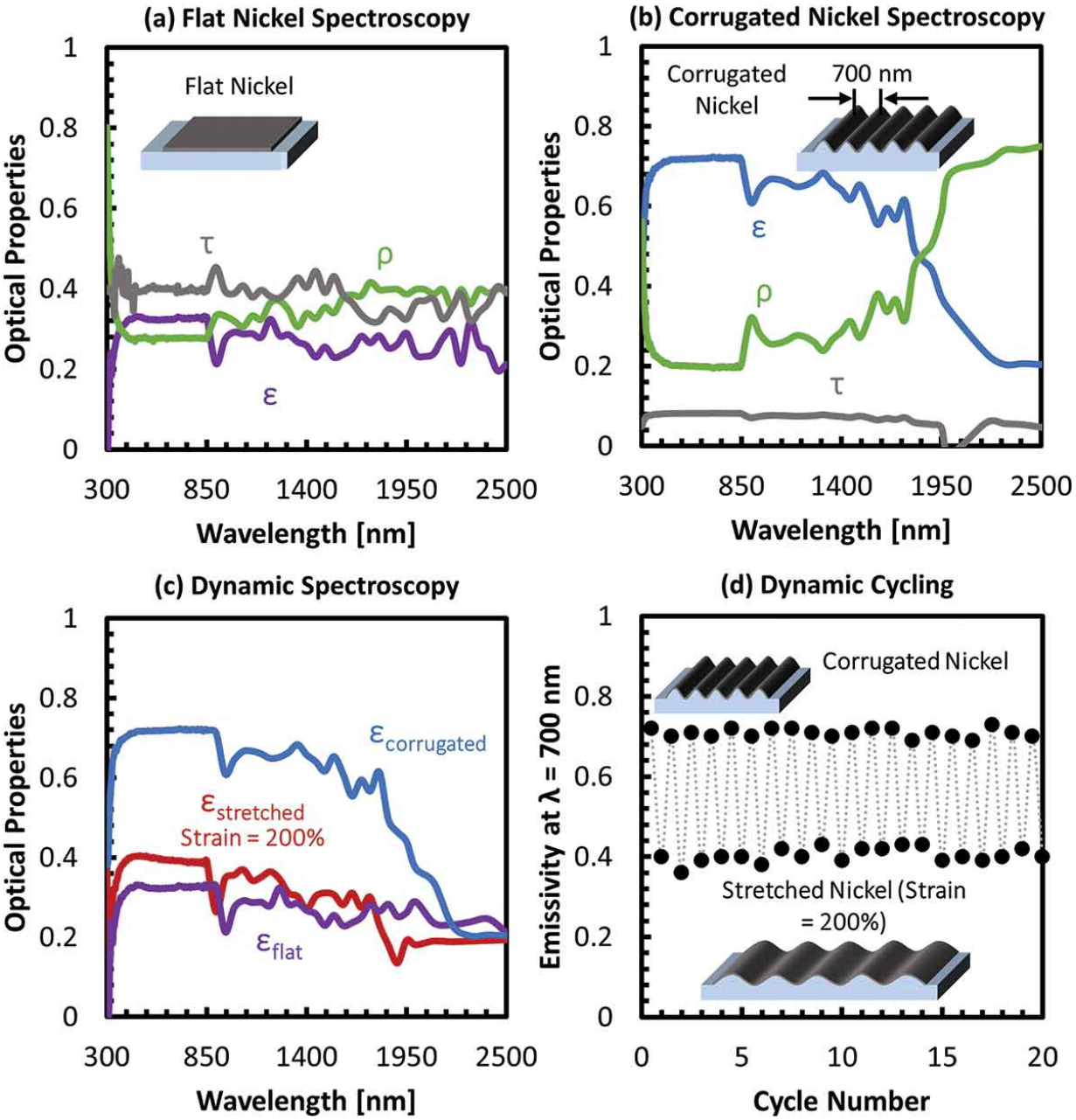

Figure 27. Reflectance spectroscopy data. The flat nickel sample includes a 10 nm thick film of nickel on a stretchable elastomer substrate, and the emissivity (ε) spectrum has been obtained by measuring the reflection (ρ) and transmission (τ) data. Compared to the flat film (a), the emissivity in the corrugated film (b) increases due to multiple scattering events and increased absorption. By varying the corrugation via mechanical straining, the emissivity can be dynamically

controlled. (c) The corrugated nickel system demonstrates the emissivity control from 0.7 to 0.4 in the visible spectrum, which leads to significant changes in solar absorption and radiative heating properties. The original sample length is 25 mm. (d) The data also show that the fully stretched corrugated sample restores the emissivity and optical properties of the flat samples and is repeatable up to 20 cycles of stretching and releasing the samples. At a wavelength of 700 nm the relaxed samples show an emissivity of 0.7, whereas the stretched samples show an emissivity of 0.4. Figure reproduced from (183).

4.4 Thermal Characterization and Proof-of-concept

The tunable emissivity modulated by mechanical control in corrugated nickel enables novel dynamic temperature control systems. To predict the impact of corrugated nickel surfaces in normal ambient conditions, considerable heat transfer by convection and conduction (i.e. h_c = 12 $Wm^{-2}K^{-1}$) are assumed with transient solar irradiance in the clear sky(20). I take the ambient conditions to be average values for California, with the ambient temperature varying between 286 K and 300 K through the day. The solar azimuth angle of incidence is also assumed to be the value taken at California, with the average angle being 30˚. The thermal performance of the selective emitters is then characterized by the thermal energy balance on their surface. The model predicts the corrugated nickel film to offer the steady-state temperature of 310-315 K in the case of normal ambient conditions with a gentle breeze (h_c = 12 $Wm^{-2}K^{-1}$) (**Figure 28a**). The surface temperature is higher than that of ambient air due to increased absorption of incident solar radiation. This is contrasted with flat nickel, which heats up to 3 K above the ambient air due to a lower solar absorptivity.

The predicted tunable temperature range is shown to be 10-12 K in the normal ambient conditions. During the day, around 12 noon, the temperature reaches 310-315 K for the relaxed corrugated nickel due to substantial solar irradiation, but the temperature of the flat and stretched corrugated nickel stays at 303-305 K. The corrugated samples are also made to undergo repeated cycles of stretching and relaxation with strains up to 200%. The results demonstrate a cyclical control of surface temperature varying from 312-314 K for the relaxed corrugated nickel to 304-306 K for the stretched state, depicting a simple mechanical actuation on the corrugated nickel leading to a substantial difference in

ambient thermal performance. The corrugated samples have been characterized by IR thermography on a temperature-controlled hot plate for the average emissivity measurement. Based on the emissivity data, the surface temperature has been characterized using thermography on a rooftop experimental stage that is exposed to the ambient environment (**Figure 28b**). The corrugated samples tested systematically using a mechanical holder demonstrate reconfigurable emission and thermal properties throughout the day in the ambient environment.

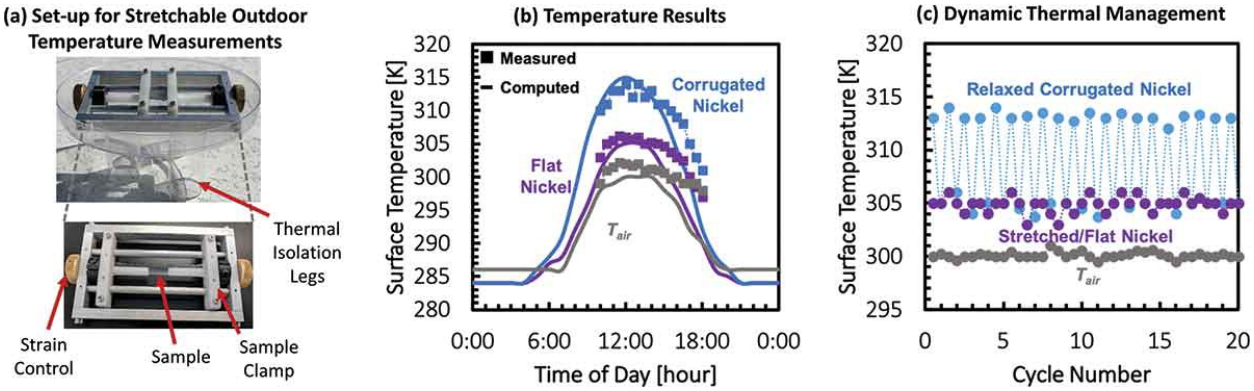

Figure 28. (a) Thermal characterization of stretchable selective emitters using outdoor temperature measurements. The samples were placed in a mechanical holder facilitating stretching, which was then placed resting on thermal isolation legs. (b) The temperature predictions and thermocouple measurement of corrugated and flat nickel samples under ambient conditions showing a temperature difference of 10–12 K between the flat and corrugated samples. (c) The temperature difference between the flat and corrugated designs promises dynamic controllability, as demonstrated by the cyclic measurements of stretching and relaxation. The measurements were taken at 12 noon and tested under 20 cycles of stretching to a strain of 200% and relaxation, indicating a reduction in heating upon stretching the sample, caused by morphology change in the corrugated nickel. Figure reproduced from (183).

Based on the corrugation effect, the nickel surface can provide a stable temperature throughout the day for potential applications in wearable electronics or comfort clothing. A preliminary demonstration of the use of corrugated nickel samples in personal applications has been done through measuring the temperature change when stretching the corrugated nickel samples on top of the human body. The corrugated nickel samples were strapped to

the chest and to the wrist to evaluate the strain/flexing-controlled temperature and heat flux changes. While the on-chest samples required manual straining and fastening, the on-wrist samples were strained by the flexion and extension movement of the human wrist. The samples were then characterized by IR thermography under identical measuring conditions on the same day. The skin temperatures on the chest and wrist were measured using thermocouples to avoid uncertainty in the skin emissivity input parameter for IR thermography. While the body temperature depends on individual conditions, i.e. gender, body mass index, and ethnical origin(191), there are clear differences between different skin zones(192). In our study, the chest depicted a temperature of around 309 K, while the wrists depicted temperatures of around 305 K. The chest can be assumed to be thermally analogous to the forehead, due to the similar temperature values on both locations(191). The temperature in the relaxed and stretched states of the corrugated nickel samples on the chest were measured to be 309.7 K and 308.8 K, while on the wrist, they were measured to be 307 K and 305.1 K (**Figure 29**). While ideally the samples are assumed to be in perfect contact with the human body, real life measurements might not allow it, resulting in slight variations between measured and computed values of temperature.

The recorded surface temperatures can then be translated into estimates for the conduction heat flux into/drawn away from the human skin (P_{cond}''). The P_{cond}'' values are then determined by a one-dimensional approximation for the heat conduction equation, giving $P_{cond}'' = \frac{\Delta T}{R_{th}''}$, where ΔT is the difference in temperature between the skin and the surface of the corrugated nickel, and the thermal conductive resistance is given by $R_{th}'' = \frac{L}{k}$. Here, L is the thickness of the sample (1 mm for relaxed state and 0.45 mm for stretched

state), with k being the thermal conductivity of the sample substrate, taken to be 0.16 $Wm^{-1}K^{-1}$ (189). For measurements on the chest, the ΔT for the samples is 0.7 K while relaxed and -0.2 K while stretched, giving P_{cond}'' values of 112 Wm^{-2} into the skin while relaxed and -71.1 Wm^{-2} out of the skin while stretched. For measurements on the wrist, the ΔT for the samples is 2.0 K while relaxed and 0.1 K while stretched, giving P_{cond}'' values of 320 Wm^{-2} into the skin while relaxed and 35.6 Wm^{-2} into the skin while stretched.

The values of heat flux in or out of the human body depend on the skin temperature, which varies from one location to another. When the sample is located on top of the human chest, the calculations(19, 20) at 12 noon with a convective coefficient of 12 $Wm^{-2}K^{-1}$ and an incoming solar radiation of 529 Wm^{-2} show a net heat flux ($P_{net}'' = P_{sun}'' - P_{rad}'' + P_{atm}'' + P_{conv}''$) of -62.5 Wm^{-2} of heat drawn from the skin while stretched (with P_{sun}'' = 198.7 Wm^{-2}, P_{rad}'' = 399.4 Wm^{-2}, P_{atm}'' = 244.1 Wm^{-2}, P_{conv}'' = -105.9 Wm^{-2}), and 79.1 Wm^{-2} of heat going into the skin while relaxed (with P_{sun}'' = 379.5 Wm^{-2}, P_{rad}'' = 456.0 Wm^{-2}, P_{atm}'' = 269.6 Wm^{-2}, P_{conv}'' = -113.9 Wm^{-2}). The calculations agree well with the values obtained with IR camera measurements on the chest (**Figure 29**). The measurements were done with the corrugated nickel sample fastened to the chest and manually stretched in steps to a maximum strain of 150%. The on-chest measurements depict net heat flux to the human body varying from net positive (into the body) to net negative (out of the body). However, the level of strains that enable these changes cannot be achieved by the natural flexing of the human chest. The flexion/extension-enabled strain variations can be achieved by fastening the corrugated nickel samples to the wrist.

For applications on the wrist, where the skin temperature is 305 K, the net heat flux is positive into the skin for both stretched and relaxed (varying from near-zero to largely

positive). Repeating the calculation at 12 noon with a convective coefficient of 12 $Wm^{-2}K^{-1}$, the heat fluxes are estimated as P_{net}'' of 1.43 Wm^{-2} of heat going into the skin while stretched (with P_{sun}'' = 198.7 Wm^{-2}, P_{rad}'' = 381.30 Wm^{-2}, P_{atm}'' = 244.1 Wm^{-2}, P_{conv}'' = -60.1 Wm^{-2}) and 142.9 Wm^{-2} of heat going into the skin while relaxed (with P_{sun}'' = 379.48 Wm^{-2}, P_{rad}'' = 435.4 Wm^{-2}, P_{atm}'' = 269.6 Wm^{-2}, P_{conv}'' = -70.7 Wm^{-2}). This human actuation-induced control over emissivity and consequently temperature of the samples acts as a proof-of-concept for applications of the corrugated nickel structures in the fields of personal thermal management and wearable electronics (**Figure 29**).

I observe that for a low skin temperature of 305 K on the wrist, the device only provides heat to the body (P_{net}'' = 142.9 Wm^{-2} when relaxed and P_{net}'' = 1.4 Wm^{-2} when stretched), avoiding overcooling of the human body. However, for a chest skin temperature of 309 K (close to the mean temperature of the human body), the heat fluxes can be positive, i.e. heat into the skin, or negative, i.e. heat drawn from the skin (with P_{net}'' = 79.1 Wm^{-2} when relaxed and P_{net}'' = -62.5 Wm^{-2} when stretched).

The mismatch between the measured and modelled heat flux especially with respect to the fully relaxed state for the samples on the chest and the wrist can be explained due to the possibility of imperfect contact between the skin and the samples. Assuming an estimated contact resistance of 6.25 × 10-3 Km^2W^{-1} from literature(193), I notice a reduction in the heat flux as measured. For the chest, the heat flux for the fully relaxed state with contact resistance is estimated to be 56 Wm^{-2} into the skin, while for the wrist under similar conditions it is estimated to be 160 Wm^{-2}.

The use of the corrugated nickel samples on the human skin, however, would impede the natural evapotranspiration cooling provided by sweating. I thus compare the

heat loss due to potential evapotranspiration with the neat heat loss to the stretched corrugated nickel samples. The evaporative heat loss from the skin is given as $P_{evap} = S \cdot h_v$, with S being the sweat rate and h_v being the latent heat of evaporation (2.427×10^6 Jkg^{-1})(194). The sweat rate for the human body is estimated to be $1.667 \times 10^{-5} - 8.333 \times 10^{-5}$ $kgs^{-1}m^{-2}$ (for a skin temperature varying between 308-314 K)(194). This results in an evaporative heat loss of 40.44-202.22 Wm^{-2} for the human skin(194, 195), compared with a net heat loss of 62 Wm^{-2} provided by the stretched corrugated nickel samples on the chest. The corrugated nickel samples provide dynamic tunable thermal and optical control by simple mechanical strain, as opposed to the lack of direct control over evapotranspiration based on personal preference.

The device durability could be affected by temperature, humidity, and sweat on the human body where it's placed. To analyze the life of the elastomer substrate, I compute the number of cycles the elastomer would be able to resist before breaking. The acrylic substrate used in this work has shown excellent fatigue life in previous research, where stretchable electrodes based on wrinkled elastomers were fabricated and tested after 100,000 cycles, showing little effect in the performance of the device(196). Evaluating the fatigue response for the samples by using the data obtained in past studies, where the crack growth rate was measured during a cyclic loading-unloading test(197), I estimate that the samples can withstand up to 10^7 cycles before breaking, even assuming the pre-existence of a 0.18 mm crack present in the elastomeric substrate, with the value dramatically increasing for smaller initial cracks. This estimation is performed considering the substrate undergoes a strain of 200%.

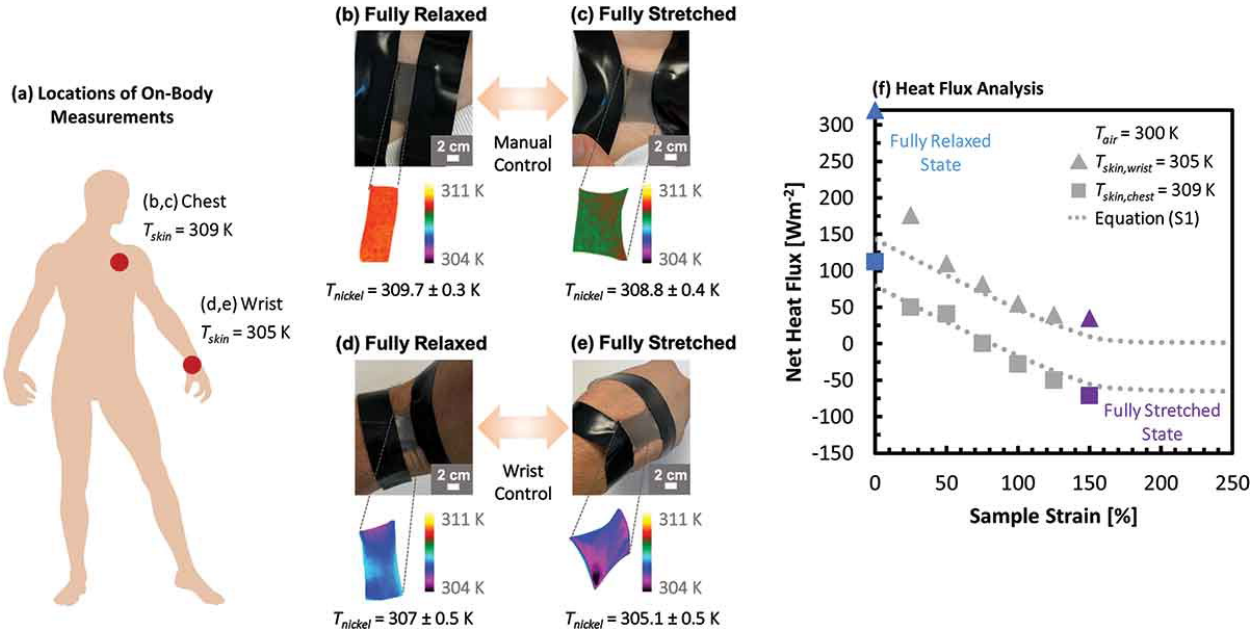

Figure 29. (a) Demonstration of the corrugated nickel samples as a wearable system on different locations of the human body. I perform temperature and heat flux measurements by placing the sample on the chest (b, c) (where the skin temperature is 309 K) and wrist (d, e) (where the skin temperature is 305 K). The chest is assumed equivalent to the forehead due to the similar skin temperature on both locations. The IR imaging (insets) depicts a measurement of temperatures for the nickel samples. On the chest, the relaxed nickel (b) shows a temperature of 309.7 ± 0.3 K, and the stretched nickel (c) shows a surface temperature of 308.8 ± 0.4 K. On the wrist, the relaxed nickel (d) shows a temperature of 307.0 ± 0.5 K, and the stretched nickel (e) shows a surface temperature of 305.1 ± 0.5 K. (f) The net heat flux into or out of the human body at 309 K (chest) and 305 K (wrist) in ideal contact with the corrugated nickel samples. The theoretical prediction for the heat flux based on Equation S1 is shown by a dotted line. While the on-chest samples (squares) depict heating to cooling from 79.2 Wm^{-2} to −62.5 Wm^{-2}, the on-wrist samples (triangles) only depict heating from 142.9 Wm^{-2} to 1.4 Wm^{-2}. Figure reproduced from (183).

CHAPTER 5

Discussion and Conclusions

The mid-IR emissivity values for the butterfly wing microstructures range from high to low, roughly corresponding to the habitat temperature for the butterflies ranging from warm to cool. The results illustrate the role played by periodic microstructures on butterfly wings' mid-IR optical properties, and their impact on butterfly thermoregulation. Further evaluation of the correlation of habitat temperature with solar and mid-IR optical properties of butterfly wings would likely advance our understanding of how butterflies adapt to varying habitat environments. For instance, the current study depicts warmer climate butterflies with increased mid-IR emissivity values. Meanwhile, existing literature indicates increased flight duration for butterflies from warmer climates (90). The link between the warmer climates, increased mid-IR emissivity and increased flight duration could possibly be explained due to the decreased time to attain steady-state temperatures for increased mid-IR emissivity. However, the hypothesis would require further analysis to yield conclusive results.

Apart from butterflies, studies on the structural thermoregulation of other geographically and climatically diverse animals could lead to better insights as to the role of IR optical properties in the ability of organisms to adapt to their surroundings. For instance, insects such as ants are wide-spread and found in extreme climates. Analysis of the mid-IR optical properties in such ants could enhance our understanding of the role of structural thermoregulation in their survival and dispersal.

The natural variations in the structural parameters of the microstructures could also act as a basis for the development of bio-inspired designs for broadband thermal

control. Unlike the narrow-band requirements of photonic systems such as multilayer reflectors, thermal systems favor broadband properties that do not require perfectly periodic structures, making the butterfly wing microstructures potential candidates for the design of thermal control systems. Our results thus present an improved knowledge of surface microstructures in nature and their relationship to thermoregulation.

Drawing inspiration from Saharan silver ants, I fabricate the crumpled graphene samples on stretchable substrates. Our computations using rigorous coupled-wave analysis (RCWA) and finite-difference time-domain (FDTD) methods depict mid-IR emissivity control from 7.5-14 μm wavelengths by the 10 μm pitch crumpled graphene. Significant emissivity changes arise from interference induced by the periodic topography and selective transmissivity reductions for the graphene.

Our measurements using UV/visible and Fourier transform infrared (FTIR) spectroscopy validate the emissivity computations and demonstrate dynamic modulation of spectral emissivity. Controlled changes in the tensile strain applied on the 10 μm pitch crumpled graphene show reversible emissivity peak changes at 9.9 μm wavelength. Based on cyclical tunability of emissivity, I thus demonstrate the unique potential of crumpled graphene as a reconfigurable optical and thermal management platform.

The dynamic control of spectral emissivity in the crumpled graphene is predicted to lead to tunability of surface temperature in the samples. I analyze the behavior of the 10 μm pitch crumpled graphene in ambient conditions with an air temperature varying from 286-300 K and moderate wind with a convective coefficient of 10 $Wm^{-2}K^{-1}$. The results predict the 10 μm pitch samples having a cooling power of 77 Wm^{-2}, and consequently attaining surface temperature of 7 K below ambient. The findings thus deepen our

understanding of topography-driven radiative control in 2D materials and enable developments of dynamic optical and thermal management systems.

The corrugated nickel-based selective emitters presented here follow simple fabrication techniques based on the integration of metal deposition on a pre-strained stretchable elastomer substrate. The resultant structures offer emissivity control over the solar spectrum with values ranging from 0.3 to 0.7 based on varying levels of stretching and releasing.

Considering the natural variability of ambient climatic conditions, where thermal boundary conditions can have a big impact on the heating and cooling rates of the human body, the controlled control of radiative and thermal properties by a simple mechanical actuation is a significant improvement to the state-of-the-art. The simple stretching and relaxation pose a considerable advantage over other methods of emissivity control, such as phase change materials with their transition temperature-limited applications. Phase change materials are inherently reliant on their fixed transition temperature which controls their change in optical properties from metallic to insulator or vice versa. Overcoming this material-imposed shortcoming enables us to attain control over optical and thermal properties irrespective of the operating temperature.

The dynamic control of optical properties can be applied to systems and surfaces where a quickly tunable spectral and thermal response is desired. The 10-12 K control in temperature allows the device to perform within a wide range of solar and ambient conditions, while maintaining a controlled surface temperature. The structure-induced thermal control offers solutions suited for various applications ranging from comfort clothing to smart windows and wearable electronic devices.

The samples presented here have been tested in Irvine, California during the summer, where the average solar irradiance is 1947 $kWhm^{-2}$ per year, and the ambient air temperature varies from 286 K to 300 K. These ambient values are similar to a vast majority of highly populated regions in the world, as in South America, Africa, India and Australia. In these regions, our design is rendered feasible to be applied to human body thermal management. The corrugated nickel sample is tested to be wearable on the chest and wrist, where it maintains its functionality, acting as a proof-of-concept for its use in personal thermal management systems. In the case of use on the chest, the product can deliver a positive or negative net heat flux to the skin below, making both heating or cooling possible in the typical range of human body temperature (308–314 K), by means of stretching or releasing the substrate. When a hypothermic state is reached (308 K), the structure provides net heating to the skin, similarly providing net cooling to the skin in the opposite case, when the body is in a hyperpyrexia condition at 314 K.

In different ambient environmental conditions, especially colder parts of the world, such as Canada, northern Europe or Russia, the corrugated nickel performs less than ideally as a personal thermal regulator. However, it can have other equally interesting applications such as thermoregulation of devices around the ambient air temperature. Further evaluation of the corrugated metallic selective emitters for radiative cooling would increase the applicability of the samples towards varying geographic, climatic, and system-level demands.

REFERENCES

1. R. C. Best, Thermoregulation in resting and active polar bears. *J. Comp. Physiol.* ■ *B* **146**, 63–73 (1982).

2. J. H. He, Q. L. Wang, J. Sun, Can polar bear hairs absorb environmental energy? *Therm. Sci.* **15**, 911–913 (2011).

3. J. A. Preciado, *et al.*, Radiative properties of polar bear hair in *ASME International Mechanical Engineering Congress and Exposition, Proceedings*, (2002), pp. 57–58.

4. A. Herman, C. Vandenbem, O. Deparis, P. Simonis, J. P. Vigneron, Nanoarchitecture in the black wings of Troides magellanus : a natural case of absorption enhancement in photonic materials. *Nanophotonic Mater. VIII* **8094**, 80940H (2011).

5. S. Berthier, Thermoregulation and spectral selectivity of the tropical butterfly Prepona meander: A remarkable example of temperature auto-regulation. *Appl. Phys. A Mater. Sci. Process.* **80**, 1397–1400 (2005).

6. G. M. O. Maloiy, J. M. Z. Kamau, A. Shkolnik, M. Meir, R. Arieli, Thermoregulation and metabolism in a small desert carnivore: the Fennec fox (Fennecus zerda) (Mammalia). *J. Zool.* **198**, 279–291 (1982).

7. H. Korhonen, M. Harri, J. Asikainen, Thermoregulation of polecat and raccoon dog: A comparative study with stoat, mink and blue fox. *Comp. Biochem. Physiol. -- Part A Physiol.* **74**, 225–230 (1983).

8. J. J. Klir, J. E. Heath, An Infrared Thermographic Study of Surface Temperature in Relation to External Thermal Stress in Three Species of Foxes: The Red Fox (Vulpes

vulpes), Arctic Fox (Alopex lagopus), and Kit Fox (Vulpes macrotis) . *Physiol. Zool.* **65**, 1011–1021 (1992).

9. L. T. Wasserthal, The role of butterfly wings in regulation of body temperature. *J. Insect Physiol.* **21**, 1921–1930 (1975).

10. J. G. Kingsolver, Thermoregulation and flight in Colias butterflies: elevational patterns and mechanistic limitations. *Ecology* **64**, 534–545 (1983).

11. D. Stuart-Fox, *et al.*, Climate is a strong predictor of near-infrared reflectance but a poor predictor of colour in butterflies. *Prcoeedings R. Soc. B* **286** (2019).

12. S. G. Bosi, J. Hayes, M. C. J. Large, L. Poladian, Color, iridescence, and thermoregulation in Lepidoptera. *Appl. Opt.* **47**, 5235–5241 (2008).

13. J. A. Clark, K. Cena, N. J. Mills, Radiative Temperatures of Butterfly Wings. *Zeitschrift für Angew. Entomol.* **73**, 327–332 (1973).

14. S. Kinoshita, S. Yoshioka, Y. Fujii, N. Okamoto, Photophysics of structural color in the Morpho butterflies. *Forma-Tokyo-* **17**, 103–121 (2002).

15. F. P. Incropera, D. P. DeWitt, T. L. Bergman, A. S. Lavine, *Fundamentals of Heat and Mass Transfer* (John Wiley & Sons, 2006).

16. D. P. DeWitt, F. P. Incropera, "Physics of Thermal Radiation" in *Theory and Practice of Radiation Thermometry*, (1988), pp. 19–89.

17. J. R. Howell, M. P. Menguc, R. Siegel, *Thermal Radiation Heat Transfer* (CRC Press, 2016).

18. S. D. Lord, “A New Software Tool for Computing Earth’s Atmospheric Transmission of Near- and Far-Infrared Radiation” (1992) https:/doi.org/1992nstc.rept.....L.

19. A. P. Raman, M. A. Anoma, L. Zhu, E. Rephaeli, S. Fan, Passive radiative cooling below ambient air temperature under direct sunlight. *Nature* **515**, 540–4 (2014).

20. A. Krishna, J. Lee, Morphology-Driven Emissivity of Microscale Tree-like Structures for Radiative Thermal Management. *Nanoscale Microscale Thermophys. Eng.* **22**, 124–136 (2018).

21. J. J. Klir, J. E. Heath, Thermoregulatory responses to thermal stimulation of the preoptic anterior hypothalamus in the red fox (Vulpes vulpes). *Comp. Biochem. Physiol. -- Part A Physiol.* **109**, 557–566 (1994).

22. N. N. Shi, *et al.*, Keeping cool: Enhanced optical reflection and radiative heat dissipation in Saharan silver ants. *Science (80-.).* **349**, 298–301 (2015).

23. J. S. Wilson, J. S. Sidwell, M. L. Forister, K. A. Williams, J. P. Pitts, Thistledown velvet ants in the Desert Mimicry Ring and the evolution of white coloration: Müllerian mimicry, camouflage and thermal ecology. *Biol. Lett.* **16**, 20200242 (2020).

24. D. J. McCafferty, G. Pandraud, J. Gilles, M. Fabra-Puchol, P. Y. Henry, Animal thermoregulation: A review of insulation, physiology and behaviour relevant to temperature control in buildings. *Bioinspiration and Biomimetics* **13** (2018).

25. C. Xu, G. T. Stiubianu, A. A. Gorodetsky, Adaptive infrared-reflecting systems inspired by cephalopods. *Science (80-.).* **359**, 1495–1500 (2018).

26. J. Xu, Z. Guo, Biomimetic photonic materials with tunable structural colors. *J. Colloid*

Interface Sci. **406**, 1–17 (2013).

27. Z. Han, *et al.*, Biomimetic multifunctional surfaces inspired from animals. *Adv. Colloid Interface Sci.* **234**, 27–50 (2016).

28. R. A. Potyrailo, *et al.*, Towards outperforming conventional sensor arrays with fabricated individual photonic vapour sensors inspired by Morpho butterflies. *Nat. Commun.* **6**, 7959 (2015).

29. A. D. Pris, *et al.*, Towards high-speed imaging of infrared photons with bio-inspired nanoarchitectures. *Nat. Photonics* **6**, 564–564 (2012).

30. M. R. J. Scherer, *et al.*, Mimicking the colourful wing scale structure of the Papilio blumei butterfly. *Nat. Nanotechnol.* **5**, 511–515 (2010).

31. C. C. Tsai, *et al.*, Butterflies regulate wing temperatures using radiative cooling in *Light in Nature VI*, (2017), p. 9.

32. , IUCN Red List of Threatened Species. *Choice Rev. Online* **49**, 49-6872-49–6872 (2012).

33. H. J. Stains, J. A. Chapman, G. A. Feldhamer, Wild Mammals of North America: Biology, Management, and Economics. *J. Wildl. Manage.* **47**, 571 (1983).

34. K. L. Laidre, G. S. York, *Polar bears: proceedings of the 18th working meeting of the IUCN/SSC Polar Bear Specialist Group, Anchorage, Alaska, 7-11 June 2016* (2018) https:/doi.org/10.2305/iucn.ch.2018.ssc-op.63.en.

35. D. E. McCoy, T. Feo, T. A. Harvey, R. O. Prum, Structural absorption by barbule

microstructures of super black bird of paradise feathers. *Nat. Commun.* **9** (2018).

36. B. Heinrich, Thermoregulation in endothermic insects. *Science (80-.).* **185**, 747–756 (1974).

37. J. E. Rawlins, Thermoregulation by the black swallowtail butterfly, Papilio polyxenes (Lepidoptera: Papilionidae). *Ecology* **61**, 345–357 (1980).

38. H. K. Clench, Behavioral Thermoregulation in Butterflies. *Ecology* **47**, 1021–1034 (1966).

39. T. C. Bonebrake, C. L. Boggs, J. A. Stamberger, C. A. Deutsch, P. R. Ehrlich, From global change to a butterfly flapping: Biophysics and behaviour affect tropical climate change impacts. *Proc. R. Soc. B Biol. Sci.* **281** (2014).

40. G. Nève, C. Hall, Variation of thorax flight temperature among twenty Australian butterflies (Lepidoptera: Papilionidae, Nymphalidae, Pieridae, Hesperiidae, Lycaenidae). *Eur. J. Entomol.* **113**, 571–578 (2016).

41. H. J. MacLean, J. K. Higgins, L. B. Buckley, J. G. Kingsolver, Morphological and physiological determinants of local adaptation to climate in Rocky Mountain butterflies. *Conserv. Physiol.* **4**, cow035 (2016).

42. Y. Zhai, *et al.*, Scalable-manufactured randomized glass-polymer hybrid metamaterial for daytime radiative cooling. *Science (80-.).* **355**, 1062–1066 (2017).

43. X. A. Zhang, *et al.*, Dynamic gating of infrared radiation in a textile. *Science (80-.).* **623**, 1–15 (2019).

44. D. Xie, *et al.*, Broadband omnidirectional light reflection and radiative heat dissipation in white beetles: Goliathus goliatus. *Soft Matter* **15**, 4294–4300 (2019).

45. K. Chung, *et al.*, Flexible, angle-independent, structural color reflectors inspired by morpho butterfly wings. *Adv. Mater.* **24**, 2375–2379 (2012).

46. L. Zhu, A. Raman, K. X. Wang, M. A. Anoma, S. Fan, Radiative cooling of solar cells. *Optica* **1**, 32–38 (2014).

47. L. Zhu, A. P. Raman, S. Fan, Radiative cooling of solar absorbers using a visibly transparent photonic crystal thermal blackbody. *Proc. Natl. Acad. Sci. U. S. A.* **112**, 12282–12287 (2015).

48. C. C. Tsai, *et al.*, Physical and behavioral adaptations to prevent overheating of the living wings of butterflies. *Nat. Commun.* **11** (2020).

49. B. D. Wilts, A. J. M. Vey, A. D. Briscoe, D. G. Stavenga, Longwing (Heliconius) butterflies combine a restricted set of pigmentary and structural coloration mechanisms. *BMC Evol. Biol.* **17** (2017).

50. K. Watanabe, T. Hoshino, K. Kanda, Y. Haruyama, S. Matsui, Brilliant Blue Observation from a Morpho -Butterfly-Scale Quasi-Structure. *Jpn. J. Appl. Phys.* **44**, L48–L50 (2005).

51. B. D. Wilts, M. A. Giraldo, D. G. Stavenga, Unique wing scale photonics of male Rajah Brooke's birdwing butterflies. *Front. Zool.* **13** (2016).

52. R. H. Siddique, S. Diewald, J. Leuthold, H. Hölscher, Theoretical and experimental analysis of the structural pattern responsible for the iridescence of Morpho

butterflies. *Opt. Express* **21**, 14351–14361 (2013).

53. J. Sun, B. Bhushan, J. Tong, Structural coloration in nature. *RSC Adv.* **3**, 14862–14889 (2013).

54. R. De Keyser, C. J. Breuker, R. S. Hails, R. L. H. Dennis, T. G. Shreeve, Why small is beautiful: Wing colour is free from thermoregulatory constraint in the small lycaenid butterfly, Polyommatus icarus. *PLoS One* **10** (2015).

55. L. P. Biró, *et al.*, Role of photonic-crystal-type structures in the thermal regulation of a Lycaenid butterfly sister species pair. *Phys. Rev. E - Stat. Physics, Plasmas, Fluids, Relat. Interdiscip. Top.* **67**, 7 (2003).

56. , Weather Underground Historical Weather. *https://www.wunderground.com/history/* (August 2, 2018).

57. , Weather Spark Weather Data. *https://weatherspark.com* (July 10, 2019).

58. B. D. Wilts, A. Matsushita, K. Arikawa, D. G. Stavenga, Spectrally tuned structural and pigmentary coloration of birdwing butterfly wing scales. *J. R. Soc. Interface* **12** (2015).

59. B. R. Wasik, *et al.*, Artificial selection for structural color on butterfly wings and comparison with natural evolution. *Proc. Natl. Acad. Sci.* **111**, 12109–12114 (2014).

60. X. Liu, S. Zhang, H. Zhang, Microstructure of butterfly wing scale and simulation of structural color. *Optik (Stuttg).* **127**, 1729–1733 (2016).

61. H. Tabata, K. Kumazawa, M. Funakawa, J. I. Takimoto, M. Akimoto, Microstructures

and optical properties of scales of butterfly wings. *Opt. Rev.* **3**, 139–145 (1996).

62. L. Wu, Z. Han, Z. Qiu, H. Guan, L. Ren, The microstructures of butterfly wing scales in northeast of China. *J. Bionic Eng.* **4**, 47–52 (2007).

63. F. Pratesi, M. Burresi, F. Riboli, K. Vynck, D. S. Wiersma, Disordered photonic structures for light harvesting in solar cells. *Opt. Express* **21**, A460 (2013).

64. D. S. Wiersma, P. Bartolini, A. Lagendijk, R. Righini, Localization of light in a disordered medium. *Nature* **390**, 671–673 (1997).

65. M.G.Moharam, T.K.Gaylord, Rigorous coupled-wave analysis of planar-grating diffraction. *J. Opt. Soc. Am.* **71**, 811 (1981).

66. S. Peng, G. M. Morris, Efficient implementation of rigorous coupled-wave analysis for surface-relief gratings. *J. Opt. Soc. Am. A* **12**, 1087 (1995).

67. D. E. Azofeifa, H. J. Arguedas, W. E. Vargas, Optical properties of chitin and chitosan biopolymers with application to structural color analysis. *Opt. Mater. (Amst).* **35**, 175–183 (2012).

68. W. E. Vargas, D. E. Azofeifa, H. J. Arguedas, Índices De Refracción De La Quitina, El Quitosano Y El Ácido Úrico Con Aplicación En Análisis De Color Estructural. *Opt. Pura y Apl.* **46**, 55–72 (2013).

69. A. Krishna, *et al.*, Infrared optical and thermal properties of microstructures in butterfly wings. *Proc. Natl. Acad. Sci. U. S. A.* **117**, 1566–1572 (2020).

70. H. O. McMahon, Thermal Radiation from Partially Transparent Reflecting Bodies. *J.*

Opt. Soc. Am. **40**, 376 (1950).

71. S. Catalanotti, *et al.*, The radiative cooling of selective surfaces. *Sol. Energy* **17**, 83–89 (1975).

72. J. long Kou, Z. Jurado, Z. Chen, S. Fan, A. J. Minnich, Daytime Radiative Cooling Using Near-Black Infrared Emitters. *ACS Photonics* **4**, 626–630 (2017).

73. J. Fang, *et al.*, Enhanced photocatalytic hydrogen production on three-dimensional gold butterfly wing scales/CdS nanoparticles. *Appl. Surf. Sci.* **427**, 807–812 (2018).

74. B. D. Wilts, H. L. Leertouwer, D. G. Stavenga, Imaging scatterometry and microspectrophotometry of lycaenid butterfly wing scales with perforated multilayers. *J. R. Soc. Interface* **6** (2009).

75. S. N. Aideo, D. Mohanta, Investigation of manifestation of optical properties of butterfly wings with nanoscale zinc oxide incorporation in *Journal of Physics: Conference Series*, (2016).

76. Y. Guan, *et al.*, Ordering of Hollow Ag-Au Nanospheres with Butterfly Wings as a Biolate. *Sci. Rep.* **8** (2018).

77. T. J. Simonsen, *et al.*, Phylogenetics and divergence times of Papilioninae (Lepidoptera) with special reference to the enigmatic genera Teinopalpus and Meandrusa. *Cladistics* **27**, 113–137 (2011).

78. B. D. Wilts, P. Pirih, K. Arikawa, D. G. Stavenga, Shiny wing scales cause spec(tac)ular camouflage of the angled sunbeam butterfly, Curetis acuta. *Biol. J. Linn. Soc.* **109**, 279–289 (2013).

79. M. New, D. Lister, M. Hulme, I. Makin, A high-resolution data set of surface climate over global land areas. *Clim. Res.* **21**, 1–25 (2002).

80. M. C. Peel, B. L. Finlayson, T. A. McMahon, Updated world map of the Köppen-Geiger climate classification. *Hydrol. Earth Syst. Sci.* **11**, 1633–1644 (2007).

81. F. Liu, *et al.*, Replication of homologous optical and hydrophobic features by templating wings of butterflies Morpho menelaus. *Opt. Commun.* **284**, 2376–2381 (2011).

82. T. Chen, Q. Cong, Y. Qi, J. Jin, K. L. Choy, Hydrophobic durability characteristics of butterfly wing surface after freezing cycles towards the design of nature inspired anti-icing surfaces. *PLoS One* **13**, e0188775 (2018).

83. Y. Fang, G. Sun, T. Q. Wang, Q. Cong, L. Q. Ren, Hydrophobicity mechanism of non-smooth pattern on surface of butterfly wing. *Chinese Sci. Bull.* **52**, 711–716 (2007).

84. Solargis, World Bank Organization, Energy Sector Management Assistance Program (ESMAP), Global Solar Atlas. *Glob. Sol. Atlas*, 1 (2019).

85. C. D. Ferris, F. M. Brown, *Butterflies of the Rocky Mountain states* (University of Oklahoma Press, 1981).

86. J. Llorente-Bousquets, H. Descimon, K. Johnson, Taxonomy and biogeography of Archaeoprepona demophoon in Mexico, with description of a new subspecies (Lepidoptera: Nymphalidae: Charaxinae). *Trop. Lepid.* **4**, 31–36 (1993).

87. , Información Climatológica por Estado, Coordinación General del Servicio Meteorológico Nacional. *https://smn.conagua.gob.mx/es/informacion-climatologica-*

por-estado?estado=oax (November 14, 2019).

88. , Supplemental Monthly Temperature Normals for Cheesman, Colorado, National Centers for Environmental Information, National Oceanic and Atmospheric Administration. *https://www.ncdc.noaa.gov/normalsPDFaccess/* (November 14, 2019).

89. J. S. Tsuji, J. G. Kingsolver, W. B. Watt, Thermal physiological ecology of Colias butterflies in flight. *Oecologia* **69**, 161–170 (1986).

90. H. Van Dyck, E. Matthysen, Thermoregulatory differences between phenotypes in the speckled wood butterfly: Hot perchers and cold patrollers? *Oecologia* **114**, 326–334 (1998).

91. L. P. Brower, E. H. Williams, L. S. Fink, R. R. Zubieta, Ram, Monarch Butterfly Clusters Provide Microclimate Advantages During the Overwintering Season in Mexico. *J. Lepid. Soc.* **62**, 177–188 (2008).

92. The National Renewable Energy Laboratory (NREL), Reference Solar Spectral Irradiance: Air Mass 1.5. *Am. Soc. Test. Mater. - Terr. Ref. Spectra Photovolt. Perform. Eval.*, 21 (2012).

93. F. Al-Amri, T. K. Mallick, Alleviating operating temperature of concentration solar cell by air active cooling and surface radiation. *Appl. Therm. Eng.* **59**, 348–354 (2013).

94. H. Najafi, K. A. Woodbury, Optimization of a cooling system based on Peltier effect for photovoltaic cells. *Sol. Energy* **91**, 152–160 (2013).

95. K. A. Moharram, M. S. Abd-Elhady, H. A. Kandil, H. El-Sherif, Enhancing the

performance of photovoltaic panels by water cooling. *Ain Shams Eng. J.* **4**, 869–877 (2013).

96. S. Huang, *et al.*, Infrared Emissivity Measurement for Vertically Aligned Multiwall Carbon Nanotubes (CNTs) Based Heat Spreader Applied in High Power Electronics Packaging in *2016 6th Electronic System-Integration Technology Conference (ESTC)*, (2016).

97. S. Huang, *et al.*, The effects of graphene-based films as heat spreaders for thermal management in electronic packaging. *2016 17th Int. Conf. Electron. Packag. Technol.*, 889–892 (2016).

98. H. C. Cheng, T. C. Huang, P. W. Hwang, W. H. Chen, Heat dissipation assessment of through silicon via (TSV)-based 3D IC packaging for CMOS image sensing. *Microelectron. Reliab.* **59**, 84–94 (2015).

99. C. Li, M. Zou, Y. Shang, M. Zhang, Study on the Thermal Transient Response of TSV Considering the Effect of Electronic-Thermal Coupling. *J. Semicond. Technol. Sci.* **15**, 356–364 (2015).

100. P. C. Hsu, *et al.*, Personal thermal management by metallic nanowire-coated textile. *Nano Lett.* **15**, 365–371 (2015).

101. X. Liu, *et al.*, Taming the blackbody with infrared metamaterials as selective thermal emitters. *Phys. Rev. Lett.* **107** (2011).

102. K.-N. Liou, E. A. Rogério dos Santos Alves; Alex Soares de Souza, *An Introduction to Atmospheric Radiation* (1980).

103. E. Rephaeli, A. Raman, S. Fan, Ultrabroadband photonic structures to achieve high-performance daytime radiative cooling. *Nano Lett.* **13**, 1457–1461 (2013).

104. Z. Chen, L. Zhu, A. Raman, S. Fan, Radiative cooling to deep sub-freezing temperatures through a 24-h day-night cycle. *Nat. Commun.* **7**, 1–5 (2016).

105. Y. Huang, Q. Zhao, S. K. Kalyoncu, R. Torun, O. Boyraz, Silicon-on-sapphire mid-IR wavefront engineering by using subwavelength grating metasurfaces. *J. Opt. Soc. Am. B* **33**, 189 (2016).

106. J. Zi, *et al.*, Coloration strategies in peacock feathers. *Proc. Natl. Acad. Sci.* **100**, 12576–12578 (2003).

107. D. G. Stavenga, J. Tinbergen, H. L. Leertouwer, B. D. Wilts, Kingfisher feathers - colouration by pigments, spongy nanostructures and thin films. *J. Exp. Biol.* **214**, 3960–3967 (2011).

108. P. Vukusic, J. R. Sambles, Photonic structures in biology. *Nature* **424**, 852–855 (2003).

109. A. R. Parker, N. Martini, Structural colour in animals - Simple to complex optics in *Optics and Laser Technology*, (2006), pp. 315–322.

110. S. Kinoshita, *Structural colors in the realm of nature* (World Scientific, 2008).

111. R. O. Prum, Structural colouration of mammalian skin: convergent evolution of coherently scattering dermal collagen arrays. *J. Exp. Biol.* **207**, 2157–2172 (2004).

112. H. Butt, *et al.*, *Morpho* Butterfly-Inspired Nanostructures. *Adv. Opt. Mater.* **4**, 497–504

(2016).

113. F. Zhang, *et al.*, Infrared detection based on localized modification of Morpho butterfly wings. *Adv. Mater.* **27**, 1077–1082 (2015).

114. L. del Campo, *et al.*, Emissivity measurements on aeronautical alloys. *J. Alloys Compd.* **489**, 482–487 (2010).

115. T. Furukawa, T. Iuchi, Experimental apparatus for radiometric emissivity measurements of metals. *Rev. Sci. Instrum.* **71**, 2843 (2000).

116. P. Herve, J. Cedelle, I. Negreanu, Infrared technique for simultaneous determination of temperature and emissivity. *Infrared Phys. Technol.* **55**, 1–10 (2012).

117. H. Sai, Y. Kanamori, Spectrally Selective Thermal Radiators and Absorbers With Periodic Microstructured Surface for High-Temperature Applications. *Microscale Thermophys. Eng.* **7**, 101–115 (2003).

118. K. S. Chen, *et al.*, Emission of rough surfaces calculated by the integral equation method with comparison to three-dimensional moment method simulations. *IEEE Trans. Geosci. Remote Sens.* **41**, 90–101 (2003).

119. M. G. Moharam, Coupled-Wave Analysis Of Two-Dimensional Dielectric Gratings in *Holographic Optics: Design and Applications*, (1988), p. 8.

120. M. G. Moharam, T. K. Gaylord, E. B. Grann, D. A. Pommet, Formulation for stable and efficient implementation of the rigorous coupled-wave analysis of binary gratings. *J. Opt. Soc. Am. A* **12**, 1068 (1995).

121. J. Heo, *et al.*, (Sn,Al)Ox Films Grown by Atomic Layer Deposition. *J. Phys. Chem. C* **115**, 10277–10283 (2011).

122. R. L. Puurunen, A short history of atomic layer deposition: Tuomo Suntola's atomic layer epitaxy. *Chem. Vap. Depos.* **20**, 332–344 (2014).

123. M. a Steindorfer, V. Schmidt, M. Belegratis, B. Stadlober, J. R. Krenn, Detailed simulation of structural color generation inspired by the Morpho butterfly. *Opt. Express* **20**, 21485–94 (2012).

124. J. Huang, X. Wang, Z. L. Wang, Controlled replication of butterfly wings for achieving tunable photonic properties. *Nano Lett.* **6**, 2325–2331 (2006).

125. M. A. Hanning-Lee, B. B. Brady, L. R. Martin, J. A. Syage, Ozone decomposition on alumina: Implications for solid rocket. *Geophys. Res. Lett.* **23**, 1961–1964 (1996).

126. I. H. Malitson, Interspecimen Comparison of the Refractive Index of Fused Silica. *J. Opt. Soc. Am.* **55**, 1205 (1965).

127. D. Stephenson, "Modeling variation in the refractive index of optical glasses," Rochester Institute of Technology. (1990).

128. P. Vitanov, A. Harizanova, T. Ivanova, Z. Alexieva, G. Agostinelli, Deposition and Properties of the Pseudobinary Alloy (Al 2 O 3) x (TiO 2) 1- x and Its Application for Silicon Surface Passivation. *Jpn. J. Appl. Phys.* **45**, 5894–5901 (2006).

129. D. Choi, S.-J. Kim, J. H. Lee, K.-B. Chung, J.-S. Park, A study of thin film encapsulation on polymer substrate using low temperature hybrid ZnO/Al2O3 layers atomic layer deposition. *Curr. Appl. Phys.* **12**, S19–S23 (2012).

130. S. H. Kang, T. Y. Tai, T. H. Fang, Replication of butterfly wing microstructures using molding lithography. *Curr. Appl. Phys.* **10**, 625–630 (2010).

131. J. Kischkat, *et al.*, Mid-infrared optical properties of thin films of aluminum oxide, titanium dioxide, silicon dioxide, aluminum nitride, and silicon nitride. *Appl. Opt.* **51**, 6789–6798 (2012).

132. M. A. Ordal, R. J. Bell, R. W. Alexander, L. L. Long, M. R. Querry, Optical properties of fourteen metals in the infrared and far infrared: Al, Co, Cu, Au, Fe, Pb, Mo, Ni, Pd, Pt, Ag, Ti, V, and W. *Appl. Opt.* **24**, 4493 (1985).

133. O. Coddington, J. L. Lean, P. Pilewskie, M. Snow, D. Lindholm, A solar irradiance climate data record. *Bull. Am. Meteorol. Soc.* **97**, 1265–1282 (2016).

134. D. A. Murdock, J. E. Ramos Torres, J. J. Connors, R. D. Lorenz, Active thermal control of power electronic modules. *IEEE Trans. Ind. Appl.* **42**, 552–558 (2006).

135. T. D. Swanson, G. C. Birur, NASA thermal control technologies for robotic spacecraft in *Applied Thermal Engineering*, (2003), pp. 1055–1065.

136. C. A. Gueymard, D. Myers, K. Emery, Proposed reference irradiance spectra for solar energy systems testing. *Sol. Energy* **73**, 443–467 (2002).

137. Z. Huang, X. Ruan, Nanoparticle embedded double-layer coating for daytime radiative cooling. *Int. J. Heat Mass Transf.* **104**, 890–896 (2017).

138. A. Lenert, *et al.*, A nanophotonic solar thermophotovoltaic device. *Nat. Nanotechnol.* **9**, 126–130 (2014).

139. L. Hu, G. Chen, Analysis of optical absorption in silicon nanowire arrays for photovoltaic applications. *Nano Lett.* **7**, 3249–52 (2007).

140. J. Quintiere, Radiative characteristics of fire fighters' coat fabrics. *Fire Technol.* **10**, 153–161 (1974).

141. M. Ono, K. Chen, W. Li, S. Fan, Self-adaptive radiative cooling based on phase change materials. *Opt. Express* **26**, A777–A787 (2018).

142. H. Wang, Y. Yang, L. Wang, Switchable wavelength-selective and diffuse metamaterial absorber/emitter with a phase transition spacer layer. *Appl. Phys. Lett.* **105** (2014).

143. S. Taylor, Y. Yang, L. Wang, Vanadium dioxide based Fabry-Perot emitter for dynamic radiative cooling applications. *J. Quant. Spectrosc. Radiat. Transf.* **197**, 76–83 (2017).

144. A. Kazemi Moridani, *et al.*, Plasmonic Thermal Emitters for Dynamically Tunable Infrared Radiation. *Adv. Opt. Mater.* **5** (2017).

145. M. C. Wang, *et al.*, Heterogeneous, three-dimensional texturing of graphene. *Nano Lett.* **15**, 1829–1835 (2015).

146. V. W. Brar, *et al.*, Electronic modulation of infrared radiation in graphene plasmonic resonators. *Nat. Commun.* **6** (2015).

147. O. Salihoglu, *et al.*, Graphene-Based Adaptive Thermal Camouflage. *Nano Lett.* **18**, 4541–4548 (2018).

148. J. V. Anguita, M. Ahmad, S. Haq, J. Allam, S. R. P. Silva, Nanotechnology: Ultra-broadband light trapping using nanotextured decoupled graphene multilayers. *Sci.*

Adv. **2** (2016).

149. C. Lee, X. Wei, J. W. Kysar, J. Hone, Measurement of the elastic properties and intrinsic strength of monolayer graphene. *Science (80-.).* **321**, 385–388 (2008).

150. S. V. Muley, N. M. Ravindra, Emissivity of electronic materials, coatings, and structures. *Jom* **66**, 616–636 (2014).

151. R. Magnusson, T. K. Gaylord, Analysis of multiwave diffraction of thick gratings. *J. Opt. Soc. Am.* **67**, 1165 (1977).

152. J. W. Weber, V. E. Calado, M. C. M. Van De Sanden, Optical constants of graphene measured by spectroscopic ellipsometry. *Appl. Phys. Lett.* **97** (2010).

153. E. Ochoa-Martínez, *et al.*, Determination of a refractive index and an extinction coefficient of standard production of CVD-graphene. *Nanoscale* **7**, 1491–1500 (2015).

154. A. Krishna, *et al.*, Ultraviolet to Mid-Infrared Emissivity Control by Mechanically Reconfigurable Graphene. *Nano Lett.* **19**, 5086–5092 (2019).

155. E. S. R. L. US Department of Commerce, NOAA, ESRL Global Monitoring Division - Global Radiation Group (2015) (October 6, 2018).

156. P. Kang, M. C. Wang, P. M. Knapp, S. W. Nam, Crumpled Graphene Photodetector with Enhanced, Strain-Tunable, and Wavelength-Selective Photoresponsivity. *Adv. Mater.* **28**, 4639–4645 (2016).

157. D. Rhee, W. K. Lee, T. W. Odom, Crack-Free, Soft Wrinkles Enable Switchable Anisotropic Wetting. *Angew. Chemie - Int. Ed.* **56**, 6523–6527 (2017).

158. L. Cai, *et al.*, Warming up human body by nanoporous metallized polyethylene textile. *Nat. Commun.* **8** (2017).

159. Y. Zhai, *et al.*, Scalable-manufactured randomized glass-polymer hybrid metamaterial for daytime radiative cooling. *Science* **355**, 1062–1066 (2017).

160. Y. M. Song, J. S. Yu, Y. T. Lee, Antireflective submicrometer gratings on thin-film silicon solar cells for light-absorption enhancement. *Opt. Lett.* **35**, 276–278 (2010).

161. W. Ma, Y. Wen, X. Yu, Broadband metamaterial absorber at mid-infrared using multiplexed cross resonators. *Opt. Express* **21**, 30724 (2013).

162. T. Maier, H. Brückl, Wavelength-tunable microbolometers with metamaterial absorbers. *Opt. Lett.* **34**, 3012 (2009).

163. R. Osiander, S. L. Firebaugh, J. L. Champion, D. Farrar, M. A. G. Darrin, Microelectromechanical devices for satellite thermal control. *IEEE Sens. J.* **4**, 525–531 (2004).

164. P.-C. Hsu, *et al.*, A dual-mode textile for human body radiative heating and cooling. *Sci. Adv.* **3**, e1700895 (2017).

165. D. H. Kim, J. A. Rogers, Stretchable electronics: Materials strategies and devices. *Adv. Mater.* **20**, 4887–4892 (2008).

166. A. M. Hussain, *et al.*, Metal/Polymer Based Stretchable Antenna for Constant Frequency Far-Field Communication in Wearable Electronics. *Adv. Funct. Mater.* **25**, 6565–6575 (2015).

167. C. Yan, *et al.*, Stretchable and wearable electrochromic devices. *ACS Nano* **8**, 316–322 (2014).

168. Y. Peng, *et al.*, Nanoporous polyethylene microfibres for large-scale radiative cooling fabric. *Nat. Sustain.* **1**, 105–112 (2018).

169. P. B. Catrysse, A. Y. Song, S. Fan, Photonic Structure Textile Design for Localized Thermal Cooling Based on a Fiber Blending Scheme. *ACS Photonics* **3**, 2420–2426 (2016).

170. J. K. Tong, *et al.*, Infrared-Transparent Visible-Opaque Fabrics for Wearable Personal Thermal Management. *ACS Photonics* **2**, 769–778 (2015).

171. L. Cai, *et al.*, Spectrally Selective Nanocomposite Textile for Outdoor Personal Cooling. *Adv. Mater.* **30**, 1802152 (2018).

172. K.-K. Du, *et al.*, Control over emissivity of zero-static-power thermal emitters based on phase-changing material GST. *Light Sci. Appl.* **6**, e16194 (2017).

173. N. N. Shi, *et al.*, Keeping cool: Enhanced optical reflection and radiative heat dissipation in Saharan silver ants. *Science (80-.).* **349**, 298–301 (2015).

174. J. Teyssier, S. V. Saenko, D. Van Der Marel, M. C. Milinkovitch, Photonic crystals cause active colour change in chameleons. *Nat. Commun.* **6**, 1–7 (2015).

175. A. Narayanaswamy, G. Chen, Thermal emission control with one-dimensional metallodielectric photonic crystals. *Phys. Rev. B* **70**, 125101 (2004).

176. R. A. Lowe, D. L. Chubb, S. C. Farmer, B. S. Good, Rare-earth garnet selective emitter.

Appl. Phys. Lett. **64**, 3551–3553 (1994).

177. W. Sabuga, R. Todtenhaupt, Effect of roughness on the emissivity of the precious metals silver, gold, palladium, platinum, rhodium, and iridium. *High Temp. - High Press.* **33**, 261–269 (2001).

178. A. G. Worthing, Physical properties of well seasoned molybdenum and tantalum as a function of temperature. *Phys. Rev.* **28**, 190–201 (1926).

179. B. Jae Lee, Y.-B. Chen, S. Han, F.-C. Chiu, H. Jin Lee, Wavelength-Selective Solar Thermal Absorber With Two-Dimensional Nickel Gratings. *J. Heat Transfer* **136**, 072702 (2014).

180. S. Zeng, *et al.*, Bio-inspired sensitive and reversible mechanochromisms via strain-dependent cracks and folds. *Nat. Commun.* **7**, 11802 (2016).

181. S. G. Lee, *et al.*, Switchable Transparency and Wetting of Elastomeric Smart Windows. *Adv. Mater.* **22**, 5013–5017 (2010).

182. E. Lee, *et al.*, Tilted Pillars on Wrinkled Elastomers as a Reversibly Tunable Optical Window. *Adv. Mater.* **26**, 4127–4133 (2014).

183. M. Sala-Casanovas, A. Krishna, Z. Yu, J. Lee, Bio-Inspired Stretchable Selective Emitters Based on Corrugated Nickel for Personal Thermal Management. *Nanoscale Microscale Thermophys. Eng.*, 1–15 (2019).

184. A. Taflove, S. C. Hagness, *Computational electrodynamics : the finite-difference time-domain method* (Artech House, 2005).

185. M. A. Ordal, R. J. Bell, R. W. Alexander, L. L. Long, M. R. Querry, Optical properties of Au, Ni, and Pb at submillimeter wavelengths. *Appl. Opt.* **26**, 744 (1987).

186. E. D. Palik, *Handbook of optical constants of solids* (2012).

187. S. Shian, D. R. Clarke, Electrically tunable window device. *Opt. Lett.* **41**, 1289 (2016).

188. M. Shrestha, G.-K. Lau, Tunable window device based on micro-wrinkling of nanometric zinc-oxide thin film on elastomer. *Opt. Lett.* **41**, 4433 (2016).

189. 3M, VHB ™ Tapes Technical Data. **25**, 1–9 (2014).

190. E. M. Sparrow, S. H. Lin, Absorption of thermal radiation in a V-groove cavity. *Int. J. Heat Mass Transf.* **5**, 1111–1115 (1962).

191. J.-H. Choi, V. Loftness, Investigation of human body skin temperatures as a bio-signal to indicate overall thermal sensations. *Build. Environ.* **58**, 258–269 (2012).

192. N. Romeijn, E. J. W. Van Someren, Correlated Fluctuations of Daytime Skin Temperature and Vigilance. *J. Biol. Rhythms* **26**, 68–77 (2011).

193. B. Saggin, M. Tarabini, G. Lanfranchi, A device for the skin-contact thermal resistance measurement. *IEEE Trans. Instrum. Meas.* **61**, 489–495 (2012).

194. T. V McCaffrey, R. D. Wurster, H. K. Jacobs, D. E. Euler, G. S. Geis, Role of skin temperature in the control of sweating. *J. Appl. Physiol.* **47**, 591–597 (1979).

195. D. Gagnon, O. Jay, G. P. Kenny, The evaporative requirement for heat balance determines whole-body sweat rate during exercise under conditions permitting full evaporation. *J. Physiol.* **591**, 2925–2935 (2013).

196. G.-B. Lee, S. G. Sathi, D.-Y. Kim, K.-U. Jeong, C. Nah, Wrinkled elastomers for the highly stretchable electrodes with excellent fatigue resistances. *Polym. Test.* **53**, 329–337 (2016).

197. W. Fan, Y. Wang, S. Cai, Fatigue fracture of a highly stretchable acrylic elastomer. *Polym. Test.* **61**, 373–377 (2017).